



國立臺灣大學工學院材料科學與工程學研究所

博士論文

Department of Materials Science and Engineering

College of Engineering

National Taiwan University

Doctoral Dissertation

原子層沉積之金屬氧化物及高分子/金屬氧化物超晶格

複合材料熱電性質及氣體滲透率研究

Thermoelectricity and gas permeability of metal oxide and
metal oxide/polymer superlattice composites by atomic

layer deposition

施柏瑋

Bo-Wei Shih

指導教授：蔡豐羽 博士

Advisor: Feng-Yu Tsai, Ph.D.

中華民國 108 年 12 月

December, 2019



國立臺灣大學博士學位論文
口試委員會審定書

論文中文題目： 原子層沉積之金屬氧化物及高分子/金屬氧化物超晶格複合材料熱電性質及氣體滲透率研究

論文英文題目： Thermoelectricity and gas permeability of metal oxide and metal oxide/polymer superlattice composites by atomic layer deposition

本論文係施柏瑋君 (D02527016) 在國立臺灣大學材料科學與工程學系、所完成之博士學位論文，於民國 108 年 12 月 18 日承下列考試委員審查通過及口試及格，特此證明

口試委員： 蔡豐羽
(指導教授)

郭錦龍

白奇峰

謝文斌

陳奕君

系主任、所長 謝宗霖 (簽名)



誌謝

經過漫長的求學生涯，終於要卸下學生的角色了。在這最後一段的博士班歲月中，可說是充滿磨練與挫折，但因有了許多人的鼓勵與幫助，讓我可以克服難關，順利的走完這讓我成長最多的一個階段。

首先要感謝的是我的指導教授蔡豐羽博士所給予訓練。在研究過程中，教授的信任讓我可以自由地發揮想像以及嘗試各種實驗；但在重要的時刻，您的及時督導及糾正讓我可以發現自己的錯誤並修正。因此，在博士班的學習中，讓我培養出可以獨立思考並謹慎自我審視的能力。於此同時，也要感謝謝文斌教授長期提供實驗資源讓我能順利完成研究，以及郭錦龍教授於口試前及時雨的鼓勵讓我混亂的思緒得以沉澱。

感謝實驗室學長姐們的知識分享和經驗傳授，讓我於研究初期可以快速的步入軌道；也感謝各個學弟學妹們，你們的好學讓我在扮演學長這個角色時，可以重新審視我所學的知識及技能。謝謝各位在實驗室遇到的人，你們豐富了我的研究生活。接下來要感謝的是，系辦各位阿姨、牙醫系琬瑜學姐和勝豪學長，以及大學和高中的好友們，你們讓我在研究之餘或是研究疲憊時，可以向你們吐苦水或是聽你們的幹話吐槽和各種八卦來調劑身心，謝謝各為讓我的台北生活更加精采。


最後要感謝的是，一直以來支持我的媽媽、大姐一家、二姐一家、三姐以及子華，你們不管是無形或是實值的照顧和關愛，是讓我有能力面對各項挑戰以及獲得博士學位最重要的動力來源，謝謝你們無條件的陪伴，你們是我最重要的寶藏。

摘要



本研究將探討由原子層沉積技術所製備之超晶格薄膜材料於熱電領域以及各種不同領域之應用，如：可撓式超高阻氣性薄膜以及奈米孔洞材料之開發。隨著穿戴型電子裝置的普及以及積體電路尺度的微縮，如何回收裝置操作時所產生的廢熱和冷卻裝置中各種微型晶片以達到再生能源之利用和裝置元件壽命的延長為現今科學家及工業界爭相研究之項目。其中薄膜熱電技術為一可同時解決這些問題之技術，但其實用性仍受限於高效能薄膜熱電材料以及高可靠性熱電薄膜製程技術之缺乏。在材料選擇方面，相較於傳統的重金屬化合物塊材熱電材料，金屬氧化物半導體薄膜熱電材料具備多項優勢，包括價格低廉、化學性質穩定、環境友善、且薄膜製備簡易等，因此為極受看好之新世代熱電材料。然而，金屬氧化物雖具有良好的電導率及 Seebeck coefficient，但其熱導率亦極高，使其代表熱電效能之 ZT 值難以提高。本研究將利用具高可靠性之薄膜沉積技術—原子層沉積技術(ALD)製備技術純熟之氧化鋅薄膜並藉由進行新穎觀念之研究，以大幅提升之氧化鋅薄膜之熱電效能，此外，亦進行將超晶格薄膜應用於可撓式超高阻氣性薄膜以及奈米孔洞材料之開發的研究。本論文主要的研究項目有下列五點：

- (1) 在 ALD 氧化鋅中，引入不同之摻雜物以形成週期性超晶格結構，並探討摻雜物種類、濃度、分布方式以及超晶格週期對於熱電效應之影響。在我們的研究中顯示，高原子量以及離子半徑匹配於基質之摻雜物在同時使用傳統摻雜技術和本實驗室所開發的混合層摻雜技術下，可對基質之熱電效能有最佳之提升，其幅度可達 12 倍。
- (2) 在 ALD 反應中，使用具 ^{18}O 與 ^{16}O 同位素之前驅物以形成具有同位素之超晶格薄膜，此研究就可在維持前項研究中所最佳化之電性條件下，更進一步的降低熱導率。於結果中顯示，50%的同位素混摻並在疊層週期約為 10 奈米時，可將前項研究中最佳之熱導率再下降 20~25%。

- 
- (3) 開發新穎分子層沉積(MLD)之有機高分子導電薄膜，與金屬氧化物層交替沉積形成高分子/氧化物超晶格薄膜，藉由大量的有機/無機界面來大幅降低材料熱導率，但仍維持高導電度。於導電高分子的研究上，我們成功開發出兩款高分子薄膜，其中一款電導率可高達 500 S cm^{-1} 。而在高分子/氧化物超晶格薄膜的熱電性質表現上，在最佳化的結構中，其熱電效能可提升 7 倍。
- (4) 開發具抗水解能力之高分子即其所形成之高分子/氧化物超晶格薄膜阻氣性質研究。於結果中，該高分子即其所形成之超晶格薄膜皆於高濕度的環境下，具有較高的穩定性。
- (5) 開發低溫熱裂解技術，以製備奈米孔洞材料。於研究中發現，在水氣的幫助下，可大幅降低 alucone 之熱裂解溫度以形成奈米孔洞材料。其最佳化的條件中，可有效移除高達 70% 的碳含量，且退火溫度可低於 100°C 。因此，此技術將使奈米孔洞材料可沉積於高分子基板以及應用於各種軟性電子元件中。

關鍵詞：薄膜熱電材料、原子層沉積技術、分子層沉積技術、氧化鋅、超晶格薄膜、高分子奈米複合材料、可撓式高阻氣性薄膜、奈米孔洞材料。

Abstract



Thermoelectric thin films are an important type of materials for the management and recycling of waste heat in the ever-shrinking electronic devices, but their development has been hindered by the dearth of methods for fabricating high-quality thin films with adequate thermoelectric performance, i.e. high Seebeck coefficient, high electrical conductivity, and low thermal conductivity. This study develops high-quality superlattice thin films based on metal oxides and conducting polymers by atomic layer deposition (ALD) and molecular layer deposition (MLD), aiming to realize significant enhancement in the thermoelectric figure of merit, or ZT value, of the resultant thin films. Additionally, the gas permeation properties of the ALD/MLD superlattice thin films are also examined. Key results and findings of this work are summarized as follows.

- (1) Effects of composition and structure on the thermoelectric properties of metal oxide superlattice thin films: We used ZnO as our host material, into which we insert HfO₂, ZrO₂, or TiO₂ guest layers with various thicknesses and periodicities as both electrical dopants and phonon-scattering centers. We arrived at the following conclusions: (i) of the 3 types of guest layers, HfO₂ showed the best overall enhancement in ZT, by a factor of 12, over the ZnO host owing to Hf's similar ionic radius to Zn's and high atomic mass; (ii) the



optimal electrical performance was achieved by forming the guest layers as a mixture of both ZnO and the guest in a periodicity of 1 mixed monolayer per 24 ZnO monolayer; (iii) the best phonon-scattering effect was obtained by inserting 7 guest monolayers for every two periods of the structure described in (ii).

- (2) Effects of incorporating O¹⁸ isotope into the metal oxide superlattice on its thermoelectric properties: Based on the optimal structure we developed in (1), we found that the ZT could be further increased by around 20% by replacing 50% of the oxygen content with O¹⁸ in a periodicity of 10 nm O¹⁶/10 nm O¹⁸.
- (3) Development of novel MLD conducting polymers and their superlattices with metal oxide semiconductors: Two polymers, polyaniline and poly(3,4-ethylenedioxythiophene) (PEDOT), were successfully deposited with electrical conductivity of up to 500 S cm⁻¹. Superlattice films composed of alternating 4 periods of ALD mix 19:1 HZO and 6 cycles of MLD PEDOT were found to offer the maximum improvement in ZT, by ~700%, over that of the undoped ZnO.
- (4) Development of hydrolysis-resistant MLD polymer films to fabricate ALD/MLD nanolaminated high-performance gas barrier films: Polyamide (Poly(imino-carbonyl-1,4-phenylene-carbonyl-iminoethylene)) films deposited

from terephthaloyl chloride and ethylenediamine were found to provide the best long-term stability under humid condition among several polyamide films studied.



Key words: Thin-film thermoelectrics, atomic layer deposition (ALD), molecular layer deposition (MLD), zinc oxide (ZnO), superlattice, conducting polymer nanocomposites, flexible gas barrier, nanoporous materials.

Table of Contents



誌謝	i
摘要	ii
Abstract.....	iv
Table of Contents.....	vii
List of Figures.....	xii
List of Tables	xix
Chapter 1 Introduction.....	1
1.1 Overview of thermoelectricity	1
1.2 Fundamental of thermoelectric effect.....	4
1.2.1 Origin of thermoelectric effect	4
1.2.2 Trade-off between electrical conductivity and Seebeck coefficient.....	8
1.2.3 Thermal conductivity of materials.....	11
1.2.4 The figure of merit, ZT.....	14
1.3 Thermoelectricity in thin films	16

1.3.1	Size effect	16
1.3.2	Superlattice(Nanolaminates)	17
1.3.3	Advantages of thin film thermoelectric materials	19
1.4	Fundamental of atomic layer deposition and its advantages of depositing thin film thermoelectric materials	22
1.4.1	Atomic layer deposition(ALD).....	22
1.4.2	Molecular layer deposition(MLD)	24
1.4.3	Advantages of ALD on depositing thin film thermoelectric materials.....	26
1.5	Literature review of thin film thermoelectric materials deposited by ALD	29
1.6	Applications of ALD/MLD superlattices	32
1.6.1	Flexible high performance gas barrier.....	32
1.6.2	Nanoporous materials	34
1.7	Motivation and objective statements	36
1.8	Research approach.....	39
1.8.1	High valence and high atomic weight metal ion doping	39
1.8.2	Isotope superlattice	40
1.8.3	Novel MLD conducting polymer development and the metal oxide/polymer superlattice deposition	41

1.8.4	Anti-hydrolysis polymer development	43
1.9	Dissertation Organization	45
Chapter 2 Experimental methods		47
2.1	Equipment and experiment details	47
2.1.1	ALD and MLD deposition systems	47
2.1.2	Conventional and mixed ALD metal ion doping process.....	48
2.1.3	Oxygen isotope incorporated superlattice	51
2.1.4	MLD conducting polymer process	52
2.1.5	Anti-hydrolysis polymers and metalcone process	54
2.2	Thin film characteristics analysis	56
2.2.1	Measurements of electrical conductivity and Seebeck coefficient.....	56
2.2.2	Measurement of thermal conductivity by the time-domain thermoreflectance method (TDTR)	57
2.2.3	Quartz crystal microbalance (QCM)	61
2.2.4	Spectral characterization.....	61
2.2.5	Transmission electron microscopy (TEM)	62
2.2.6	Micro-figure measurement (Alpha-step).....	63
2.2.7	Gas barrier performance measurements	63

2.2.8	Thermogravimetric analysis (TGA)	64
Chapter 3 Metal oxide superlattice		65
3.1	Selection of dopants.....	65
3.2	Distribution Patterns of dopants	72
3.2.1	Conventional versus mixed ALD doping processes	72
3.2.2	Combination of conventional and mixed ALD doping processes	79
3.3	Isotope superlattice	92
3.3.1	Modification of deposition parameters.....	92
3.3.2	Influence on thermoelectric properties	94
3.4	Summary.....	100
Chapter 4 Metal oxide/polymer superlattice		102
4.1	Poly(3,4-ethylenedioxythiophene) (PEDOT).....	102
4.1.1	The deposition of PEDOT	102
4.1.2	Interface-engineering of metal oxide/PEDOT superlattice	108
4.1.3	Superlattice deposition and thermoelectric performance	114
4.2	Polyaniline	127
4.3	Polythiophene	130

4.4	Summary	132
Chapter 5 Long-term stable gas barrier		134
5.1	The deposition of polyamide	134
5.2	The gas barrier performance of polyamide and HfO ₂ /polyamide superlattice 143	
5.3	The deposition of polyester	146
5.4	Summary	149
Chapter 6 Conclusions		150
Reference		153
Appendix		
Nanoporous materials		161
Other data		169



List of Figures



Chapter 1

Figure 1.1: Operating principle of TE materials.....	3
Figure 1.2: Best ZT value for bulk n-type and p-type TE materials.	3
Figure 1.3: Illustration of model for deducing.	6
Figure 1.4: The Fermi Dirac distributions at each end and difference between them.....	6
Figure 1.5: The dependence of Seebeck coefficient on DOS over energy states.	7
Figure 1.6: Fermi window and Fermi-Dirac distribution.	10
Figure 1.7: Tendency of Seebeck coefficient and electrical with regard to the location of Fermi window.....	11
Figure 1.8: Contribution of κ_{el} and κ_{ph} to κ_{total} for different types of materials.	15
Figure 1.9: The optimization of ZT through carrier concentration tuning..	15
Figure 1.10: The schematic diagram of the density of states for electrons in different dimension based on parabolic band structure.....	21
Figure 1.11: The schematic diagram of energy filtering effect in superlattice.....	21
Figure 1.12: The schematic illustration of ALD film growth mechanism.....	27
Figure 1.13: ALD window, the dependence of growth rate per cycle on temperature... ..	28
Figure 1.14: The schematic illustration of MLD polyester film growth mechanism.	28



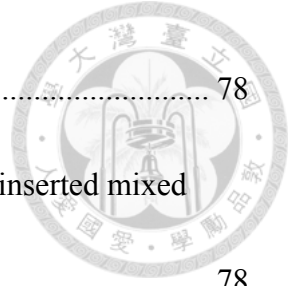
Figure 1.15: The structure of PA32.	33
Figure 1.16: The schematics of torturous path of inorganic-organic multilayer gas barrier.....	33
Figure 1.17: The schematic illustration of the evolution of ALD/MLD superlattice after post-annealing in various atmosphere.	35
Figure 1.18: The tunability of pore size resulted from ALD/MLD superlattice.....	35
Figure 1.19: The reaction mechanism of MLD PEDOT ⁹⁵	43

Chapter 2

Figure 2.1: The scheme illustration of home-made system for measuring Seebeck coefficient.	57
Figure 2.2: The multilayered structure used for simulation.	59
Figure 2.3: The result of ZnO thermal conductivity by TDTR method.	60
Figure 2.4: The schematic layout of TDTR apparatus.	60
Figure 2.5: The calculated $S\alpha$ for each parameters in simulation.	61

Chapter 3

Figure 3.1: The XRD patterns of undoped ZnO and all con 9:1 doped ZnO.	71
Figure 3.2: The schematic illustration of depositing dopant layer by conventional	



process and mixed ALD doping process.	78
Figure 3.3: XRD comparison for (a) same period length; (b) densely inserted mixed ALD doping; (c) same Hf content.	78
Figure 3.4: The ZnO films doped with a combination of conventional and mixed HfO ₂ dopant layers.....	88
Figure 3.5: The illustration and the nomenclature of structures with 1 period of mix 24:1 HZO and varied cycles of conventional HfO ₂ layer.	88
Figure 3.6: MGPC of (a) HfO ₂ on the surface of 24 cycles ZnO and (b) the first cycle ZnO on the various cycles of HfO ₂ acquired from in-QCM analysis.	89
Figure 3.7: Cross-sectional TEM images of the mix 24:1 HZO films inserted with (a) 3, (b) 5, (c) 7 cycles of the conventional dopant layer at each 1 period length (24 ZnO cycles/1 m-dopant cycle/24 ZnO cycles).....	89
Figure 3.8: The energy band alignment of ZnO and HfO ₂	90
Figure 3.9: The transportation of carriers in mix 24 / nH (a) $n < 7$; (b) $n = 7$; (c) $n > 7$	90
Figure 3.10: Cumulative lattice thermal conductivity of bulk ZnO at 300 K simulated by Karttunen et al. ¹⁰⁰	91
Figure 3.11: The nomenclature of structures which are isotope incorporated.....	98
Figure 3.12: The contribution ratio of each phonon modes in ZnO which is simulated by Wu et al. ¹⁰³	98

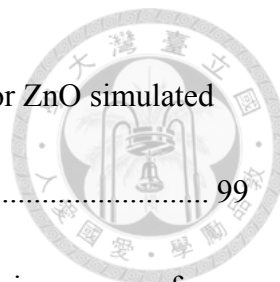


Figure 3.13: The phonon group velocity as a function of frequency for ZnO simulated by Wu et al. ¹⁰³	99
Figure 3.14: The simulation done by Wang et al. ¹⁰⁴ (a) phonon dispersion curves of wurtzite ZnO; (b) vibrational density of states of wurtzite ZnO.	99

Chapter 4

Figure 4.1: The photographs of deposited PEDOT films and blank glass substrates...	106
Figure 4.2: The FITR spectrum of deposited PEDOT films.	106
Figure 4.3: The UV-Vis spectrum of deposited PEDOT films.	107
Figure 4.4: The in-situ QCM results of the deposition of PEDOT on the surface of ZnO using two kinds of pulse sequences.	112
Figure 4.5: The cross sectional TEM images of deposited films in the structure of 6×(80-cycle ZnO/ 1-cyle PEDOT).	112
Figure 4.6: The mass gain of ZnO in steady-growth region and that on the surface of inserted PEDOT with various modifications.	113
Figure 4.7: The mass gain of H ₂ O on surface covered by redundant SbCl ₅	113
Figure 4.8: The XRD patterns of ZnO deposited by ALD and MLD systems.	124
Figure 4.9: The mean grain size calculation of mix 19:1 HZO by Scherrer equation..	125
Figure 4.10: The cross-sectional TEM images of HZO/PEDOT superlattices with (a) 1-	



cycle; (b) 6-cycle inserted PEDOT. 125

Figure 4.11: The schematic illustration of superlattice-structure and series-resistance model in our calculation. 125

Figure 4.12: The estimated interface thermal conductance in ZnO/hydroquinone/ZnO superlattice done by Ashutosh Giri et al. 126

Figure 4.13: The schematic illustration of energy band alignment of PEDOT and ZnO. 126

Figure 4.14: The photograph of 15 and 30nm polyaniline thin films on glass substrates. 129

Figure 4.15: The FTIR spectrum of ~30nm polyaniline. 129

Figure 4.16: The in-situ QCM results (a) deposition of polythiophene while pulsing thiophene twice; (b) pulse VOCl_3 alone; (c) increasing N_2 flow rate transiently. 131

Chapter 5

Figure 5.1: The QCM results by the usage of MC and piperazine in deposition of polyamide at varied deposition temperature (a) 100°C ; (b) 120°C 139

Figure 5.2: The QCM results by the usage of MC and 1,8-diaminooctane in deposition of polyamide at varied deposition temperature (a) 120°C ; (b) 100°C 139

Figure 5.3: The QCM results of 100-cycle polyamide deposited by the usage of MC and

1,8-diaminooctane at 100°C. The inset is the zoom-in of the mass gain at latter cycles.

..... 139

Figure 5.4: The FITR spectrum of polyamide deposited by the usage of MC and 1,8-

diaminooctane..... 140

Figure 5.5: The QCM result by the usage of terephthaloyl chloride and ED in deposition

of polyamide at 120°C..... 140

Figure 5.6: The QCM result of the multiple pulse of single precursor..... 141

Figure 5.7: The QCM result of polyamide by the usage of terephthaloyl chloride and ED

with re-nucleation layers. 141

Figure 5.8: The FITR spectrum of polyamide deposited by the usage of terephthaloyl

chloride and ED. 142

Figure 5.9: The QCM results of varied pulse time of EG (a) 0.02 s; (b) 0.10 s. The insets

are the mass gain at latter cycles. 147

Figure 5.10: The QCM result of polyester at 180°C with 0.02 s pulse of EG..... 147

Figure 5.11: The schematic illustration of single and double reaction in MLD..... 148

Figure 5.12: The reaction mechanism of the self-condensation of MC monomers..... 148

Appendix

Figure A.1: The QCM result of alucone with varied exposure time (a) without; (b) 5 s;

(c) 15 s of EG deposited at 105 °C. 166

Figure A.2: The cross-sectional SEM images of alucone film with the exposure of EG.

..... 166

Figure A.3: The TGA result of the SiO₂ nanoparticles. 167

Figure A.4: The TGA results of the SiO₂/alucone core-shell particles. 167

Figure A.5: The TGA results of the SiO₂/alucone core-shell particles after varied low-

temperature pyrolysis process. 168

List of Tables



Chapter 1

Table 1.1: The current progress in ALD ZnO thin film thermoelectric materials.	31
---	----

Chapter 2

Table 2.1: ALD parameters of depositing undoped ZnO.....	49
Table 2.2: ALD parameters of depositing conventional process metal ion doped ZnO.	49
Table 2.3: ALD parameters of depositing mixed ALD doping process metal ion doped ZnO.....	50
Table 2.4: MLD parameters of depositing polythiophene.....	53
Table 2.5: MLD parameters of depositing polyaniline.....	53
Table 2.6: MLD parameters of depositing PEDOT.	53
Table 2.7 MLD parameters of depositing polyester.	55
Table 2.8: MLD parameters of depositing polyamides.	55
Table 2.9: MLD parameters of depositing alucone at 105°C.	55

Chapter 3

Table 3.1: The thermoelectric characteristic of undoped ZnO, Ti:ZnO, Zr:ZnO and Hf:ZnO.....	69
---	----

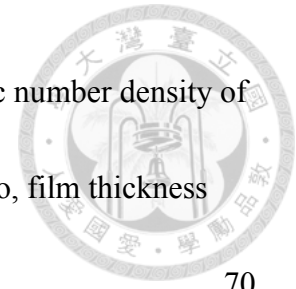


Table 3.2: The concentration of dopant measured by XPS and atomic number density of dopants. The number density is calculated by using composition ratio, film thickness and density ^{41,99}	70
Table 3.3: Bond energy of metal/ligand and metal/oxygen and the difference between bond energies ($\Delta BE = BE_{\text{metal/oxygen}} - BE_{\text{metal/ligand}}$)	70
Table 3.4: The thermoelectric characteristic of undoped ZnO, conventional process and mixed ALD doping process HZO	76
Table 3.5: The concentration of dopant measured by XPS and atomic number density of Hf. The number density is calculated by using composition ratio, film thickness and density	77
Table 3.6: The thermoelectric characteristic of the mix 24:1 HZO films inserted with 5-cycle conventional HfO ₂ layers at three periodicities (as illustrated in Figure 3.4)	86
Table 3.7: The thermoelectric characteristic of undoped ZnO and the films composed of 1 period of mix 24:1 HZO and varied cycles of conventional HfO ₂ layer	87
Table 3.8: The electrical characteristic, thickness and the refractive index of mix 24 / 7H- ¹⁶ O, mix 24 / 7H- ¹⁸ O and modified mix 24 / 7H- ¹⁸ O	93
Table 3.9: The thermoelectric characteristic of undoped ZnO, mix 24 / 7H and ¹⁸ O incorporated superlattice	97



Chapter 4

Table 4.1: The characteristic of deposited PEDOT films.	106
Table 4.2: The electrical conductivity of PEDOT/HZO superlattice with various modifications in the structure of 6×(4 periods mix 19:1 HZO + 1-cycle PEDOT)	112
Table 4.3: The electrical properties of ZnO and mixed HZO with varied insertion periodicity of mixed doping layers.	123
Table 4.4: The thermoelectric characteristic of the HZO/PEDOT superlattice films with varied periodicities of mix 19:1 HZO host layers.	123
Table 4.5: The thermoelectric characteristic of the HZO/PEDOT superlattice films composed of alternating 4 periods of mix 19:1 HZO and varied cycles of PEDOT. ...	124
Table 4.6: The relevance of polyaniline growth rate on the temperature of SbCl ₅	129

Chapter 5

Table 5.1: The structure of precursors, polymers and deposition temperatures in the deposition of polyamides.	138
Table 5.2: HeTR of varied samples before/after damp-test (85°C, 85%RH, 36 hours) and WVTR of superlattice-based gas barrier. The unit of HeTR and WVTR is cc day ⁻¹ m ⁻² and g day ⁻¹ m ⁻² , respectively.	145



Chapter 1

Introduction

1.1 Overview of thermoelectricity

According to Quadrennial Technology Review 2015 from the United States Department of Energy, it is estimated that around 20~50% of industrial energy use becomes waste heat (e.g. hot exhaust gases, hot equipment surface and the heat pump away by cooling systems) and is then discharged into the environment¹. Besides, household electrical appliances and personal portable devices also produce waste heat during operation. Recycling of such waste heat into useable energy will greatly reduce energy consumption and lessen the environmental impacts of industrial productions.

Thanks to its considerable advantages, such as scalability, reliability, zero extra energy input and no contamination, thermoelectric power generation is one of the best methods for recycling waste heat². Thermoelectricity (TE) is a physical phenomenon where heat is converted into electrical energy directly, and vice versa. The TE effect was first discovered by Italian scientist Alessandro Volta, and then became widely known thanks to the work of Baltic German physicist Thomas Johann Seebeck³. A schematic illustration of the operating principle of the TE effect is shown in Figure 1.1. When a temperature gradient is applied to a TE material, the temperature gradient induces a

chemical potential gradient of the charged carriers. The chemical potential gradient makes the charged carriers flow and then accumulate respectively at the hot and cold end of the TE material to form an electromotive force (EMF). The formed EMF can output electrical power if the ends of the TE material are attached to devices, thereby converting waste heat into useable electrical energy directly.

The efficiency of the thermoelectric effect of a material can be quantified by a figure of merit, ZT , which is defined as $ZT = \frac{S^2 \sigma}{\kappa} T$, where S is the Seebeck coefficient, which is the ratio of the formed EMF over the applied temperature difference ($-\frac{\Delta V}{\Delta T}$); σ the electrical conductivity of the material, κ the thermal conductivity, and T the absolute temperature.

As a high efficiency TE material, three properties are required. First, a high absolute value of Seebeck coefficient, which offers a high EMF to output electrical work, is required. Second, a high electrical conductivity ensures a low energy dissipation as Joule heat during operation. Third, a low thermal conductivity is able to maintain not only high but also consistent temperature difference between the two ends of the material. In general, $ZT > 1$ is the criterion to determine whether a TE material is practically usable or not. The summary of some common bulk n-type and p-type TE materials with high ZT values is shown in Figure 1.2.

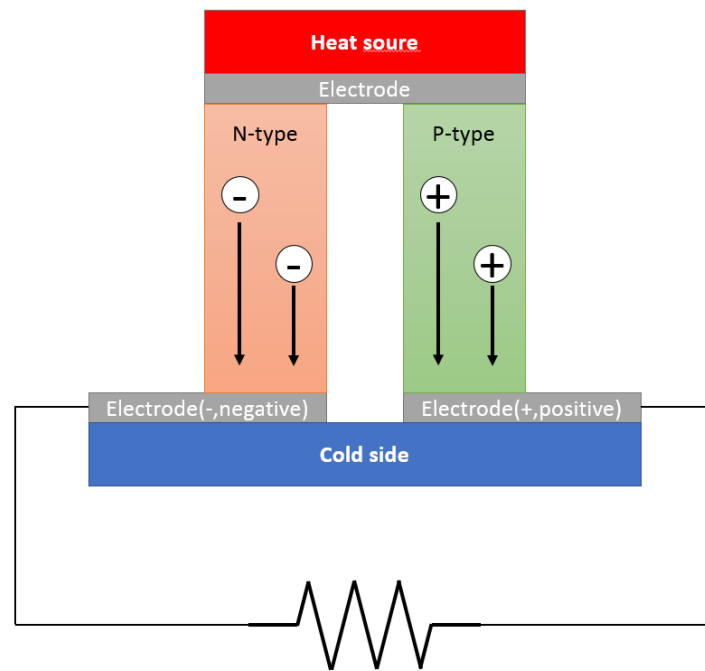


Figure 1.1: Operating principle of TE materials.

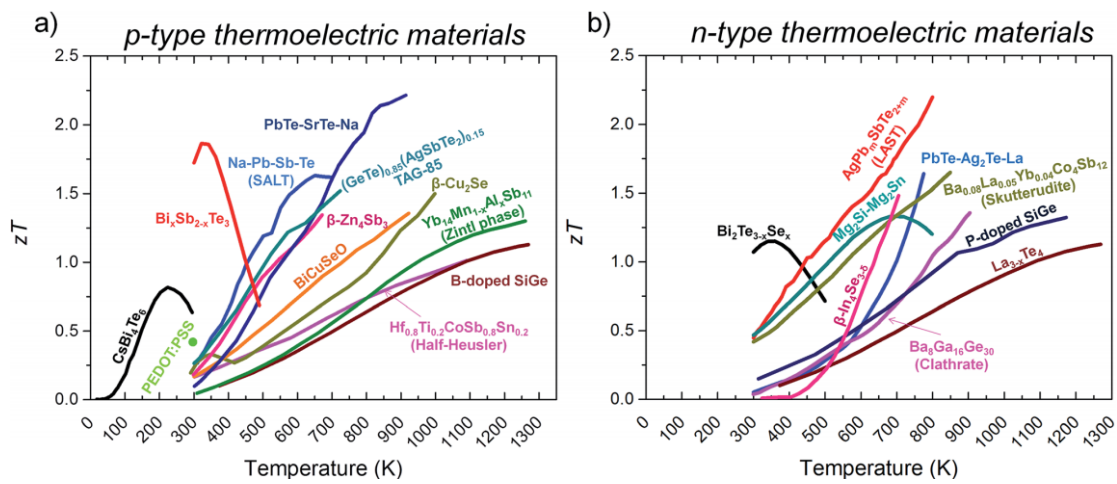
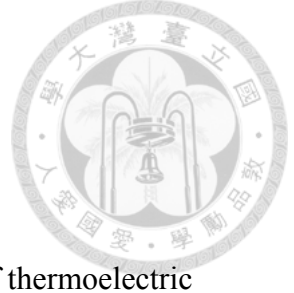


Figure 1.2: Best ZT value for bulk n-type and p-type TE materials.



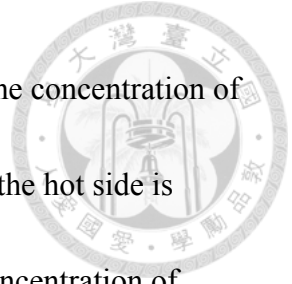
1.2 Fundamental of thermoelectric effect

1.2.1 Origin of thermoelectric effect

In this section, we use a qualitative way to deduce the origin of thermoelectric effect. First, a material with a finite thin thickness is divided into three parts, and each part is named as Contact1, Channel and Contact2, respectively. The schematic illustrations of qualitative derivation are shown in Figure 1.3, Figure 1.4. and Figure 1.5.

When the temperature is homogeneous inside the entire material, the Fermi levels are the same at Contact1 and Contact2. However, when the thermal energy is applied to the material from a single side, a temperature gradient is created across the material. Here, we assume that Contact1 is the hot side and Contact2 is the cold side. A portion of electrons at the hot side gains sufficient kinetic energy and then is able to transit to the higher energy states. In this transition process, the distribution of electrons over energy states at particular temperature is described by Fermi-Dirac distribution, $f(E) = \frac{1}{e^{\frac{E-\mu}{k_B T}} + 1}$ where k_B is Boltzmann's constant, T is the absolute temperature and μ is the chemical potential of electrons (i.e. Fermi energy). Also, the carrier concentration is known as the product of Fermi-Dirac distribution and density of states (DOS) of charged carriers.

Next, three situations with regard to the DOS over energy states near Fermi energy level are discussed as follows.



(1) The constant DOS over the energy states: In this situation, the concentration of electrons whose energy are higher than the Fermi energy in the hot side is greater than those in the cold side. On the other hand, the concentration of electrons whose energy are lower than the Fermi energy in the cold side is greater than the one in the hot side. However, the absolute values of concentration differences in this condition are the same. Hence, there is no net electron flow in the materials, which means that thermoelectric effect is absent in this kind of the materials.

(2) The DOS increases with energy: In this case, the absolute value of the difference in the electron concentration between the hot end and the cold end for electrons whose energy is higher than the Fermi energy is greater than the one lower than the Fermi energy. Hence, there is a net electron flow from the hot end to cold end and then it forms an EMF. By the definition: $S = -\frac{\Delta V}{\Delta T}$, the Seebeck coefficients of the materials whose DOS increasing with energy are negative; thus, materials are called as n-type materials.

(3) The DOS decreases with energy: Contrary to situation (2), there is a net electron flow from cold end to hot end and then it forms EMF. The Seebeck coefficients for this type of materials are positive, and thus they are referred to p-type materials.



Initial condition : Thermal equilibrium



Temperature gradient is created



Figure 1.3: Illustration of model for deducing.

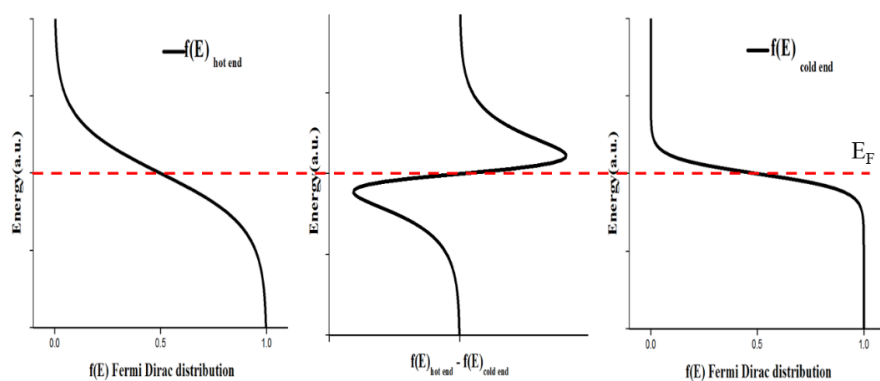


Figure 1.4: The Fermi Dirac distributions at each end and difference between them.

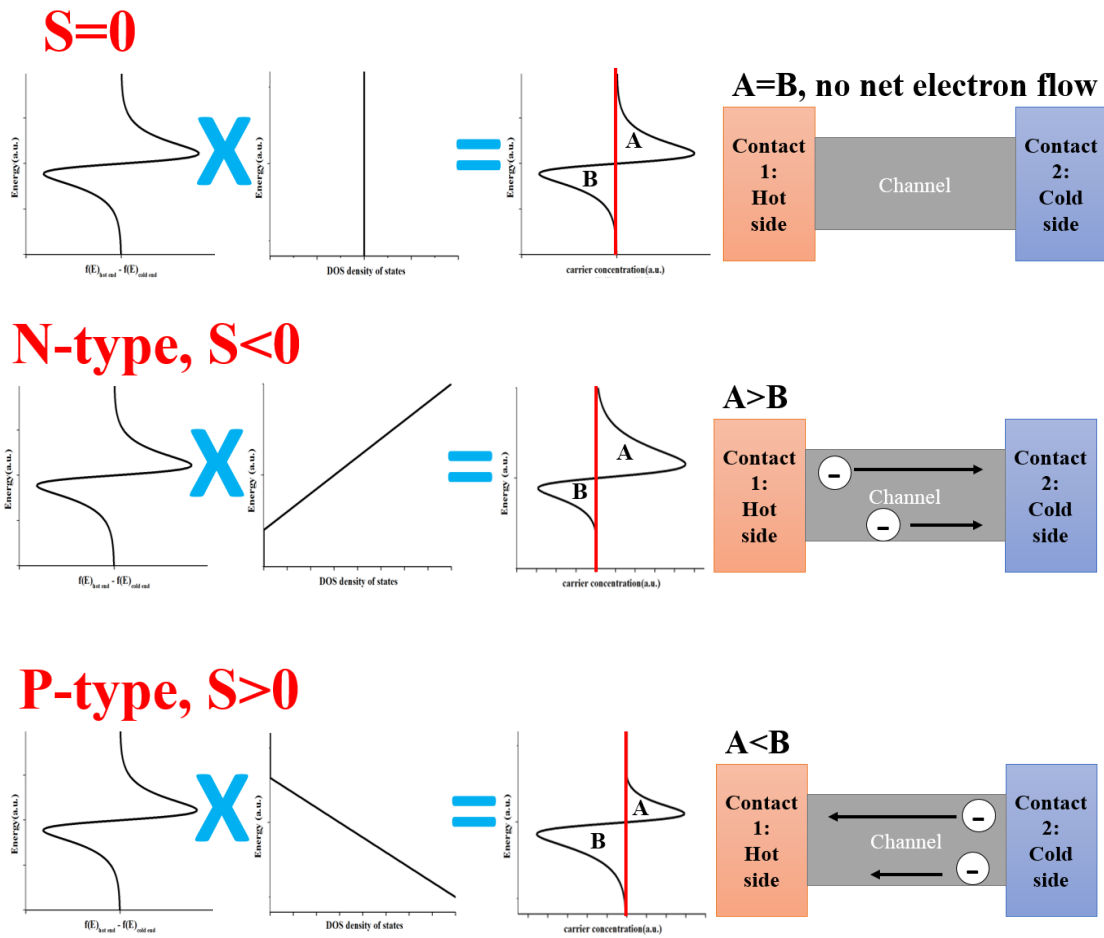
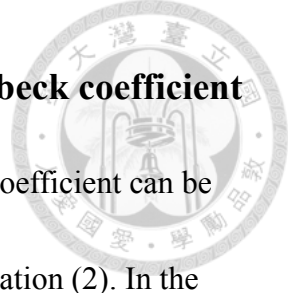


Figure 1.5: The dependence of Seebeck coefficient on DOS over energy states.



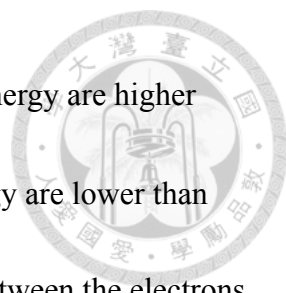
1.2.2 Trade-off between electrical conductivity and Seebeck coefficient

The relationship between electrical conductivity and Seebeck coefficient can be described by Mott formula⁴, which is shown in Equation (1) and Equation (2). In the equations, k_B is the Boltzmann's constant, T is the absolute temperature, μ is the chemical potential of electrons (i.e. Fermi energy) and $c(E)$ is called as the energy-dependent conductivity, which is the product of the energy-dependent mobility $\mu(E)$ and the DOS.

$$\sigma = \int c(E) \left(-\frac{df(E)}{dE} \right) dE \dots \dots \dots (1)$$

$$S\sigma = \frac{k_B}{-e} \int \frac{E-\mu}{k_B T} c(E) \left(-\frac{df(E)}{dE} \right) dE \dots \dots \dots (2)$$

In Mott formula, the term $\left(-\frac{df(E)}{dE} \right)$, which can also be called as the Fermi window, is the differential of the Fermi-Dirac distribution with respect to energy. The value of the Fermi window is non-zero only within the range of several $k_B T$ around the Fermi level. In addition, this function is symmetric about the Fermi level. The illustration of the Fermi window is shown in Figure 1.6. It implies that the electrical conductivity and the Seebeck coefficient of a material are only determined by the electrons whose energy is around the Fermi level. From Equation (1), we can realize that all electrons within the Fermi window make positive contributions to the electrical conductivity. Hence, the more electrons within Fermi window are, the more conductive materials become. On the other hand, as mentioned in section 1.2.1 and learned from the



term $\frac{E-\mu}{k_B T}$ in Equation (2), the contribution of the electrons whose energy are higher than the Fermi energy are cancelled out by the electrons whose energy are lower than the Fermi energy. For this reason, a great concentration difference between the electrons whose energy are higher and lower than the Fermi energy is required for the high absolute value of Seebeck coefficient. However, owing to the symmetry characteristic of the Fermi window about the Fermi energy, the conditions for achieving high electrical conductivity and absolute value of Seebeck coefficient are hard to meet simultaneously.

Take n-type materials as examples, the schematic illustration is shown in Figure 1.7. First, we make an assumption that the energy-dependent mobility $\mu(E)$ is near constant over energy. When the Fermi energy of a material is near the bottom of the conduction band, only several free electrons exist inside the conduction band and are able to make contributions to the electrical conductivity due to the low DOS near the bottom of conduction band. However, the low symmetry of DOS near the bottom of conduction band ensures a high absolute value of Seebeck coefficient. In contrast, the number and the symmetry of DOS become higher when the Fermi level arises and goes deep into the conduction band. Although a high electrical conductivity is achieved by increasing the number of DOS, the high symmetry of DOS diminishes the absolute value of Seebeck coefficient. Hence, only a few materials with a special DOS

distribution or an energy-dependent mobility $\mu(E)$ within the Fermi window are able to address the trade-off issue of Seebeck coefficient and electrical conductivity.

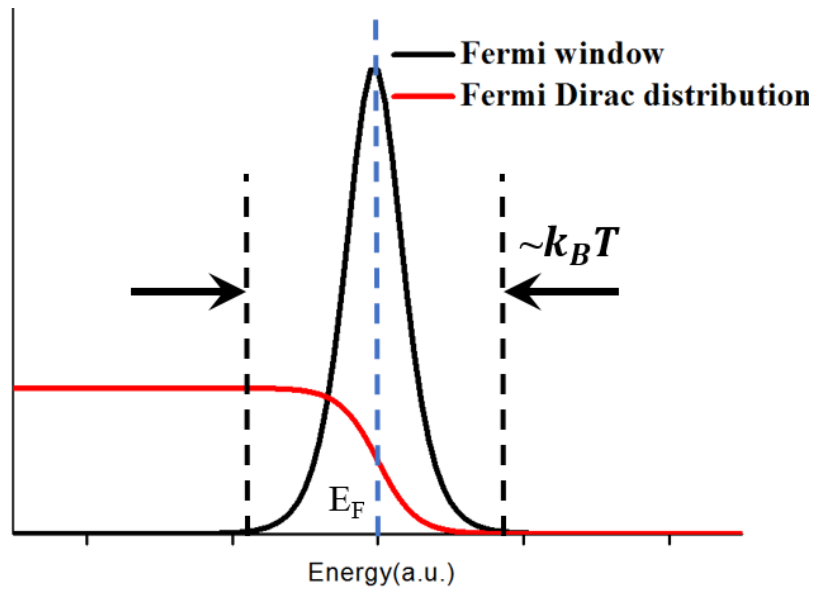


Figure 1.6: Fermi window and Fermi-Dirac distribution.

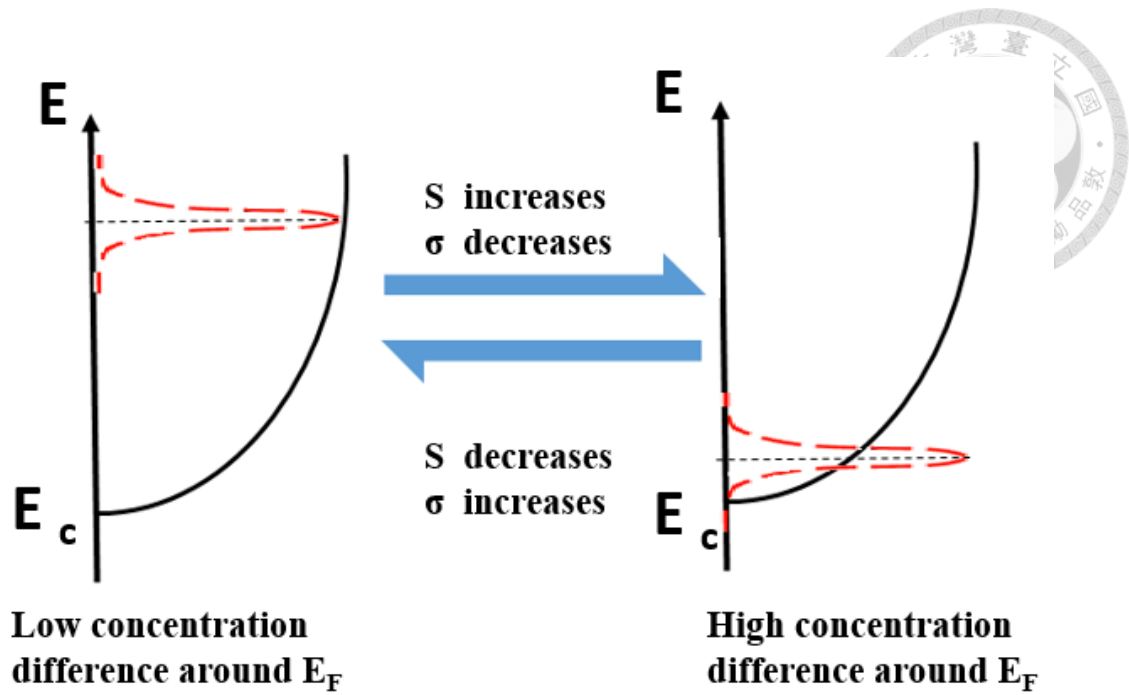


Figure 1.7: Tendency of Seebeck coefficient and electrical with regard to the location of Fermi window.

1.2.3 Thermal conductivity of materials

The thermal conductivity is a parameter to describe the ability of thermal energy transmitting through materials by the heat carriers. Typically, the thermal conductivity of a material is made up of two parts, one is the contribution from the charged carriers, i.e. electrons or holes, and the other is attributed to the phonons, i.e. lattice vibration.

Mathematically, the thermal conductivity of a material can be expressed as $\kappa_{total} = \kappa_{el} + \kappa_{ph}$. The contribution of each parts to thermal conductivity is shown in Figure 1.8.

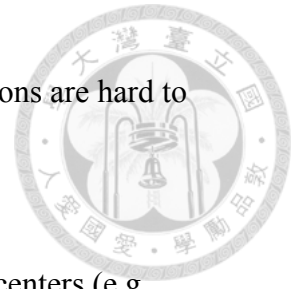
For the contribution from electrons, it is proportional to the product of the electrical conductivity and the absolute temperature, which can be described by

Wiedemann–Franz law, i.e. $\kappa_{el} = \sigma LT$, the proportional constant L is known as Lorenz constant and equals to $2.44 \times 10^{-8} \text{ W}\Omega\text{K}^{-2}$. For materials with high electrical conductivities, such as metals and heavily doped semiconductors, κ_{el} dominates the thermal conductivities of those materials. However, it shows little effect on typical semiconductors and is even negligible in insulators.

In the materials, the atoms vibrate around their equilibrium position as long as $T \neq 0 \text{ K}$. The vibration of an atom couples with that of neighbor atoms strongly, forming the lattice vibration, which is the sum of vibrations from those atoms and is characterized by a standing wave. Next, the quantized lattice vibrations are known as “phonons”, which are quasiparticles. The process of transporting thermal energy can be viewed as the transmission of the phonons from one side to the other side through materials. In the following, the factors influencing the transportation of phonons are introduced:

- (1) Weight of atoms: Be analogues to classical harmonic oscillator, vibration frequency reduces when the weight of atoms raises. For this reason, it reduces the transmission speed of phonon, and then reduces the thermal conductivities of materials.
- (2) Microstructure and type of bonds: With the loose bonds between atoms and the disordered microstructure, i.e. amorphous, the vibration of an atom weakly

couples with those of neighbor atoms. For this reason, phonons are hard to propagate inside materials.



- (3) Phonon scattering: When phonons encounter the scattering centers (e.g. dopants, dislocation, grain boundary, mass difference interfaces) during transmitting, the transmitting direction of phonons changes. Hence the transmission of phonons is impeded as long as phonon the scattering centers exist inside the materials. Depending of the type and the characteristic, the scattering centers can be categorized into phonon-phonon scattering, impurity scattering, boundary (or interface) scattering and phonon-electron scattering.

1.2.4 The figure of merit, ZT

The figure of merit of the thermoelectric materials is described as $ZT = \frac{S^2 \sigma}{\kappa} T$.

From the above introduction, we can realize that the high absolute value of Seebeck coefficient, the high electrical conductivity and the low thermal conductivity are required for achieving high ZT. A high absolute value of Seebeck coefficient ensures a large outputting EMF; a high electrical conductivity guarantees a low energy dissipation as Joule heating; a low thermal conductivity ensures a high and consistent temperature difference. Normally, power factor, i.e. $S^2 \sigma$, represents the figure of merit in the electrical part and can be tuned by doping. Form the calculation by G. Jeffrey Snyder and Eric S. Toberer⁵, it showed that the good thermoelectric materials are typically the heavily doped semiconductors with a carrier concentration between 10^{19} and 10^{20} carriers per cm^3 . The schematic illustration of optimizing ZT through carrier concentration tuning is shown in Figure 1.9.

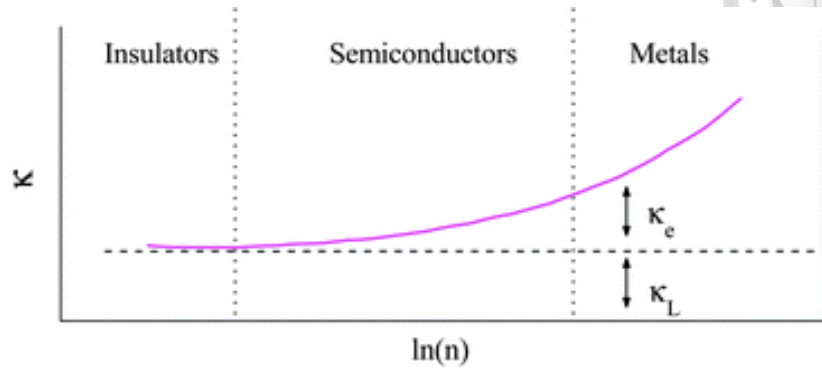


Figure 1.8: Contribution of κ_{el} and κ_{ph} to κ_{total} for different types of materials.

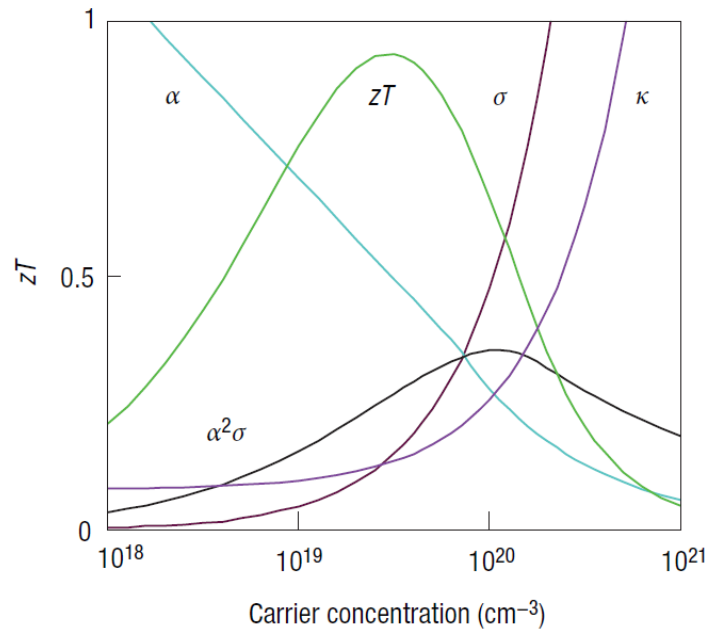


Figure 1.9: The optimization of ZT through carrier concentration tuning. In the picture, α (0 to 500 $\mu\text{V/K}$) represents the absolute value of Seebeck coefficient; σ (0 to 5000 S cm^{-1}) is the electrical conductivity; κ (0 to 10 $\text{W m}^{-1} \text{K}^{-1}$) is the thermal conductivity⁵.



1.3 Thermoelectricity in thin films

1.3.1 Size effect

In the past decades, the progress of increasing the ZT of the thermoelectric materials was retarded owing to the interdependence of each parameter. As mentioned in section 1.2.1 and 1.2.2, if we enhance the electrical conductivity by doping, the suppression of the absolute value of Seebeck coefficient is accompanied; besides, the thermal conductivity also increases due to the contribution from increasing κ_{el} . From this reason, ZT may decrease unexpectedly.

However, the emerging nanotechnologies offer opportunities to break through the current predicaments. By reducing the dimension of the materials, it shows a great potential to overcome the difficulty of the interdependence of parameters⁶. Since it is able to engineer the density of states for electrons straightforwardly without changing the composition elements. For example, it may destroy the high symmetric characteristic of DOS in the Fermi window while the Fermi level goes deep into the conduction band, but still offers amounts of DOS. In this case, the high absolute value of Seebeck coefficient and the high electrical conductivity are obtained in the meantime. The schematic diagram of the density of states for electrons in different dimension based on parabolic band structure is shown in Figure 1.10. Besides the benefits to electrical performance, the size effect also increases a large number of boundary

scatterings, which reduce thermal conductivity greatly, to reduce the thermal conductivity. Overall, reducing the dimension of the materials is a promising way to enhance the figure of merit of thermoelectric.



1.3.2 Superlattice(Nanolaminates)

Thanks to the emerging nanotechnology, we can not only reduce the dimension of materials but also design and introduce some nanostructures into the materials, such as nanoinclusions⁷⁻¹², nanopores¹³⁻¹⁶. Among these novel nanostructures, the superlattice (nanolaminates) shows a great ability to enhance the figure of merit, ZT^{17-22} .

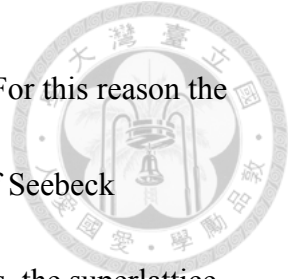
Nanolaminates are referred to the materials whose structures are made up of several kinds of base materials with different properties (e.g. composition elements, density, hardness and thermal conductivity.) alternatively and periodically in nanoscale. If the base materials are crystalline but in the different crystal structures, the nanolaminates can also be called as the superlattice. However, these two terms can replace with each other generally, so we use the term “superlattice” in this dissertation for convenience.

First, the complete and layered interfaces are able to suppress the thermal conductivity more effectively compared to the random distributed heterogeneous structure. As mentioned in section 1.2.3, the scattering centers inside materials retard the transport of phonons. For superlattice, when the interfaces are perpendicular to the

direction of heat transferring, the phonons with particular wavelength may undergo destructive interference completely according to the period length of interfaces. Consequently, the contribution to thermal conductivity of the phonons with particular wavelength vanishes. From this concept, we may filter out the phonons which offer major contribution to thermal conductivity by tuning the periodicity of interfaces even introducing multi-periodicity into the materials to reduce the thermal conductivity of superlattice effectively.

Second, the superlattice also offers an unparalleled way to overcome the entanglement of the electrical conductivity and the absolute value of Seebeck coefficient. Energy filtering effect, which can block the transmission of low energy carriers, occurs at the interfaces of two materials with the diverse transportation characteristic of charged carriers^{23–27}. The schematic diagram of energy filtering effect is shown in Figure 1.11. Once again, the reduction of the absolute value of Seebeck coefficient is accompanied with the enhancement of electrical conductivity via doping, which makes the Fermi level goes deep into the conduction band for n-type materials. However, if the energy barriers are placed along the transmitting direction of charged carriers, the low energy carriers no longer make contribution to the electrical conductivity and Seebeck coefficient. Though the enhancement of electrical conductivity is suppressed slightly, great mounts of carriers with energy higher than the

Fermi level still make positive contributions to Seebeck coefficient. For this reason the enhancements of the electrical conductivity and the absolute value of Seebeck coefficient are obtained in the meanwhile. Owing to these advantages, the superlattice becomes the new paradigms in developing high ZT thermoelectric materials.

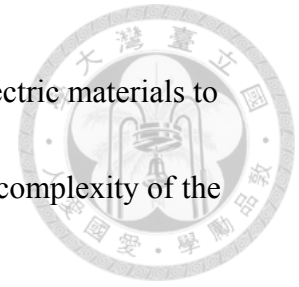


1.3.3 Advantages of thin film thermoelectric materials

As the growing usage of personal portable devices, the management and the recycling of waste heat in the ever-shrinking electronic devices have drawn much attentions nowadays. However, as the high performance bulk type thermoelectric materials are no longer suitable for the use in portable devices owing to the limited shape characteristic^{28–31}. Therefore, the developments of nanoscale thermoelectric materials are demanded urgently. After years of effort, the progress in nanoscale thermoelectric materials has been made.

In the current results, nanowires^{32–35} and quantum-dots^{21,36–39} thermoelectric materials show excellent characteristics. Nevertheless, the packing density and the binding materials which provide the electrical conducting pathways and the mechanical strength still have to be taken into consideration in practical use. For this reason, the usages of extra materials and process are necessary to fabricate thermoelectric devices.

Hence, the usages of nanowire type and quantum-dot type thermoelectric materials to recycle the waste heat or cool the system increase the difficulty and complexity of the microminiaturized electronic device process.



On the other hand, the thin films thermoelectric materials, which also show promoted thermoelectric properties, are physically continuous and thus the complete materials, so the supporting materials are no longer required. In addition, the thin film deposition process are already utilized in the current semiconductor industry extensively. Thus, the thin film thermoelectric materials are the best type of nanomaterials to recycle the waste heat and cool the system in microminiaturized electronic device. Among the current thin film deposition techniques, atomic layer deposition (ALD) shows a great potential for developing high performance thin film thermoelectric materials, since ALD is the emerging thin film deposition technique in semiconductor industry and possesses unparalleled the precise control over thickness and composition. These advantageous ensure the feasibility in practical use and the capability to fine tune the properties of deposited thin films.

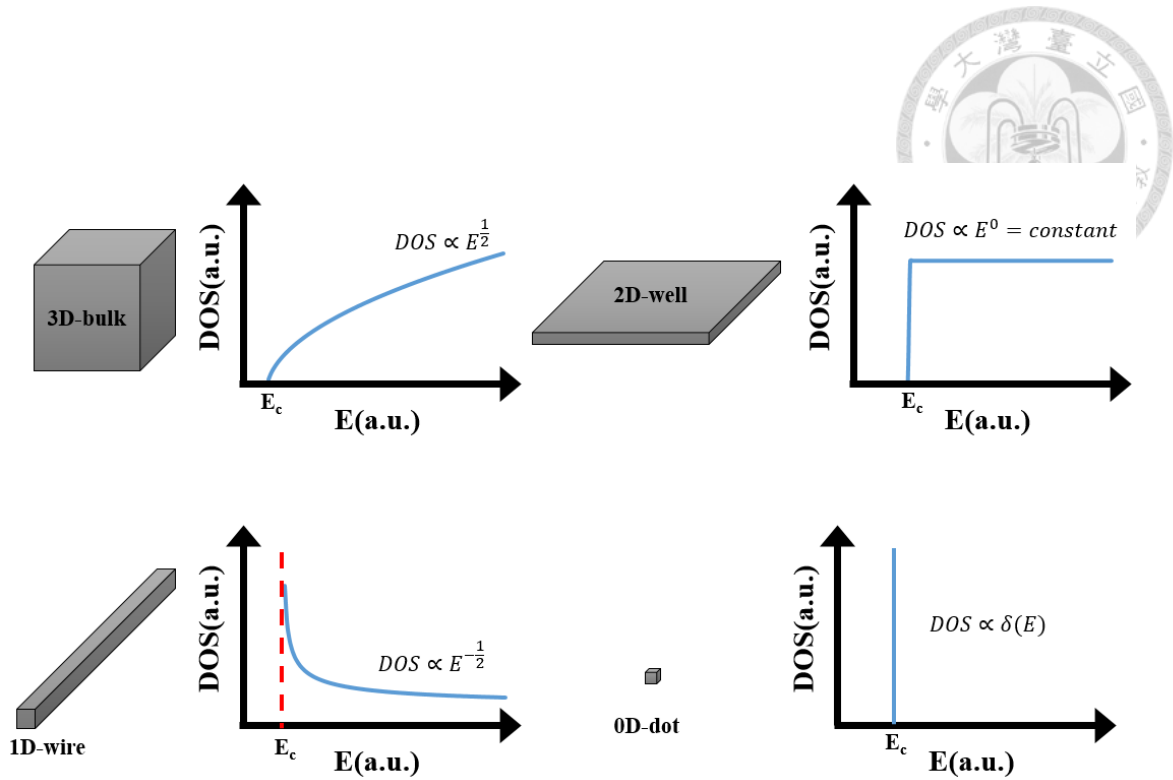


Figure 1.10: The schematic diagram of the density of states for electrons in different dimension based on parabolic band structure.

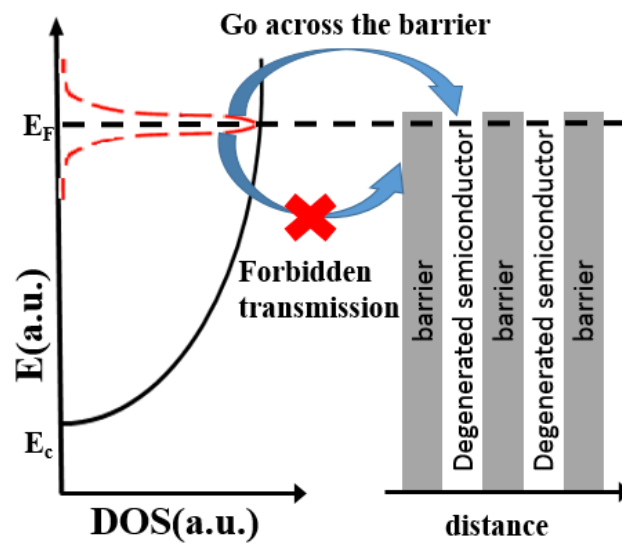


Figure 1.11: The schematic diagram of energy filtering effect in superlattice.

1.4 Fundamental of atomic layer deposition and its advantages of depositing thin film thermoelectric materials



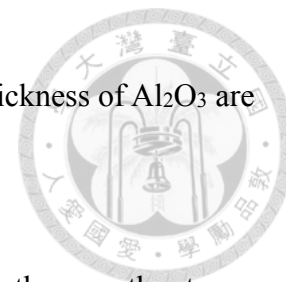
1.4.1 Atomic layer deposition(ALD)

Atomic layer deposition, which is a unique type of chemical vapor deposition (CVD), has drawn much attention in the recent years owing to its unique self-limiting growth characteristic. It utilizes two sequential self-limiting surface reactions between the vapors of precursors and the surface functional groups to deposit thin films. Take the deposition of Al_2O_3 as an example, the schematic illustration of film-growth mechanism is shown in Figure 1.12. The reaction steps are described as below:

- (1) Trimethylaluminum, TMA, is introduced into reaction chamber and then reacts with the hydroxyl groups on the surface of substrate.
- (2) The physisorbed TMA and the reaction byproducts, i.e. methane, are removed during N_2 purge step.
- (3) H_2O is introduced into reaction chamber and then reacts with the surface methyl groups.
- (4) Once again, the physisorbed H_2O and the reaction byproducts are then removed during N_2 purge step.

The TMA dose - N_2 purge - H_2O dose – N_2 purge, these four steps are called as one cycle of ALD Al_2O_3 growth, which can form about 1 angstrom Al_2O_3 . For growing

Al₂O₃ thin films, the reaction cycles are repeated until the desired thickness of Al₂O₃ are deposited.



Self-limiting, the unique characteristic of ALD reaction, makes the growth rate per cycle unchanged while increasing the dose amount of precursors and prolonging the purge time. This characteristic ensures following advantages: the defect-free deposition, the complete and uniform coverage over the surface with a high aspect ratio surface feature, the precise control over the film thickness and the elemental composition⁴⁰.

Besides the selection of precursors, the deposition temperature also plays an important role to achieve self-limiting characteristic in ALD process. Since ALD growth only occurs within a particular temperature window (ALD window). The illustration of the dependence of growth rate per cycle on the temperature is shown in Figure 1.13.

When the temperature is below ALD window, there are two situations. One is that the precursors may condense on the surface easily, and then it causes a higher growth rate per cycle. The other one is that reactions between the precursor and the surface functional groups are limited by the low kinetic energy, and then it cause a lower growth rate per cycle. On the other hand, when the temperature is above ALD window, there are also two situations. The first one is that the precursors may thermally decompose and the undesired reactions occurs, which raise growth rate per cycle. The second one is that the chemisorbed precursors tend to desorb form the surface, and then the lower growth

rate per cycle is obtained.

After years of effort, the deposition of various materials by ALD technique (e.g. metal oxide^{41–43}, metal nitride^{44–46}, metal sulfide^{47,48}, pure metal⁴⁹) have been demonstrated, and these thin films are successfully applied to varied applications, such as electronics, optoelectronics and biomedicine.



1.4.2 Molecular layer deposition(MLD)

Molecular layer deposition is a unique type of ALD. For traditional ALD, it focuses on the deposition of inorganic materials. However, MLD is referred to the deposition of pure organic polymers or organic-inorganic hybrid materials. Similar to ALD, MLD is also composed of two sequential self-limiting reactions. The deposition of pure organic polymers (e.g. polyamide, polyester and polyimide) have been extensively studied^{50–53}. Here, we take the deposition of polyester as an example to illustrate the growth mechanism. The schematic illustration is shown in Figure 1.14. In the first step, multifunctional carboxylic acid is introduced into the reaction chamber and then reacts with the surface hydroxyl groups. In the following N₂ purge step, the excess unreacted monomers and the reaction byproducts are removed. Next, polyol is introduced and reacts with the surface carboxyl groups. In the last step, N₂ purge the

surface to remove the excess unreacted polyol and the reaction byproducts. These four steps compose one cycle of MLD polyester growth.



As mentioned before, MLD is also developed to deposit organic-inorganic hybrid materials. The most iconic one is metalcone^{54–57}. Take the deposition of alucone as an example, the reaction mechanism is almost as the same as the one of ALD Al₂O₃, the only one difference is that the polyol substitutes for H₂O to reaction with the surface methyl groups and offers the surface hydroxyl groups. After cycles of MLD alucone deposition, organic-inorganic hybrid material with special linkage $\left(\text{Al}-\text{O}-\text{R}-\text{O} \right)_n$ is formed.

From the aspect of the growth mechanism, ALD and MLD are compatible to each other by selecting particular precursors with proper functional groups. Owing to the great control of composition, i.e. ratio of organic parts to inorganic parts, the combination of ALD and MLD techniques is not only simplify the manufacturing process of organic-inorganic multilayer hybrid materials but also able to fine tune the characteristics (e.g. hardness, refractive index, gas permeability and thermal conductivity) of the deposited hybrid materials^{58–61}. The detailed introduction to applications of ALD/MLD superlattices (or nanolaminates) other than thermoelectric are stated in section 1.6.

1.4.3 Advantages of ALD on depositing thin film thermoelectric materials



As mentioned in section 1.2.4, the doping is a general technique to enhance the electrical conductivity of a semiconductor. However, a precise control of doping level is required to find out the best combination of electrical conductivity and Seebeck coefficient, which offers the highest power factor (PF), i.e. $\sigma \times S^2$. Thanks to the layer-by-layer growth in atomic scale, ALD technique offers an unparalleled precise control of element concentrations, which is able to fine tune electrical conductivity, over other thin film deposition techniques. In addition, the layered and complete host-guest heterogeneous interfaces inside the superlattice are believed to impede the transport of phonons in materials effectively due to the severe phonon scatterings which are resulted from the phonon transportation property difference between the host material and the guest material (e.g. density, vibrational constant and coordination). Hence, the thermal conductivity of a material with the layered distribution of guest material decreases more drastically compared with the one with random distribution. Moreover, the ability to fine tune the thickness of entire film and basis materials is able to bring the size effect and the energy filtering effect into full play. Besides, attributed to the fine integration of ALD and MLD deposition process, the novel organic-inorganic superlattices are able to be deposited, and thus thermoelectric properties of them can be explored. With these

advantages, ALD and MLD are the promising techniques to develop the thin film thermoelectric materials.

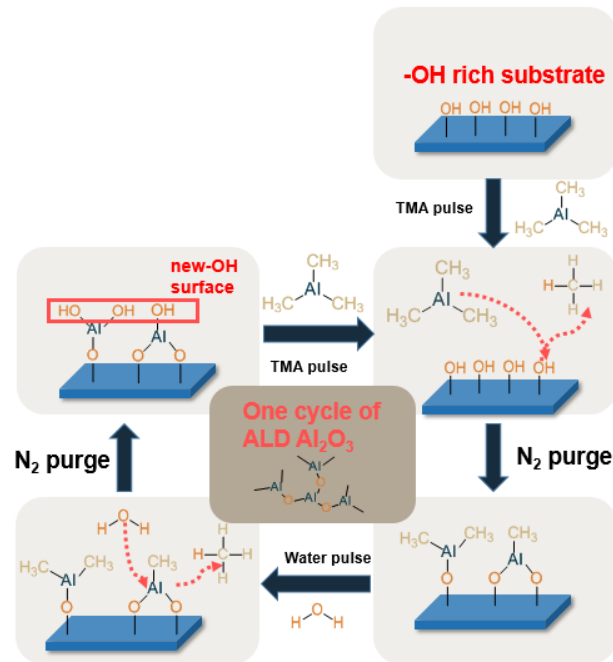


Figure 1.12: The schematic illustration of ALD film growth mechanism.

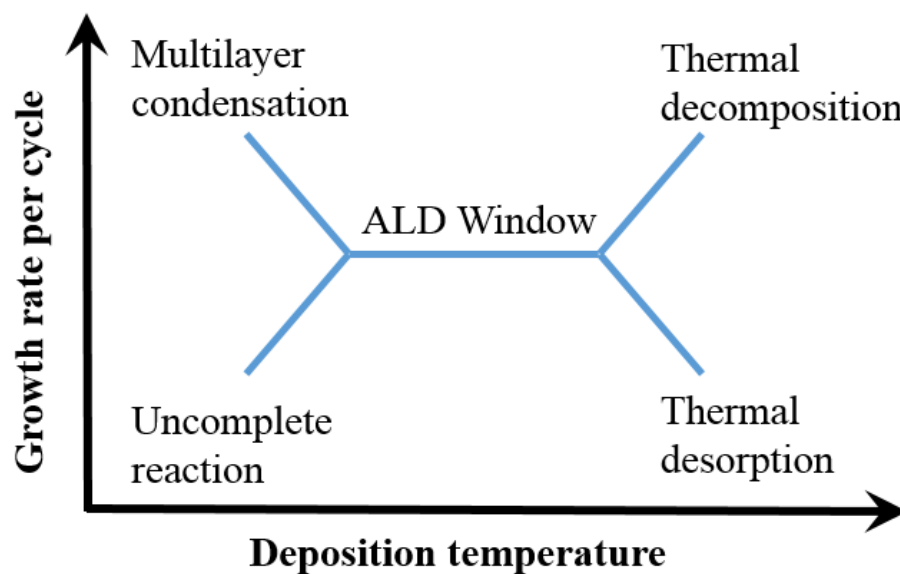


Figure 1.13: ALD window, the dependence of growth rate per cycle on temperature.

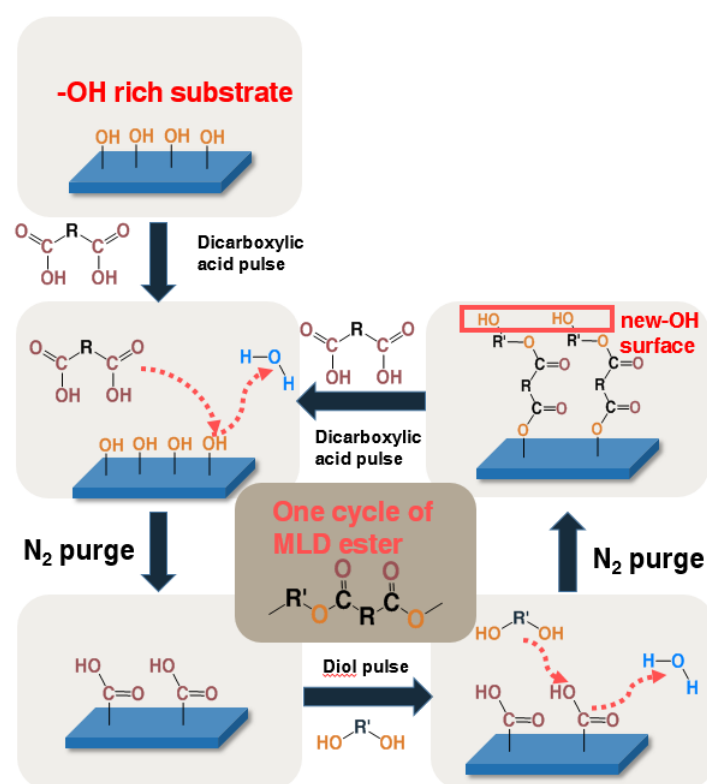



Figure 1.14: The schematic illustration of MLD polyester film growth mechanism.

1.5 Literature review of thin film thermoelectric materials deposited by ALD



To date, the depositions of several traditional bulk type thermoelectric materials by ALD have been successfully demonstrated. $\text{Bi}_2\text{Te}_3/\text{Sb}_2\text{Te}_3$ superlattices were deposited by Nminibapiel et al.⁶² The deposition of PbTe/PbSe superlattice was reported by Zhang et al.⁶³ and Sarnet et al. also demonstrated the deposition of Bi_2Te_3 by the usage of the novel synthesized in-house precursor $(\text{Et}_3\text{Si})_2\text{Se}$ ⁶⁴. Recently, Bi_2S_3 was also deposited by Mahuli et al.⁶⁵. However, few selections of precursors suppress the tunability of process, and then make it hard to fine tune the properties of materials. Moreover, the low reactivity (e.g. BiCl_3 and SbCl_3) and the low volatility (e.g. lead(II)bis(2,2,6,6-tetramethyl- 3,5-heptanedionato), $\text{Pb}(\text{C}_{11}\text{H}_{19}\text{O}_2)_2$ and bismuth(III) bis(2,2,6,6-tetramethylheptane-3,5-dionate), $\text{Bi}(\text{thd})_3$) precursors also reduce the robustness and reproducibility of the ALD processes. Besides, the traditional bulk type thermoelectric materials are disputed owing to containing scarce and toxic elements. Therefore, the traditional bulk type materials are not able to exert the potential of ALD (e.g. fine tune the electrical conductivity via doping process and the period length of superlattice) and then are used as next the generation thin film thermoelectric materials. Hence, it is important to choose a robust test-vehicle material to verify the advantages of ALD in developing thin film thermoelectric materials systematically.



ZnO (zinc oxide), which is earth abundant, environmental friendly, suitable band gap and crystal structure (direct band gap ~ 3.3 eV at 300 K and hexagonal wurtzite structure), has been considered to be the next generation thermoelectric material. The thermoelectric properties of ZnO fabricated by traditional ways (e.g. sputtering, sol-gel and powder sintering) have been extensively studied. Moreover, its ALD process is already well established and applied to varied applications, such as thin-film transistors^{66,67}, transparent conducting oxide^{68,69}, gas sensor^{70,71}, the electron transporting layers in OPVs^{72,73}. Hence, ZnO is promising in demonstrating the capability of ALD in the thin film thermoelectric materials. The Table 1.1 summarizes the current progress in ALD ZnO thin film thermoelectric materials. Among the current results, Gallium showed best doping efficiency, the electrical conductivity after doping was promoted to 1808 S/cm at 1% Ga doping concentration. For enhancing the absolute value of Seebeck coefficient, organic-inorganic superlattice, i.e. 4,4'-Oxydianiline(ODA)/ZnO, deposited by ALD/MLD combination achieved the best Seebeck coefficient, -220 μ V/K. However, the thick Al₂O₃ dopant layers (0.82 nm) inserted into ZnO matrix suppressed the thermal conductivity and enhanced the ZT value most effectively, the values are 0.26 W/m K and 0.14, respectively.

Table 1.1: The current progress in ALD ZnO thin film thermoelectric materials.

Dopants	Doping concentration (%)	Electrical conductivity (S/cm)	Seebeck coefficient ($\mu\text{V/K}$)	Thermal conductivity (W/m K)	ZT (300K)	Ref
Ga	1	1808	-60	N/A	N/A	⁷⁴
Al	2	107	-63	1.18	0.012	⁷⁵
Al	2	278	-66	0.26	0.14	⁷⁶
ODA/ HQ/ AP	2.5	1.6/ 3.5/ 10	-220/ -205/ -160	N/A	N/A	⁷⁷
Al & HQ	2	14.3	-200	N/A	N/A	⁷⁸



1.6 Applications of ALD/MLD superlattices

As stated in section 1.4.2, the combination of ALD and MLD techniques possesses a great control of the composition, structure of superlattice, so it is easy to fine tune the characteristics of deposited superlattice materials, such as hardness, refractive index/extinction coefficient, flexibility and conductivity. Therefore, there are plenty of researches about the application of superlattices materials deposited by ALD/MLD techniques, including Lithium-ion battery, filtration, gas separation, gas molecule capture/release and optical fiber^{79–85}. Here, we only focus on the following two applications, flexible high performance gas barrier and nanoporous materials.

1.6.1 Flexible high performance gas barrier

In recent years, flexible/stretchable electronics have drawn much attention and their potentials on a variety of applications have been demonstrated successfully, such as wearable devices, artificial skins, diagnosis and therapy of movement disorders. However, the commercialization of flexible/stretchable electronics is greatly hindered by the lack of effective encapsulation with satisfying flexibility/stretchability. To address this issue, our group have verified the feasibility of depositing superlattice-based flexible high performance gas barrier through ALD/MLD techniques. In our results, the inserted polymer, PA32 (Poly(imino-(1,3-dioxotrimethylene)-

iminoethylene)) (the structure Figure 1.15), provided the flexibility and decoupled the defects of inorganic parts, Al₂O₃ and/or HfO₂, and thus the gas-barrier performance was promoted by prolong the torturous paths of gases. The schematics of the torturous path of inorganic-organic multilayer gas barrier is presented in Figure 1.16. Under the optimal structure, the WVTR (water vapor transmission rate) was $\sim 10^{-6}$ g m⁻² day⁻¹, which meets the requirement of encapsulation of OLED, even with 10% strain. For the detailed results, they can be seen in the doctoral dissertation of Ming-Hung Tseng, Ph.D.

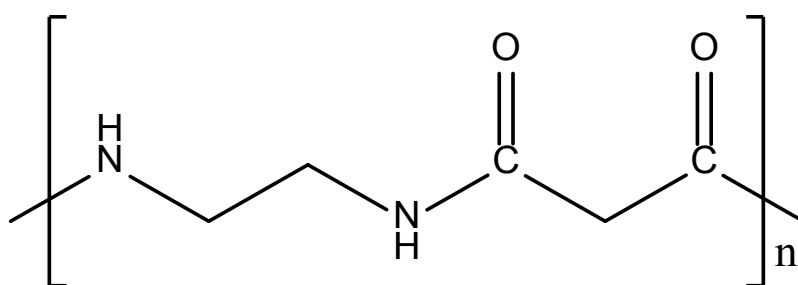


Figure 1.15: The structure of PA32.

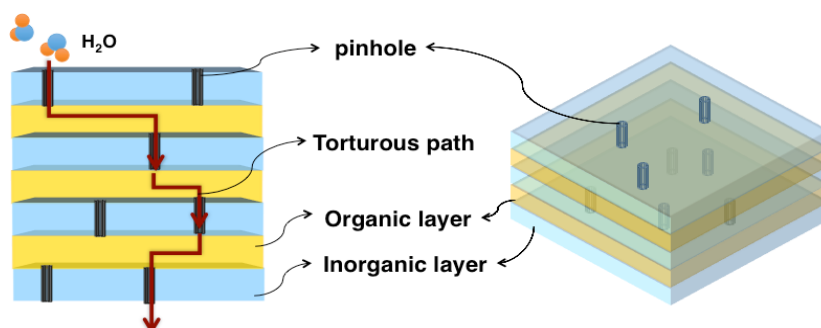


Figure 1.16: The schematics of torturous path of inorganic-organic multilayer gas barrier.

1.6.2 Nanoporous materials



In the past, the fabrication of nanoporous materials, such as zeolite and metal organic framework, required a series of chemical reactions with delicate and precision control; hence the practicality is greatly limited. Luckily, the evolution of ALD/MLD superlattice provides a novel route to fabricate nanoporous materials, whose pore size is smaller than 1 nm especially. To form nanoporous materials, the metalcone-type superlattice films, including alucone, zincone, titanicone, are post-annealed in oxygen contained atmosphere at an elevated temperature (above 400°C) to eliminate the carbon-segments, thus the nanoscale pores are obtained with varied metal oxide scaffolds based on the selected metalcone. On the other hand, the conductive-carbon contained metal oxide is obtained by annealing the deposited superlattice films in the inert atmosphere. The schematic illustration of the evolution of ALD/MLD superlattice after post-annealing in various atmosphere is shown in Figure 1.17⁷⁹. In the process of forming nanoporous materials, the pore size and porosity are determined by the thickness (chain length) and periodicity of organic segments. Therefore, these properties can be fine-tuned by selecting a proper organic precursor and designing a certain structure of superlattice. The tunability of pore size is presented in Figure 1.18 by the integrating the researches done by Liang et al^{86,87}. So far, the resulted nanoporous materials with varied pore size have been utilized in a variety of researches, e.g. the ion-conductive protection

layer of electrode in Lithium-ion battery, the molecular sieve in gas separation and filtration of organic molecules, stabilizer for enhancing Pt ORR performance and the controlled release of molecules.

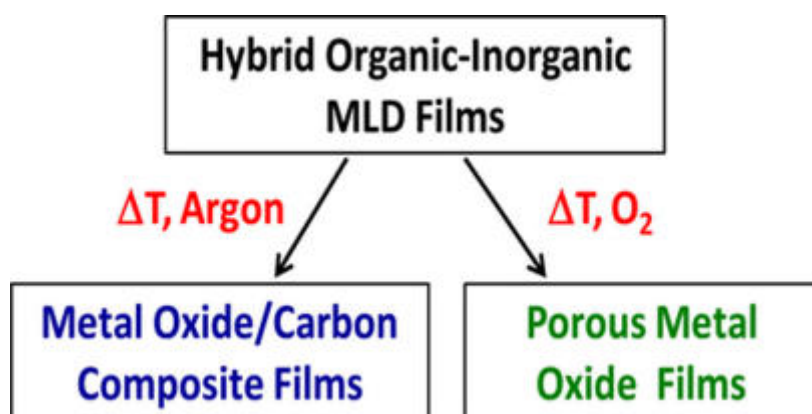


Figure 1.17: The schematic illustration of the evolution of ALD/MLD superlattice after post-annealing in various atmosphere.

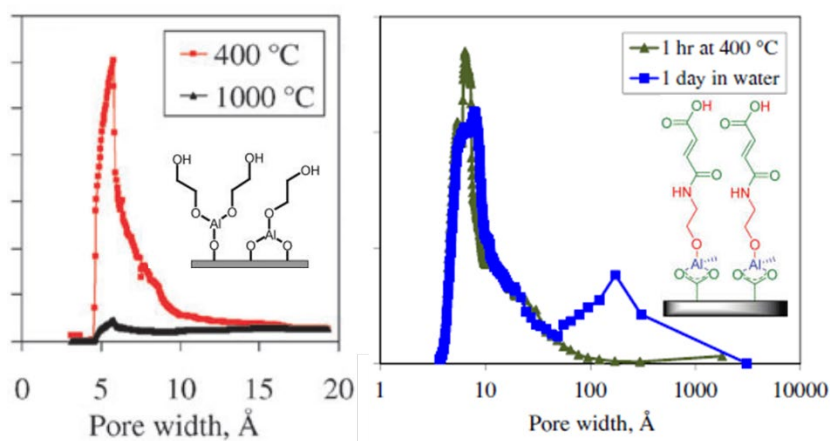


Figure 1.18: The tunability of pore size resulted from ALD/MLD superlattice.

1.7 Motivation and objective statements

As mentioned in section 1.3.3. , the demand of thin film thermoelectric materials is called for owing to the growing attention in the waste heat recycling and the cooling system in personal portable devices. Thanks to the advantages, such as the precise control over the thickness and the composition of thin films, the conformal coverage over large area substrates with high ratio surface features, ALD is the best technique to deposit the high performance thin film thermoelectric materials.


To date, the progress of ALD ZnO-based thin film thermoelectric materials has been made significantly. By fine tuning the thickness of Al dopant layers, the ZT value of has been enhanced by almost two orders of magnitude, i.e. 0.0015 to 0.14. However, from Table 1.1, we can discover that only few kinds of dopants were utilized in current researches, e.g. Al and Ga. Also, only single periodicity of superlattice was designed to reduce the thermal conductivity of materials via interface scattering in each research. Moreover, the organic insertions were limited to monolayers formed by benzene ring contained molecules which are almost insulation, so the current ALD/MLD organic-inorganic superlattices showed the terrible electrical conductivities. Hence, more detailed and fundamental researches have to be done in order to verify the feasibility and show the advantages of ALD technique in developing the high performance thin film thermoelectric materials. The researches include the type of dopants and the

formed interface, the dependence of thermal conductivity on interface period length, and development of nanoscale conducting polymers and their superlattice with inorganic materials.



As for the flexible high performance gas barrier, although the superlattice, which was composed of HfO_2 and PA32, showed an unprecedented gas barrier performance, it still suffered from the issue of the long term stability due to the hydrolysis of PA32; hence, the performance decayed with the time exposed to water. To address this issue, the development of anti-hydrolysis polymers as the substitutions for PA32 in the deposition of superlattice is crucial to improve the long term stability of superlattice. Regarding the progression of nanoporous materials, the way to eliminate organic component was post-annealing at an elevated temperature, basically above 400°C . Therefore, it is hard to use with the flexible polymer-based substrates and/or integrate with other organic-based devices since the elevated annealing temperature can also pyrolyze them. Hence, the exploration of the low-temperature pyrolysis process of metalcone superlattices can enhance the practicability of metalcone-resulted nanoporous materials.

In this dissertation, our objectives focus on the following four exploratory studies to improve the performance of superlattice thermoelectric materials, ALD/MLD gas barrier.

- 
- (1) Study of the effects of composition and structure on the thermoelectric properties of metal oxide superlattice thin films.
- (2) Study of the effects of incorporating O^{18} isotope into the metal oxide superlattice on its thermoelectric properties.
- (3) Development of novel MLD conducting polymers and their superlattice with metal oxide semiconductors.
- (4) Development of anti-hydrolysis polymers by MLD technique and the fabrication of long-term stable gas barrier composed of metal oxide and anti-hydrolysis polymers.




1.8 Research approach

1.8.1 High valence and high atomic weight metal ion doping

Typically, the doping of metal oxide is conducted by introducing guest ions (dopants) which are aliovalent to replace the cations or anions in the host materials. In ALD technique, the guest oxide layers, in which metal ions are aliovalent compared with the ones in host materials, are periodically inserted into the host metal oxide to offer dopant ions. Take Al doped ZnO (Al:ZnO) as an example, Al_2O_3 guest layers were periodically inserted into ZnO host layers by alternating one Al_2O_3 cycle with a number of ZnO cycles. In this case, since the valence of dopants, i.e. Al^{3+} , is higher than that of Zn^{2+} , the free electrons, which are able to make contributions to conducting, were created at the interface of Al_2O_3 and ZnO; hence the n-type doping was achieved. In addition to inducing free electrical carriers, the insertion of guest layers created a number of host/guest interfaces periodically which can also serve as the phonon scattering centers to reduce the thermal conductivity of Al:ZnO by increasing interfacial scattering.

As listed in Table 1.1, the current ALD researches about thermoelectric properties of doped ZnO thin films focused on the usage of boron-group metal oxides, i.e. Al_2O_3 and Ga_2O_3 , as inserted guest layers to arrive at n-type doping and reduce thermal conductivities by increasing interfacial scattering. However, based on the concept of



aliovalent doping, the usage of much higher valent metal ions as dopants is able to create more free electrons potentially. Besides, the effect of interface scattering on phonons can be enhanced by increasing the mass difference across the interface. Hence, in order to obtain these two advantages, we target on the IVB group metal ions doped ZnO to study the influence of the high valence and high atomic weight metal ion dopants on the thermoelectric properties. Because IVB group metals, i.e. titanium (Ti), zirconium (Zr) and hafnium (Hf), are tetravalent in compounds generally, they are able to donate more electrons compared to the boron group metal ions. Furthermore, Zr and Hf are much heavier than Zn, so we can systematically investigate the effect of mass difference between dopants and the host material on suppressing the thermal conductivity.

1.8.2 Isotope superlattice

In the past, the ways to modify the thermal conductivity of materials, such as morphology control, tuning element composition, crystallinity and introduction of micro/nano-structure into matrix material, influenced the electrical conductivity in the meanwhile. Typically, the damage to electrical conductivity is accompanied with reduction of thermal conductivity through above ways. Luckily, isotopically composition modifying hews out a new way to overcome the dilemma. Isotopes, the

atoms only differ in numbers of neutron, show almost the same chemical and electrical properties; thus, the incorporation of isotopes into the host materials causes nearly no influence on the electrical performance. However, the mass difference changes the vibration frequency of atoms and then affects the transport properties of phonons.


Nowadays, the researches about the effect of isotopically modification on the thermal conductivity and the thermoelectricity were almost limited to elementary substances, e.g. graphene, carbon nanotube, silicon nanowire and lithium rod⁸⁸⁻⁹¹.

Hence, the isotope effect in multi-element compound is still under investigation. In this study, we use oxygen-18, which is the heaviest stable isotope of oxygen, to deposit the isotope-containing ZnO, and then experimentally verify the effect of the concentration of isotope and the period length of superlattice on suppressing the thermal conductivity of doped ZnO while remaining the optimal electrical performance developed by aliovalent doping.

1.8.3 Novel MLD conducting polymer development and the metal oxide/polymer superlattice deposition

In tradition, conducting polymer thin films were fabricated by solution processes, such as typical chemical synthesis, spin coating and electrochemical polymerization.

However, the usage of solvents has to be considered in various applications owing to the



costs and toxicity. Besides, the solvent residue and orthogonality are also important concerns while fabricating organic based devices. Therefore, the vapor phase synthesis and deposition, which are able to overcome these problems, have drawn much attention⁹². Thanks to the promoted monomer transport on the growth surface, the conducting polymer thin films prepared by vapor processes, such as vapor phase polymerization (VPP) and oxidative chemical vapor deposition (oCVD), are more crystalline and show a higher electrical conductivity⁹²⁻⁹⁴.

Recently, Parsons et al. successfully demonstrated the deposition of poly (3, 4-ethylenedioxythiophene) (PEDOT) via oxidative molecular layer deposition technique (oMLD) using 3, 4-ethylenedioxythiophene (EDOT) as a monomer and molybdenum pentachloride (MoCl_5) as an oxidant⁹⁵. The reaction mechanism is shown in Figure 1.19. In their results, deposited PEDOT films were coated on nanostructure features (e.g. silica fiber and nanoporous ITO) with precise control of thickness, which is about 20 nm, and the highest electrical conductivity exceeded 3000 S cm^{-1} .

Nonetheless, the high condensability of MoCl_5 (mp: 194°C ; bp: 268°C) may cause the considerable variation during process. Thus, the explorations of oxidants with adequate volatility are required to build up a robust and high reproducibility MLD process. In this study, we use two novel oxidants, i.e. SbCl_5 and VOCl_3 , and then follow the similar reaction mechanism to set up versatile MLD conducting polymer deposition

process, such as polythiophene, polyaniline, and robust PEDOT process. After setting up the robust MLD conducting polymer process, we incorporate the MLD conducting polymer with the doped ZnO we developed in previous researches to deposit the metal oxide/polymer superlattices for investigating the dependence of the composition and the structure of superlattice on the thermoelectric properties.

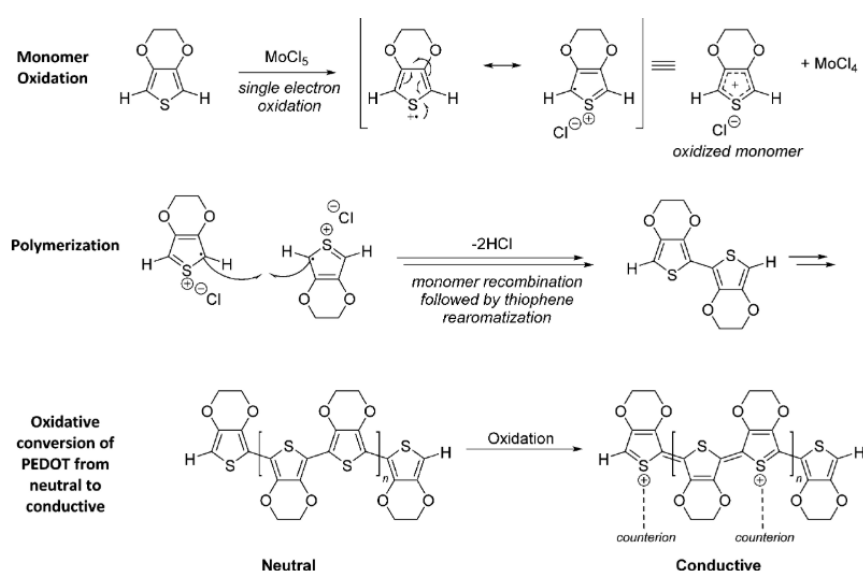


Figure 1.19: The reaction mechanism of MLD PEDOT⁹⁵.

1.8.4 Anti-hydrolysis polymer development

In our previous work, the polymer we utilized in the deposition of superlattice, PA32, suffered from the serious hydrolysis under humid conditions due to the following reasons. One is that the polymer was easily decomposed into oligomers with amine and/or carboxylic acid groups due to the high hydrolysis rate constant of amide bonds on PA32. The other is that the main chain of PA32 was composed of short aliphatic

components, which are non-hydrophobic. Therefore, water molecules are able to absorb onto the polymer chain easily and then induce the hydrolysis reaction of deposited polymers. For these two reasons, the gas barrier performance of HfO₂/PA32 superlattice decayed with time.

To address this issue, two approaches are proposed in this dissertation. The first one is to develop the deposition of polymers with a relatively low hydrolysis reaction rate constant. For convenience, we choose a versatile and commonly used polymer, polyester, to verify the concept in our proposal. In this study, we control the structure of main chain while substituting the functional group only. The second approach is maintaining the functional group but modifying the main chain of PA32, such as the introduction of aromatic component and/or long alkyl chains, to enhance the hydrophobicity of polyamide and prevent the occurrence of hydrolysis reaction. It is noteworthy that the deposition temperature is set at 100~130°C, at which the gas barrier performance of inorganic part, HfO₂, was excellent. After the development of anti-hydrolysis polymers, the superlattice gas barriers, which are made up of the alternating of anti-hydrolysis polymers and HfO₂, are deposited to verify the effect of anti-hydrolysis polymers on the long-term stability of high performance gas barrier.

1.9 Dissertation Organization



The content in each chapter is summarized below:

In chapter 1, we introduce the fundamental of thermoelectric effect, the thermoelectric in thin films, the basic of ALD and its progress on thermoelectricity; besides, we also introduce the other applications of ALD-deposited superlattices. Next, we state our research motivation and objectives and show the research approaches we used in this dissertation.

In chapter 2, we state the experimental details in this dissertation, e.g. processing equipment and parameters, and the measurement and analysis techniques.

In chapter 3, we focus on enhancing the thermoelectric performance of ZnO by doping ZnO with dopants and forming ZnO inorganic superlattices. In this study, the following topics are systematically investigated, including the selection of dopants, the distribution patterns of doping layer, and the incorporation of isotopes.

In chapter 4, we seek to further enhance the thermoelectric performance of the doped ZnO by the incorporation of conducting polymers to form the metal oxide/polymer superlattice. Hence, the properties of novel MLD-deposited conducting polymers we develop are stated first. Next, the essential of interface-engineering at doped ZnO/polymer interfaces during depositing metal oxide/polymer superlattice is discussed. Finally, the structure of doped ZnO/polymer superlattice, such as periodicity

and thickness of each layer, i optimized to achieve the best thermoelectric performance.

In chapter 5, we state the progress of developing anti-hydrolysis polymers by MLD technique first, in which includes the deposition of polyester, hydrophobic polyamide; besides, the performance of gas barrier with anti-hydrolysis polymer is presented also.

In chapter 6, the conclusion of the dissertation is stated.

Chapter 2

Experimental methods



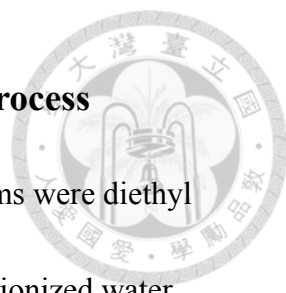
2.1 Equipment and experiment details

2.1.1 ALD and MLD deposition systems

In this study, a commercial ALD system (Cambridge NanoTech Savannah 100) was utilized to deposit metal ion doped ZnO and isotope incorporated ZnO thin films. For MLD conducting polymer thin films and metal oxide/polymer superlattice, they were deposited by a home-made system with similar configuration to Savannah 100. For ALD system and MLD system, the chamber pressures were kept around 0.1 Torr and 0.3 Torr, respectively, with both constant 20 sccm high-purity N₂ gas flow throughout process. Precursors were introduced and purged with the assistance of N₂ flow gas.

As for the sample preparations, alkali-free glass and silicon wafer were utilized as substrates. The substrates were ultrasonically cleaned for 10 minutes in each of the following baths in order: acetone, methanol, isopropanol and deionized water. Before ALD or MLD deposition process, substrates are dried by N₂ blow and then were treated with an oxygen plasma treatment in a plasma cleaner (Harrick Scientific, Model PDC-32G, USA) for 5 minutes to remove residual surface contamination and increase surface hydroxyl groups for ALD nucleation.

2.1.2 Conventional and mixed ALD metal ion doping process



In this study, the precursors we utilized to deposit ZnO thin films were diethyl zinc (DEZn, purchased from Sigma-Aldrich with 97% purity) and deionized water (H₂O). About metal ion dopants, for controlling the reactivity of precursor, we used the organometallic compounds with same functional groups as precursors, i.e. tetrakis(dimethylamido)titanium (TDMATi, purchased from Sigma-Aldrich with $\geq 99.99\%$ purity), tetrakis(dimethylamido)zirconium (TDMAZr, purchased from Sigma-Aldrich with $\geq 99.99\%$ purity) and tetrakis(dimethylamido)hafnium (TDMAHf, purchased from Sigma-Aldrich with $\geq 99.99\%$ purity) were the source of Ti, Zr and Hf, respectively. Also, all the organometallic compound precursors were used as received. During deposition processes, DEZn and deionized water were kept at room temperature; however, TDMATi, TDMAZr and TDMAHf were heated to 75°C for acquiring sufficient vapor pressure. Besides, the deposition temperature was set at 150°C, which is a normal ALD ZnO process temperature. The ALD cycle settings including precursor pulse time, precursor soaking time and N₂ purge time are listed in Table 2.1, Table 2.2 and Table 2.3. All the samples were composed of around 500 cycles of deposition. As for the nomenclature, doped ZnO with 49 cycles of ZnO and 1 cycle of conventional process HfO₂ layer is called as con 49:1 Hf:ZnO. In contrast, the one with 24 cycles of ZnO and 1 cycle of mixed ALD doping process is called as mix 24:1 Hf:ZnO.

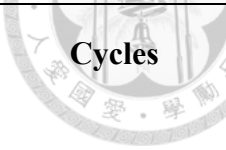
Table 2.1: ALD parameters of depositing undoped ZnO.

	Precursors	Pulse time(s)	Soaking time(s)	Purge time(s)	Cycles
Nucleation layer	DEZn	0.1	25	25	5
	H ₂ O	0.1	25	25	
ZnO	DEZn	0.05	0	5	500
	H ₂ O	0.03	0	5	

Table 2.2: ALD parameters of depositing conventional process metal ion doped ZnO.

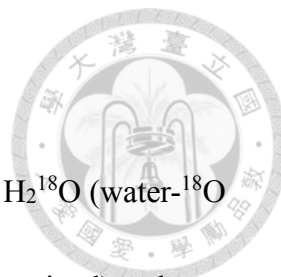
	Precursors	Pulse time(s)	Soaking time(s)	Purge time(s)	Cycles	
Nucleation layer	DeEZn	0.1	25	25	5	
	H ₂ O	0.1	25	25		
Conventional process	DEZn	0.05	0	5	n	m(n+1)~500
	H ₂ O	0.03	0	5		
	TDMATi /TDMAZr /TDMAHf	0.1	0	8	1	
	H ₂ O	0.03	0	5		

Table 2.3: ALD parameters of depositing mixed ALD doping process metal ion doped ZnO.


	Precursors	Pulse time(s)	Soaking time(s)	Purge time(s)	 Cycles	
Nucleation layer	DEZn	0.1	25	25	5	
	H ₂ O	0.1	25	25		
Mixed ALD doping process	DEZn	0.05	0	5	n	m(n+1)~500
	H ₂ O	0.03	0	5		
	DEZn+ TDMATi /TDMAZr /TDMAHf	0.05+0.1	0	15	1	
	H ₂ O	0.03	0	5		

2.1.3 Oxygen isotope incorporated superlattice

For the deposition of oxygen isotope incorporated superlattice, H_2^{18}O (water- ^{18}O with 97 atom% ^{18}O was purchased from Sigma-Aldrich and used as received) and was utilized as the source of oxygen isotope. As same as the normal H_2O , H_2^{18}O is still ease to volatilize at room temperature, so the pulse time of H_2^{18}O was set at 0.03s, which was close to the lower limit pulse time of our system for all process. However, prolonged purge time was required to remove excess physisorbed H_2^{18}O molecules owing to slightly low vapor pressure compared to normal H_2O . For convenience, we prolonged the purge time from 5s to 8s arbitrarily.



2.1.4 MLD conducting polymer process



About development of novel MLD conducting polymers, the oxidants we selected were vanadium oxychloride (VOCl_3) (mp: -77°C ; bp: 126°C) and antimony chloride (SbCl_5) (mp: 2.8°C ; bp: 90°C), which are both much more volatile than molybdenum pentachloride (MoCl_5) (mp: 194°C ; bp: 268°C). As for monomers, we used thiophene, aniline and 3, 4-ethylenedioxythiophene (EDOT) to deposit polythiophene, polyaniline and PEDOT, respectively. All the precursors were used as received and purchased from Sigma-Aldrich with $\geq 99\%$ purity except for EDOT whose purity was 97%. The temperature of each precursor and the setting parameters for depositing polythiophene, polyaniline and PEDOT are summarized in Table 2.4, Table 2.5 and Table 2.6, respectively. With regard to the deposition temperature, the chamber temperature was set at 150°C to match up the ALD doped ZnO deposition process for developing metal oxide/polymer superlattice.

Table 2.4: MLD parameters of depositing polythiophene.

Precursor	Temperature (°C)	Pulse time (s)	Soaking time (s)	Purge time (s)
VOCl ₃	RT	0.1	3/5	8
thiophene	RT	0.1	3/5	8

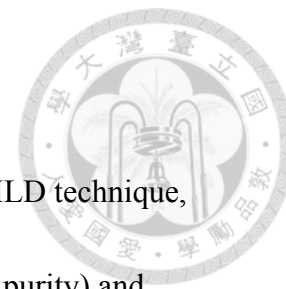
Table 2.5: MLD parameters of depositing polyaniline.

	Precursor	Temperature (°C)	Pulse time (s)	Soaking time (s)	Purge time (s)
VOCl ₃ system	VOCl ₃	RT	0.1	3/5	8
	Aniline	55/65	0.1	3/5	13
SbCl ₅ system	SbCl ₅	75/85/95	0.1	5	13
	Aniline	65	0.1	5	13

Table 2.6: MLD parameters of depositing PEDOT.

Precursor	Temperature (°C)	Pulse time (s)	Soaking time (s)	Purge time (s)
SbCl ₅	75	0.1	10	20
EDOT	80	0.1	10	20

2.1.5 Anti-hydrolysis polymers and metalcone process



In the development of anti-hydrolysis polymers deposited by MLD technique, malonyl chloride (MC, purchased from Sigma-Aldrich with $\geq 97\%$ purity) and ethylene glycol anhydrous (EG, $\geq 99.8\%$ purity) were utilized as the monomers to deposit polyester thin films. The detailed deposition parameters of polyester are listed in Table 2.7. As for the deposition of polyamide thin films, three combinations were tried: malonyl chloride and piperazine ($\geq 99\%$ purity); malonyl chloride and 1,8-diaminooctane ($\geq 98\%$ purity); terephthaloyl chloride (TC, $\geq 99\%$ purity) and ethylenediamine (ED, $\geq 99\%$ purity). The detailed deposition parameters of polyamide are presented in Table 2.8. Regarding the deposition of metalcone films (alucone we deposited only), the precursors were trimethylaluminum (TMA, with $\geq 99.99\%$ purity) and EG. The detailed parameters are summarized in Table 2.9. It is noteworthy that all precursors were purchased from Sigma-Aldrich and utilized as received.

Table 2.7 MLD parameters of depositing polyester.

Precursor	Temperature (°C)	Pulse time (s)	Soaking time (s)	Purge time (s)
MC	RT	0.5	0	25
EG	100	0.02~0.15	0/5	90

Table 2.8: MLD parameters of depositing polyamides.


	Precursor	Temperature (°C)	Pulse time (s)	Soaking time (s)	Purge time (s)
Type	MC	RT	0.5	0	25
1	piperazine	85	0.5	0	90
Type	MC	RT	0.5	0	240
2	1,8-diaminooctane	90	0.03	0	300
Type	TC	120	0.5	0	120
3	ED	RT	0.25	0	90

Table 2.9: MLD parameters of depositing alucone at 105°C.

Precursor	Temperature (°C)	Pulse time (s)	Soaking time (s)	Purge time (s)
TMA	RT	0.02	0	30
EG	100	0.02	0/5/15	90

2.2 Thin film characteristics analysis

2.2.1 Measurements of electrical conductivity and Seebeck coefficient



The electrical conductivity, carrier concentration and carrier mobility of the deposited films were determined by Hall effect system (ECOPIA HMS-3000, USA). The design of system is based on Van der Pauw four-point probes method. As for Seebeck coefficient, a home-made system was set up to conduct the measurement. The scheme illustration of home-made system is shown in Figure 2.1. The system was composed of a thermoelectric heating apparatus with a controllable power supply PROVA8000 (TES, Taiwan) to adjust output power and create consistent temperature gradient, and two type-T thermocouples which were connected to the data acquisition switch unit (Keysight 34970A, USA) to measure the temperature at the two ends of the sample. Also, the copper wires of the thermocouples were utilized to measure the electrical voltage between two ends by the data acquisition switch unit. The measurement of Hall effect and Seebeck coefficient were conducted four times (i.e. four sides or four corners) and then were averaged.

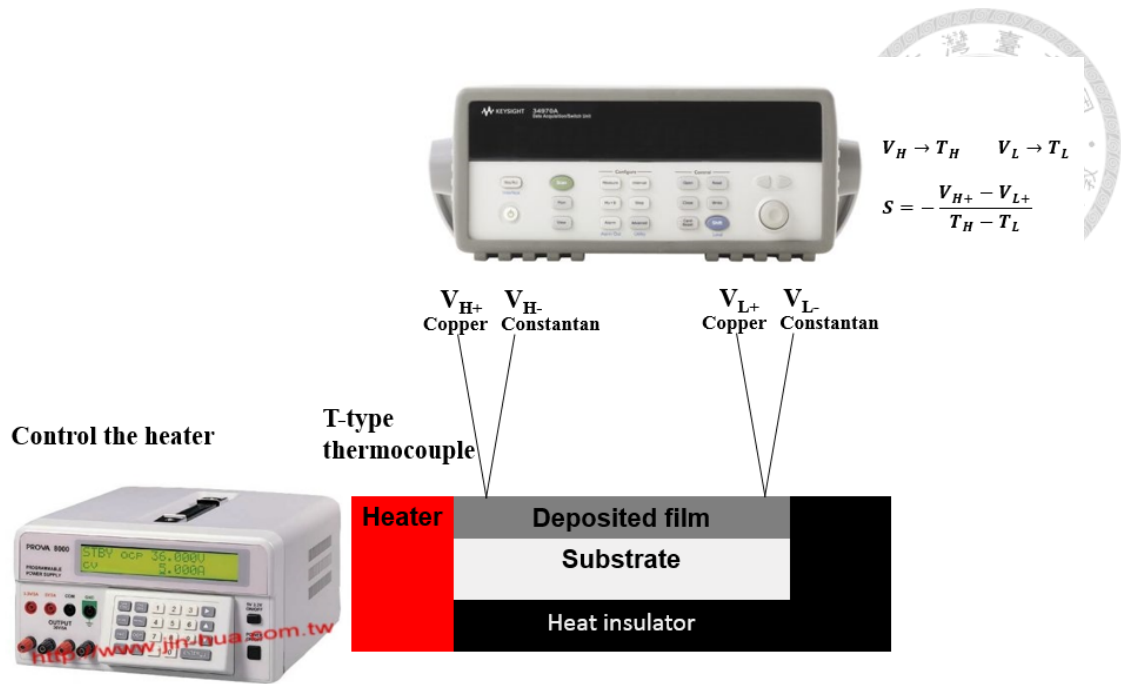



Figure 2.1: The scheme illustration of home-made system for measuring Seebeck coefficient.

2.2.2 Measurement of thermal conductivity by the time-domain thermoreflectance method (TDTR)

Time-domain thermoreflectance (TDTR) is an ultrafast optical pump-probe technique. This method is conducted by using the output of a femtosecond, mode-locked Ti:sapphire laser to heat the metal transducer film which is coated onto the under-test material and probe the temperature evolution by measuring temperature-dependence reflectance (thermoreflectance) of metal transducer film. Typically, the Al film with ~80nm thickness is selected as metal transducer film owing to its great thermoreflectance response at the wavelength of Ti:sapphire laser (~785nm). In this

study, the coated Al films are deposited by thermal evaporation.



In measurements, the output of the Ti:sapphire laser is split into two beams, pump beam and probe beam. The pump beam is modulated at 8.7 MHz by an electro-optical modulator and the probe beam is mechanically chopped at around 200 Hz. Both beams are focused on the Al film by an objective lens. The probe beam heats up the Al transducer film and then the temperature change of Al films is detected as a function by probe beam. Next, a Si photodiode and a radio-frequency lock-in amplifier are utilized to measure the intensity variant of reflected probe beam caused by temperature-dependence reflectance of Al film. The output signal $V(t)$ is composed of two parts, the in-phase component $V_{in}(t)$ and the out-of-phase component $V_{out}(t)$, and can be described as $V(t) = V_{in}(t) + iV_{out}(t)$, where t is the delay time between two beams. The thermal conductivity of materials can be determined by compared the measured ratio $V_{in}(t)/V_{out}(t)$ to the calculations from simulation of thermal transport in samples. The multilayered structure used for simulation is shown in Figure 2.2 and one of the determined thermal conductivity by matching the measured ratio and simulation is shown in Figure 2.3. This set of measuring apparatus is supported by The Extreme Conditions Laboratory at IES, Academia Sinica and the schematic layout can be seen in Figure 2.4. The detailed description of thermal model used in simulation can be seen in Ref⁹⁶.

In order to evaluate the uncertainty of obtained thermal conductivity, the sensitivity parameters of each term utilized in simulation are calculated. The sensitivity parameter is defined as: $S_{\alpha} = \frac{\partial \ln(-V_{in}/V_{out})}{\partial \ln \alpha}$, where V_{in}/V_{out} is the ratio of measured in-phase and out-of-phase voltages. α is one of parameters utilized in simulation, such as thickness of Al, interface thermal conductance between Al film and under-test material and thermal conductivity of under-test material. Figure 2.5 shows the calculated S_{α} for each parameters in simulation. Theoretically, the ratio V_{in}/V_{out} is more sensitive to the thermal conductivity of under-test material at $100 \text{ ps} \leq t \leq 500 \text{ ps}$. Therefore, the influential parameters in our simulation are the thickness and heat capacity of Al film, thickness of ALD deposited material and the interface thermal conductance between ALD deposited material with Al film and Si substrate. Assuming 3% uncertainties of these influential parameters, the total error in simulated thermal conductivity of ALD deposited material is ~7%.

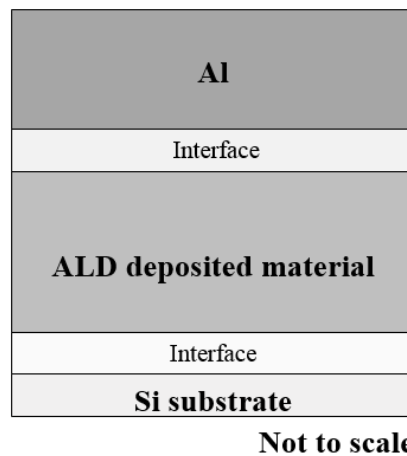


Figure 2.2: The multilayered structure used for simulation.

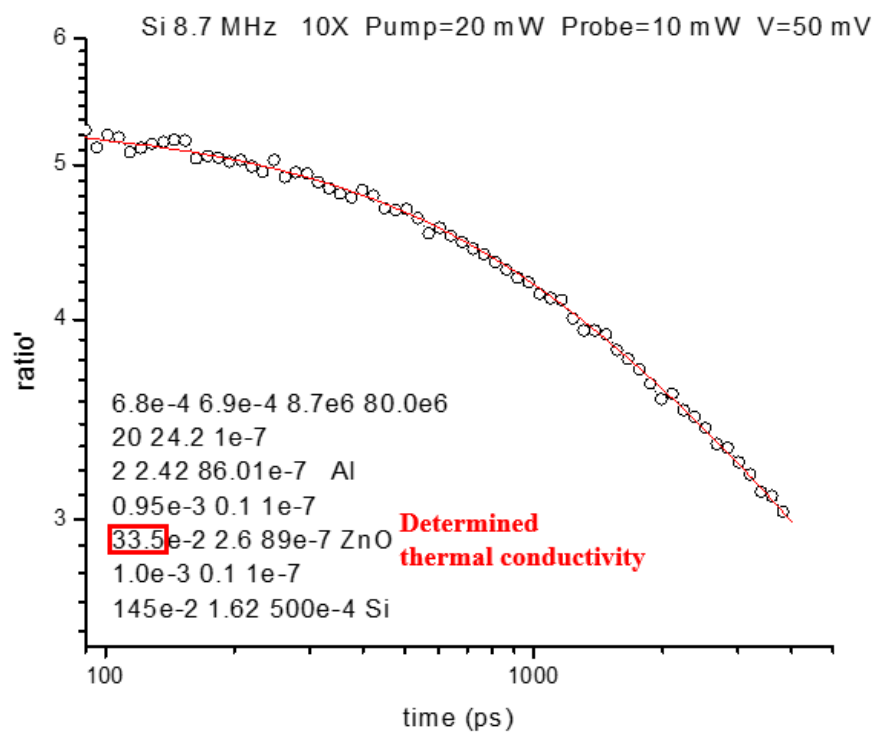


Figure 2.3: The result of ZnO thermal conductivity by TDTR method.

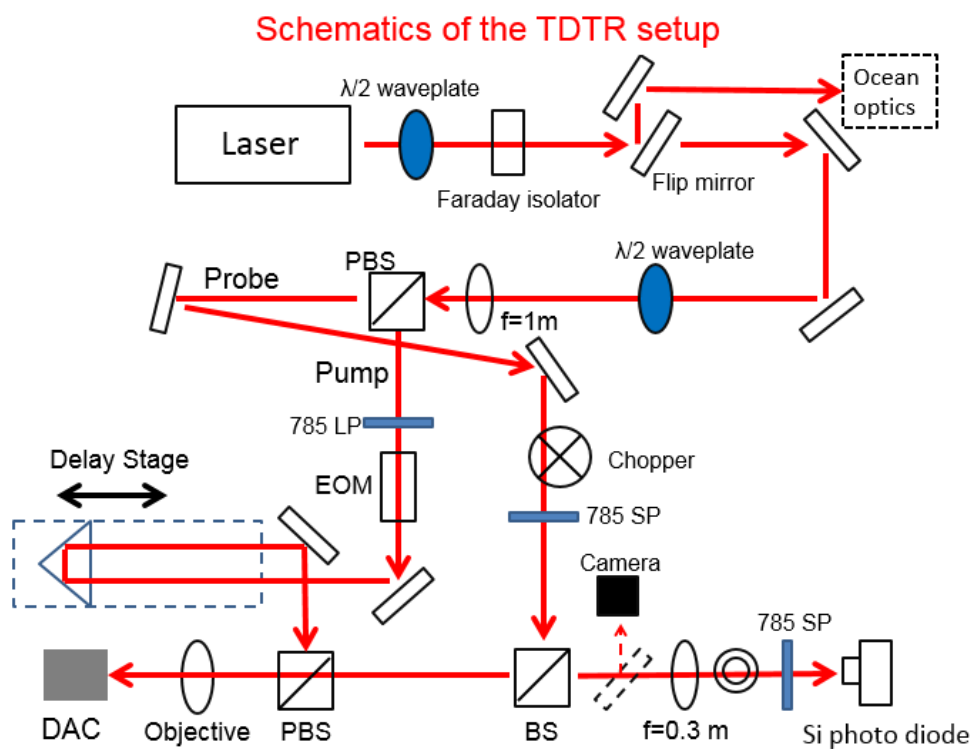


Figure 2.4: The schematic layout of TDTR apparatus.

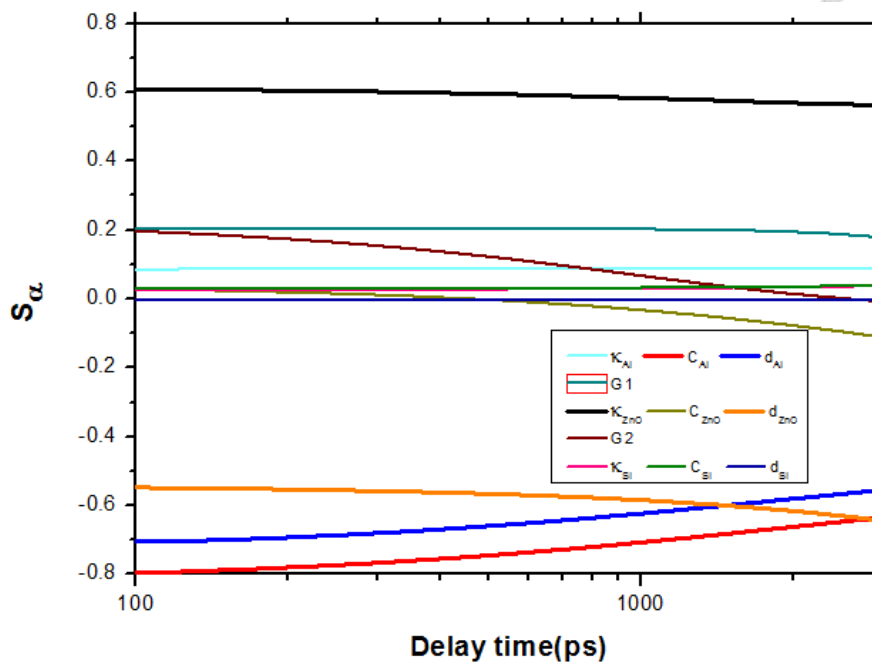



Figure 2.5: The calculated S_{α} for each parameters in simulation.

2.2.3 Quartz crystal microbalance (QCM)

To monitor the surface reaction of precursors (e.g. adsorption and desorption) during process in real time, ALD and MLD deposition systems are equipped with customized in-situ QCM system. The QCM signals were recorded and analyzed by STM-2 (INFICON, Switzerland).

2.2.4 Spectral characterization

As for the thickness and refractive index measurement of the inorganic ALD films, they were determined by ellipsometry (Elli-SE-U, Ellipso Technology, Korea). In order to compare the doping concentrations between conventional process and mixed



ALD doping process, determining the composition of the deposited films was conducted with X-ray photoelectron spectroscopy (XPS) by PHI 5000 VersaProbe (ULVAC-PHI, Japan) using an Al K α X-ray source. Before depth profile XPS measurement, Ar⁺ sputtering pre-treatment was applied to remove surface contamination. The element concentrations were determined by averaging the depth-profiling results. For crystallinity and crystal structure, X-ray diffraction (XRD) patterns were collected by Rigaku TTRAX3 X-ray diffractometer (Rigaku, Japan) with Cu K α radiation. The characteristic IR absorption peaks and the UV-Vis absorption of deposited polymer films were collected by Perkinelmer spectrum 100 FT-IR operated in transmission mode at 4 cm⁻¹ resolution and Jasco V-770 UV-Visible/NIR spectrophotometer with wavelength in the range of 200-1300 nm, respectively.

2.2.5 Transmission electron microscopy (TEM)

To clearly observe the microstructure of superlattices along the direction of film growth, the cross-sectional TEM images were obtained by the field emission TEM, JEOL 2010F system (JEOL, Japan). The preparation of the cross-sectional TEM samples were implemented by Gatan Precision Ion Polishing System II, 695.B (Gatan, USA).



2.2.6 Micro-figure measurement (Alpha-step)

As for determining the thickness of MLD conducting polymer thin films, it is hard to conduct by ellipsometry since the refractive indexes of deposited materials are uncertain, which arises the uncertainty of the measured thickness. For this reason, micro-figure measurement (MICROFIGURE MEASURING INSTRUMENT-Surfcorder ET3000) was utilized to determine the thickness of deposited films. Before measurement, we removed parts of the deposited films either physically or chemically depending on the characteristic of the films. Hence, a sharp step was created and then the height of the step, i.e. film thickness, was able to be measured.

2.2.7 Gas barrier performance measurements

In this dissertation, two types of measurements, water vapor transmission rate (WVTR) and helium transmission rate (HeTR), were implemented. In the measurement of WVTR, the gas barrier was deposited on a PI substrate (thickness=75 μm) and then the WVTR was measured by MOCON AQUATRAN Model 1 at 38°C and 100% RH. As for the HeTR of the ALD/MLD deposited gas barrier with PI substrate, it was measured by a home-made setup developed by our group with the helium leak detector (Alcatel, ASM, 142Graph) as the helium sensor. For the detailed description of home-made setup, it can be found in the doctoral dissertation of Ming-Hung Tseng, Ph.D.

2.2.8 Thermogravimetric analysis (TGA)

To evaluate effect of low-temperature pyrolysis process we developed, thermogravimetric analysis (TGA) was utilized to measure the weight of carbon-residue inside the ALD/MLD deposited superlattice. In this measurement, it was conducted by TA Instruments SDT-Q600 with a 100 sccm (standard cubic centimeter per minute) O₂ flow.



Chapter 3

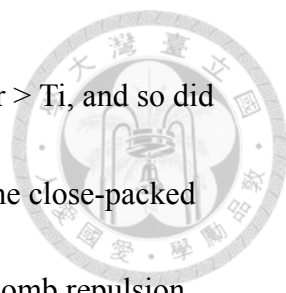
Metal oxide superlattice



3.1 Selection of dopants

For verifying the effects of Ti, Zr and Hf doping on thermoelectric properties of ZnO, we deposited four types of doped ZnO films by conventional process, i.e. con 49:1, con 24:1, con 19:1 and con 9:1 for each dopant, and the characteristics of them are summarized in Table 3.1.

Starting with the carrier concentration, it is noteworthy that the carrier concentration in Ti:ZnO system was higher than those in the other two systems. This phenomenon could be originated from the actual dopant concentration and the distance between ionized dopants. The elemental composition measured by XPS and calculated atomic number density are listed in Table 3.2. Although we chose the precursors with the same functional groups for Ti, Zr and Hf, the reactivity of these precursors were still different owing to the formation energy difference of chemisorbed precursors. Because the formation of a chemisorbed precursor involved breaking a metal/ligand bond within precursor itself and then forming a metal/oxygen bond between precursor and surface hydroxyl group. Therefore, the reactivity of a precursor might be described by the difference between the bond energies (ΔBE) of metal/ligand and metal/oxygen. The bond energy of each bond is shown in Table 3.3. It could be discovered that the actual



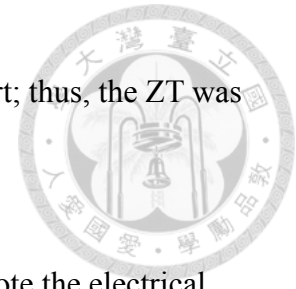
dopant concentration indeed followed the trend of ΔBE , i.e. $Hf > Zr > Ti$, and so did the number density of each dopant. Based on effective field theory, the close-packed dopants are not able to donate free electrons freely owing to the Coulomb repulsion force between adjacent ionized dopants^{68,97,98}; thus, Ti:ZnO system had a higher doping efficiency. As for the decreasing electrical mobility for all structures, it was attributed to dopant scattering effect and the suppression of crystallinity. The XRD patterns of undoped ZnO and all con 9:1 doped ZnO are shown in Figure 3.1. The reduction of intensity for all peaks implies the suppression of crystallinity with the incorporation of dopants. Especially, (002) peak, which is parallel to direction of film growth and periodicity of dopants, decreases obviously and shifts to higher angle due to lattice shrinkage in z-axis caused by the smaller ionic radius of dopants compared to Zn, which are 56 pm, 73 pm, 72 pm and 74 pm for Ti, Zr, Hf and Zn, respectively. With great radius difference, the degree of change in the diffraction pattern for Ti:ZnO was most severe, so the electrical mobility reduced seriously as well. For the overall influence on electrical conductivity, it could be found that the electrical conductivity rose as the dopant concentration increased except for con 9:1 structure. Also, this result could be explained by effective field theory. Therefore, the carrier concentration only rose slightly even decrease when the concentration of dopant rose beyond a certain level, such as con 9:1 Ti:ZnO.

In the case of Seebeck coefficients, they basically followed Mott formula, which states the trade-off characteristic of the absolute value of Seebeck coefficient and electrical conductivity. Furthermore, it could be discovered that the Seebeck coefficient was less sensitive to the electrical mobility than the carrier concentration by comparing con 24:1 Zr:ZnO with con 19:1 Hf:ZnO and con 9:1 Ti:ZnO and con 9:1 Hf:ZnO.

Overall, the highest PF value occurred at con 49:1 structure in these three systems, which was only slightly doped, the carrier concentration was around 10×10^{19} and the electrical mobility was maintained as high as possible.

Referring to thermal conductivity, we initially assumed that Hf:ZnO might has a lower thermal conductivity attributed to the large mass difference. However, this hypothesis only held for Zr:ZnO and Hf:ZnO. With the almost same ionic radius, the effect of dopants on crystallinity was almost about the same; thus, the mass difference played a crucial factor in suppressing thermal conductivity. Thus, the thermal conductivity of Hf:ZnO was lower than Zr:ZnO regardless of doping concentrations. As for Ti:ZnO, the effect of reducing crystallinity overwhelmed the influence of mass difference, so the thermal conductivity of Ti:ZnO showed a lower value when doping concentration rose. Especially, con 9:1 Ti:ZnO had the lowest thermal conductivity even the concentration of dopant was lower than Zr:ZnO and Hf:ZnO. For the overall enhancement on ZT, although the degree of reduction for thermal conductivity was

almost 15-fold, the decreasing PF compensated the outstanding effort; thus, the ZT was only enhanced by the factor of 6.44 in con 9:1 Ti:ZnO.



In summary, these three tetravalent dopants were able to promote the electrical conductivity of ZnO by the factor of around 2.5 and suppress thermal conductivity by the factor of near 15, but the decreasing absolute value of Seebeck coefficient retarded the further enhancement in ZT, which was just about 6-fold enhancement. Although the degree of enhancement in ZT was about the same in these three system, we could still conclude that Hf might be the best dopant among them. Because the incorporation of Hf didn't decrease the electrical mobility severely. This advantage ensured high electrical conductivity without increasing carrier concentration greatly, and thus the high absolute value of Seebeck coefficient could be held. Besides, the great mass difference suppressed the thermal conductivity effectively.

Table 3.1: The thermoelectric characteristic of undoped ZnO, Ti:ZnO, Zr:ZnO and Hf:ZnO. n: carrier concentration and the unit is $\times 10^{19} \text{ cm}^{-3}$; μ : electrical mobility and the unit is $\text{cm}^2 \text{ V}^{-1} \text{ s}^{-1}$; σ : electrical conductivity, S cm^{-1} ; κ : thermal conductivity, $\text{W m}^{-1} \text{ K}^{-1}$; the unit of Seebeck coefficient is $\mu\text{V K}^{-1}$; PF is the power factor and the unit is $\times 10^{-4} \text{ W m}^{-1} \text{ K}^{-2}$.

	n	μ	σ	Seebeck	PF	κ	ZT (300k)	Normalized ZT
ZnO	4.78	18.36	140.6	-107.49 \pm 1.29	1.62	33.5 \pm 0.41	0.0015	1.00
Con 49:1	12.77	13.01	265.8	-71.02 \pm 1.33	1.34	7.15 \pm 0.05	0.0056	3.87
Ti								
Con 24:1	19.02	9.13	277.9	-62.75 \pm 0.78	1.09	4.60 \pm 0.10	0.0071	4.91
Con 19:1	27.22	7.07	308.3	-55.11 \pm 1.30	0.94	3.70 \pm 0.20	0.0076	5.22
Con 9:1	23.55	5.23	197.5	-57.91 \pm 0.90	0.66	2.12 \pm 0.01	0.0093	6.44
Zr								
Con 49:1	10.36	18.18	301.6	-71.79 \pm 0.52	1.55	6.80 \pm 0.05	0.0068	4.71
Con 24:1	15.41	13.25	327.1	-60.03 \pm 0.89	1.18	4.70 \pm 0.05	0.0075	5.17
Con 19:1	16.97	11.79	318.1	-54.65 \pm 1.51	0.95	4.15 \pm 0.01	0.0070	4.72
Con 9:1	17.46	6.19	173.1	-64.36 \pm 1.14	0.72	2.30 \pm 0.01	0.0094	6.43
Hf								
Con 49:1	9.42	17.90	270.2	-74.25 \pm 0.89	1.49	6.20 \pm 0.01	0.0072	4.95
Con 24:1	14.55	13.70	319.4	-59.82 \pm 0.34	1.14	4.05 \pm 0.05	0.0084	5.82
Con 19:1	15.44	11.12	275.1	-60.79 \pm 1.32	1.02	3.50 \pm 0.05	0.0087	5.99
Con 9:1	17.03	5.68	155.1	-61.42 \pm 0.82	0.59	2.13 \pm 0.12	0.0083	5.66

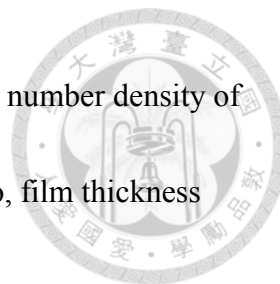


Table 3.2: The concentration of dopant measured by XPS and atomic number density of dopants. The number density is calculated by using composition ratio, film thickness and density^{41,99}.

	O:Zn:dopant	Number density of dopant (nm⁻²)
Con 9:1 Ti:ZnO	40.33 : 56.57 : 3.30	3.51
Con 9:1 Zr:ZnO	41.14 : 55.29 : 3.57	4.52
Con 9:1 Hf:ZnO	41.75 : 54.46 : 3.79	4.82

Table 3.3: Bond energy of metal/ligand and metal/oxygen and the difference between bond energies ($\Delta BE = BE \text{ metal/oxygen} - BE \text{ metal/ligand}$).

Bond energy of metal/ligand (kJ/mol)		Bond energy of metal/oxygen (kJ/mol)		ΔBE (kJ/mol)
Ti-N	-476	Ti-O	-666	-190
Zr-N	-565	Zr-O	-766	-201
Hf-N	-535	Hf-O	-801	-266

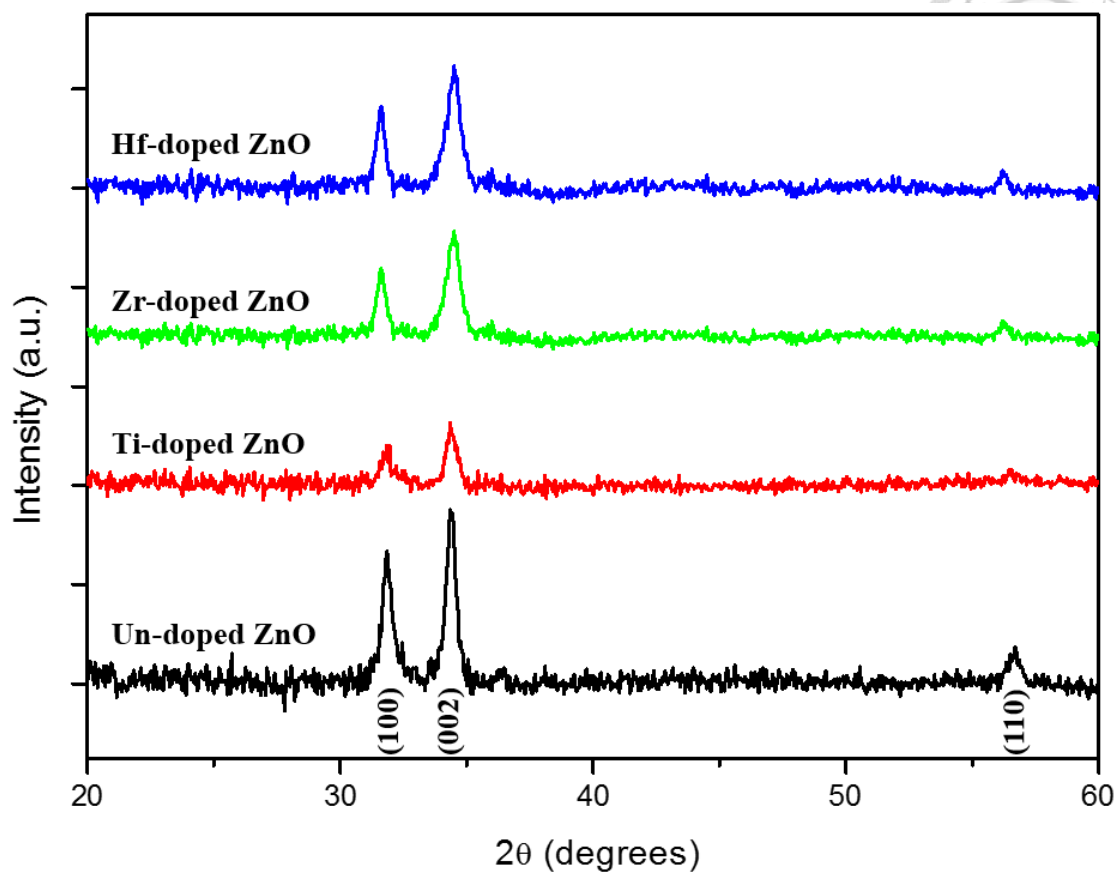


Figure 3.1: The XRD patterns of undoped ZnO and all con 9:1 doped ZnO.




3.2 Distribution Patterns of dopants

3.2.1 Conventional versus mixed ALD doping processes

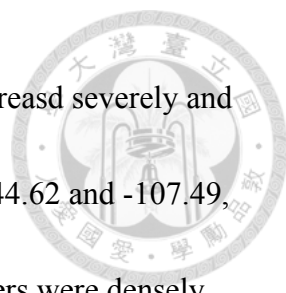
Previous section disclosed that a close-packed dopant distribution was unfavorable to enhance the electrical conductivity, so we developed a new ALD doping process, i.e. mixed ALD doping process. In the mixed ALD doping process, the dopant precursor, TDMAHf, was introduced into reaction chamber along with DEZn simultaneously while depositing dopant layers. By this way, two precursors were going to compete with each other to react with surface hydroxyl groups, so the decrement of Hf number density in dopant layers was obtained. The schematic illustration of depositing dopant layer by conventional process and mixed ALD doping process is shown in Figure 3.2. We also deposited types of mixed ALD doping process Hf:ZnO (HZO), the thermoelectric properties of them are summarized in Table 3.4.

First, it could be discovered that the carrier concentration of HZO deposited by mixed ALD doping process was much higher than that deposited by conventional process at the same repetition rate of dopant layers. Since the actual dopant concentration was quite low in mixed ALD doping process, the number density of Hf in mixed ALD doping process was only around $0.6\sim 0.7\text{ nm}^{-2}$, which was much lower than that in conventional process, i.e. $\sim 4.80\text{ nm}^{-2}$. The dopant concentration measured by XPS and calculated number density is summarized in Table 3.5. In this situation,



dopants were much freer to donate free carriers and then became ionized ions without severe repulsion from other ionized dopants in the same dopant layer. For this reason, we could increase the carrier concentration of HZO by increasing repetition rate of dopant layer until dopants were no longer such free to donate free carrier owing to the repulsion from ionized dopants in the adjacent dopant layers, i.e. from mix 4:1 to mix 3:1. With regard to the electrical mobility, the decrement of dopants in mixed ALD doping process cut down the dopant scattering effect and reduced the suppression of crystallinity, so the electrical mobility in mixed ALD doping was higher than that in conventional process. Figure 3.3(a) shows the XRD patterns for comparing crystallinity of the same dopant layer period length deposited by two different process, i.e. con 24:1 versus mix 24:1. Nevertheless, Figure 3.3(b) reveals that densely inserted dopant layers still decreased the crystallinity in (002), especially. Besides, an abundance of free carriers raised the electron scattering, which may retard the transport of each other, so the electrical mobility decreased with carrier concentration, i.e. mix 3:1. Luckily, the overall effect of mixed ALD doping process on electrical conductivity was positive, the best value was almost doubled in comparison to conventional process, i.e. mix 14:1 versus con 24:1.

Referring to Seebeck coefficient, the benefit of mixed ALD doping process on promoting doping efficiency was unfavorable to maintain the high absolute value of



Seebeck coefficient, so the absolute value of Seebeck coefficient decreased severely and the lowest value was only remain 40% compared to undoped ZnO, -44.62 and -107.49, respectively. Therefore, the PF value was quite low when dopant layers were densely inserted. Luckily, the PF value was greater than undoped ZnO when the period length of dopant layers was long, such as mix 34:1, mix 29:1 and mix 24:1. The highest PF occurred at mix 24:1 with the value of $1.90 \times 10^{-4} \text{ W m}^{-1} \text{ K}^{-2}$. Due to the low degradation to the electrical mobility in these structures, high carrier concentration was inessential for acquiring high electrical conductivity, so decrement on the absolute value of Seebeck coefficient could be suppressed. As the period length of dopant layers kept increasing, e.g. from mix 24:1 to mix 34:1, the PF value decreased and was close to the value of undoped ZnO.

Unlike its benefit to electrical performance, mixed ALD doping process showed a poor effect on reducing the thermal conductivity of ZnO. It could be seen that the degree of reducing thermal conductivity of mixed ALD doping process was much lower than that of conventional process at the same dopant layer repetition rate, i.e. ~ 2.13 for con 9:1 and ~ 8.48 for mix 9:1. As for the similar dopant concentration, e.g. mix 9:1 and con 49:1, conventional process was able to suppress thermal conductivity more effectively even densely inserted mixed ALD doping dopant layers reduced the crystallinity more severely, which can be seen in Figure 3.3(c). This result was

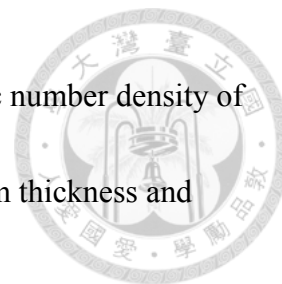
attributed to the outstanding effect of more distinct interface on phonon scattering, so the conventional process could reduce the thermal conductivity much more effectively. With regard to the overall effect on ZT, the best performance occurred at mix 3:1, whose thermal conductivity was the lowest, and the degree of enhancement was about 4-fold.

Summing up two distribution patterns of dopant, it could be realized that close-packed dopants deposited by conventional process were able to form complete heterogeneous interfaces and then had an advantage in reducing thermal conductivity. On the other hand, sparsely distributed dopants deposited by mixed ALD doping process were able to increase carrier concentration efficiently and less harmed the electrical mobility. These two characteristics ensured a high PF value, such as mix 24:1. In order to obtain the advantage of each process simultaneously for further enhancing ZT value, we were going to combine two processes and found out the best distribution pattern of the dopants.

Table 3.4: The thermoelectric characteristic of undoped ZnO, conventional process and mixed ALD doping process HZO. n: carrier concentration and the unit is $\times 10^{19} \text{ cm}^{-3}$; μ : electrical mobility and the unit is $\text{cm}^2 \text{ V}^{-1} \text{ s}^{-1}$; σ : electrical conductivity, S cm^{-1} ; κ : thermal conductivity, $\text{W m}^{-1} \text{ K}^{-1}$; the unit of Seebeck coefficient is $\mu\text{V K}^{-1}$; PF is the power factor and the unit is $\times 10^{-4} \text{ W m}^{-1} \text{ K}^{-2}$.

		n	μ	σ	Seebeck	PF	κ	ZT (300k)	Normalized ZT
ZnO		4.78	18.36	140.6	-107.49 \pm 1.29	1.62	33.5 \pm 0.41	0.0015	1.00
	49:1	9.42	17.90	270.2	-74.25 \pm 0.89	1.49	6.20 \pm 0.01	0.0072	4.95
Con	24:1	14.55	13.70	319.4	-59.82 \pm 0.34	1.14	4.05 \pm 0.05	0.0084	5.82
Hf:ZnO	19:1	15.44	11.12	275.1	-60.79 \pm 1.32	1.02	3.50 \pm 0.05	0.0087	5.99
	9:1	17.03	5.68	155.1	-61.42 \pm 0.82	0.59	2.13 \pm 0.12	0.0083	5.66
	34:1	14.79	17.92	424.6	-64.92 \pm 0.68	1.79	11.2 \pm 0.07	0.0048	3.29
	29:1	15.39	17.55	432.7	-64.72 \pm 0.84	1.81	11.0 \pm 0.16	0.0049	3.39
	24:1	16.72	17.30	463.5	-64.03 \pm 0.52	1.90	10.5 \pm 0.01	0.0054	3.73
Mix	19:1	21.63	16.06	556.4	-53.72 \pm 1.26	1.61	9.35 \pm 0.05	0.0052	3.54
Hf:ZnO	14:1	30.17	12.49	602.9	-49.11 \pm 0.67	1.45	8.60 \pm 0.02	0.0051	3.49
	9:1	33.74	10.79	583.3	-47.41 \pm 1.29	1.31	8.48 \pm 0.07	0.0046	3.19
	4:1	38.54	7.54	465.7	-45.99 \pm 0.78	0.98	4.88 \pm 0.02	0.0061	4.16
	3:1	36.20	7.29	428.6	-44.62 \pm 0.65	0.85	4.05 \pm 0.05	0.0063	4.34

Table 3.5: The concentration of dopant measured by XPS and atomic number density of Hf. The number density is calculated by using composition ratio, film thickness and density.



	O:Zn:Hf	Number density of Hf (nm⁻²)
Con 9:1	41.75 : 54.46 : 3.79	4.82
Con 24:1	45.71 : 52.87 : 1.42	4.83
Con 49:1	45.50 : 53.81 : 0.64	4.76
Mix 24:1	44.63 : 55.17 : 0.20	0.69
Mix 19:1	44.29 : 55.45 : 0.26	0.68
Mix 9:1	45.59 : 53.83 : 0.58	0.72
Mix 4:1	44.75 : 53.99 : 1.26	0.71
Mix 3:1	43.82 : 54.58 : 1.60	0.73

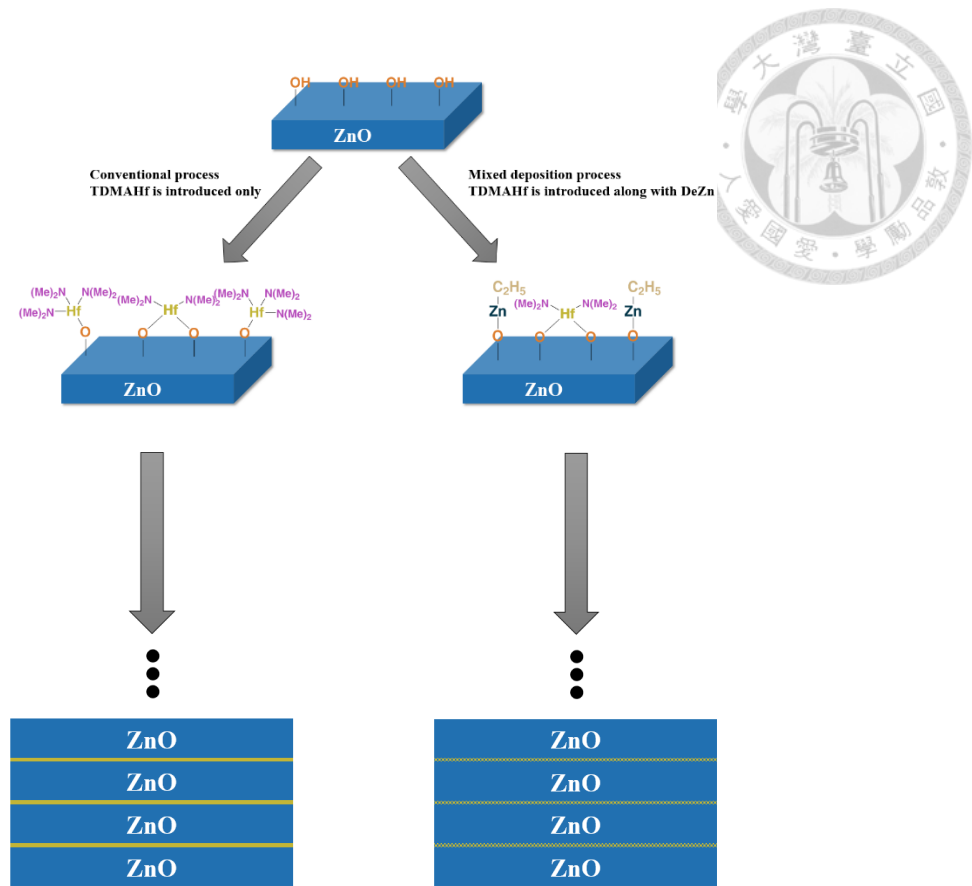


Figure 3.2: The schematic illustration of depositing dopant layer by conventional process and mixed ALD doping process.

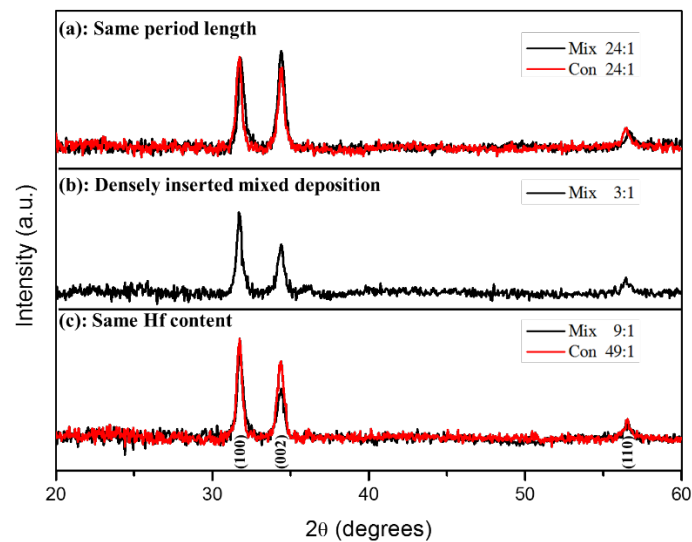


Figure 3.3: XRD comparison for (a) same period length; (b) densely inserted mixed ALD doping; (c) same Hf content.

3.2.2 Combination of conventional and mixed ALD doping processes


As mentioned before, the combination of conventional process and mixed ALD doping process was potential to obtain the advantage of each way, i.e. heat blocking of conventional process and excellent electrical performance of mixed ALD doping process. From the results of last section, it revealed that the optimal electrical performance was achieved by forming the dopant layers as a mixture of both ZnO and the HfO₂ in a periodicity of 1 mixed monolayer per 24 ZnO monolayer since mix 24:1 showed the highest PF value. Based on this contention, we were going to use mix 24:1 as a basis structure and then insert complete HfO₂ guest layers with different periodicity and thickness to enhance the suppression of thermal conductivity for mix 24:1 structure.

First, the optimal periodicity of inserted complete HfO₂ layers was studied. Table 3.6 presents the thermoelectric properties of films composed of alternating mix 24:1 host and 5-cycle conventional HfO₂ dopant layers, where the mix 24:1 host layers were of 1 period (24 ZnO cycles/1 mixed doping cycle/24 ZnO cycles), 2 periods (24/1/24/1/24), or 3 periods (24/1/24/1/24/1/24); the total number of cycles of the HZO films with the 3 mix 24:1 period lengths were 540, 553, and 520, respectively. The illustrated structures of 3 films are shown in Figure 3.4. The results confirmed that further the enhancements of ZT were indeed achievable with the combination of two processes. The addition of the 5-cycle conventional dopant layers caused only minor

reductions in power factor and other electrical properties of the mix HZO, while it lowered the thermal conductivity to ~ 3 from $\sim 10 \text{ W m}^{-1} \text{ K}^{-1}$, resulting in ~ 3 fold increase in ZT from that of mix 24:1 HZO. The optimal structure in terms of ZT was 1 period of mix 24:1 alternating with the conventional dopant layer, as the structures with 2 and 3 periods of mix 24:1 contained insufficient numbers of conventional dopant layers to effectively suppress thermal conductivity.

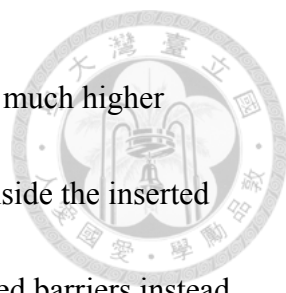
After optimizing the periodicity of the inserted HfO_2 layers, the effects of cycle of the conventional HfO_2 layers on thermoelectric performance were investigated. Figure 3.5 is the illustration of superlattices composed of 1 period of mix 24:1 HZO and varied cycles of conventional HfO_2 layer, and the thermoelectric characteristics are summarized in Table 3.7.

In order to elucidate the correlation between the deposition cycles of complete HfO_2 guest layers and the properties of mix 24 / nH, in-situ QCM was utilized to monitor the growth mechanism while switching materials. Figure 3.6(a) is the mass gain per cycle (MGPC) of HfO_2 on the surface of 24 cycles ZnO which was the deposition procedure of mix 24 / nH. Owing to the less stereo-hindrance of DEZn, the number density of surface hydroxyl groups on ZnO is much higher than that on HfO_2 , so the MGPC of HfO_2 on the ZnO surface was much higher in the initial cycles than that in the latter cycles. However, once a monolayer of HfO_2 formed, i.e. 3 cycles in our result, the



MGPC of HfO₂ decreased and approached to a constant value, which represented the steady ALD growth for HfO₂ on the surface of itself. Because TDMAHf couldn't react with the residual hydroxyl groups at the interface between ZnO and HfO₂ owing to its bulkier structure. On the other hand, Figure 3.6(b) shows the MGPC of one ZnO cycle over the surface of a ZnO film (thickness = 24 cycles) primed with 0 to 30 cycles of a HfO₂ layer. The MGPC of the ZnO cycle sharply decreased with increasing thickness of the HfO₂ priming layer, again as a result of the substrate's original ZnO surface being increasingly converted into a HfO₂ one. The MGPC did not reach a steady value until ≥ 7 HfO₂ cycles, indicating that it required ≥ 7 cycles of the HfO₂ priming layer to fully block the incoming ZnO precursors from interfacing with the bottom ZnO layer. This result interprets that: at < 7 HfO₂ cycles, the HfO₂ layer apparently still contained molecular-scale voids—as can be discerned from the cross-sectional TEM images presented in Figure 3.7—to allow the incoming ZnO precursors (DEZn and H₂O) to diffuse through and adsorb directly onto the bottom ZnO surface, which upon subsequent ZnO deposition would conceivably result in molecular-scale ZnO conduits through the HfO₂ layer, connected to the bottom ZnO layer. Such ZnO conduits would serve as electron-conducting channels through the HfO₂ layer.

Based on this contention, the decrements of carrier concentration, electrical mobility and electrical conductivity as the number of cycles is less than 7 could be




explained as follows. Although the insulating nature of HfO_2 and the much higher conduction band position of HfO_2 , some conductive ZnO channels inside the inserted HfO_2 layers still offered paths for carriers to transmit through insulated barriers instead of tunneling; thus, there were still considerable amounts of free carriers. With regard to the degree of suppression on electrical mobility, mix 24 / nH was made up of a thin insulating layer ($< 1 \text{ nm}$) and a thick ($\sim 8 \text{ nm}$) conductive domain which consisted of one segment of mix 24:1 and 24 cycles of ZnO. The conductive domain is called as super ZnO in the rest of dissertation for convenience. In this structure, super ZnO was thick enough to build up a high mobility path for carriers, so once electrons transmitted through the thin insulating barrier, their transportation in next super ZnO was about the same as that in the previous super ZnO. Therefore, the electrical mobility was only influenced slightly and then could be maintained at $14\sim 16 \text{ cm}^2 \text{ V}^{-1} \text{ s}^{-1}$. As for Seebeck coefficients, since the reduction of carrier concentration in mix 24 / nH ($n < 7$) was mainly attributed to the shrinkage of total transmission area, which is energy-independent. Thus, the distribution of carriers with energy didn't change and then the Seebeck coefficient was maintained at $\sim 64 \mu\text{V K}^{-1}$.

As the cycles of inserted HfO_2 was more than 7, conducting ZnO channels no longer existed inside the insulated HfO_2 layers, so the carriers could only transmit through the barriers by tunneling effect. Thanks to the atomic-scale thickness of HfO_2 ,

most of carriers were able to go across the barriers, so the decrement of carrier concentration was still moderate. As for the electrical mobility, it was as the same as the case when cycles were less than 7, once electrons tunneled through the thin insulating barrier, their transportation in next super ZnO was almost as the same as that in pervious super ZnO, so the electrical mobility could still be maintained at $\sim 14 \text{ cm}^2 \text{ V}^{-1} \text{ s}^{-1}$.

Besides, it is noteworthy that the absolute value of Seebeck coefficient increased abruptly when the cycles of HfO₂ become 7 and then dropped. This phenomenon might result from energy filtering effect. Typically, energy filtering effect is conducted by a material whose conduction band is located around the Fermi level of the matrix material, which is mentioned in section 1.3.2. However, the great difference of conduction band position between HfO₂ and ZnO, i.e. $\sim 1.6 \text{ eV}$, was unfavorable for energy filtering effect. Luckily, 7 cycles of HfO₂ was still quite thin, so it didn't build up a thick barrier. For this reason, only carriers with low energy were blocked intensely but most of carriers with high energy were able to tunneling through barriers, so the energy-dependent tunneling effect may also be referred to energy filtering effect. However, as the thickness of HfO₂ increased, i.e. 9 cycles, the barrier was too thick for the carriers to tunnel through and then greatly blocked the transmission of the carriers, so the absolute value of Seebeck coefficient dropped. Figure 3.8 shows the energy band alignment and Figure 3.9 shows the transportation of carriers with different cycles of inserted HfO₂.



Referring to thermal conductivity, multi-cycle of inserted HfO₂ indeed blocked the transportation of phonons effectively and therefore suppressed the thermal conductivity obviously, i.e. lower to $1.95 \pm 0.02 \text{ W m}^{-1} \text{ K}^{-1}$. Since multi-cycle of inserted HfO₂ completed the heterogeneous interface which could serve as phonon scattering center that slowed the transportation of phonons intensely. Besides, the formed HfO₂ domain also retarded the transportation of phonons by producing serial thermal resistance due to its low thermal conductivity characteristic, i.e. $\sim 1.0 \text{ W m}^{-1} \text{ K}^{-1}$. Our result roughly conformed to the simulation done by Karttunen et al.¹⁰⁰, the max mean free path (Max. MFP) of phonon in super ZnO is near 8 nm, which was as the same as the thickness of super ZnO, since the thick and complete HfO₂ layers might scatter the phonons whose MFP is longer than 8nm. In Figure 3.10, setting Max. MFP at 8nm yields a cumulative thermal conductivity about $\sim 2.0 \text{ W m}^{-1} \text{ K}^{-1}$. Combining the serial thermal resistance resulted from HfO₂, the predicted thermal conductivities of mix 24 / 7H and mix 24 / 9H were $1.91 \text{ W m}^{-1} \text{ K}^{-1}$ and $1.86 \text{ W m}^{-1} \text{ K}^{-1}$, respectively, which were close to our results. The deviation was quite reasonable because HfO₂ layers couldn't serve as a complete phonon blocking layers as we assumed in estimation.

In Table 3.7, it reveals that the thermal conductivity decreases monotonically with the cycles of inserted HfO₂. Although we might keep decreasing the thermal conductivity by increasing the number of HfO₂ cycles, the insulation characteristic of

HfO₂ was going to make mix 24 / nH become insulated. Hence, after striking a balance between all effects, mix 24 / 7H showed the best the overall effect on enhancing ZT, and the degree of enhancement was over a factor of 13 compared to undoped ZnO.

In summary, multi-cycle of inserted HfO₂ was able to elevate the absolute value of Seebeck coefficient by energy filtering effect at certain cycles while maintaining electrical conductivity and suppressed the thermal conductivity effectively. Thus it could enhance the ZT by a factor of ~13. Based on current results, we were going to use optimal structure, mix 24 / 7H, as a template structure for further decreasing thermal conductivity via isotope modification in the next section.



Table 3.6: The thermoelectric characteristic of the mix 24:1 HZO films inserted with 5-cycle conventional HfO₂ layers at three periodicities (as illustrated in Figure 3.4). n: carrier concentration and the unit is $\times 10^{19} \text{ cm}^{-3}$; μ : electrical mobility and the unit is $\text{cm}^2 \text{ V}^{-1} \text{ s}^{-1}$; σ : electrical conductivity, S cm^{-1} ; κ : thermal conductivity, $\text{W m}^{-1} \text{ K}^{-1}$; the unit of Seebeck coefficient is $\mu\text{V K}^{-1}$; PF is the power factor and the unit is $\times 10^{-4} \text{ W m}^{-1} \text{ K}^{-2}$.

	n	μ	σ	Seebeck	PF	κ	ZT (300k)	Normalized ZT
ZnO	4.78	18.36	140.6	-107.49 \pm 1.29	1.62	33.5 \pm 0.41	0.0015	1.00
Mix 24:1	16.72	17.30	463.5	-64.03 \pm 0.52	1.90	10.5 \pm 0.01	0.0054	3.73
1 period	11.81	14.28	270.1	-63.78 \pm 0.51	1.10	2.44 \pm 0.03	0.0135	9.29
2 periods	12.71	14.83	301.6	-63.64 \pm 0.38	1.22	2.78 \pm 0.07	0.0132	9.06
3 periods	13.19	15.22	321.2	-64.15 \pm 0.24	1.32	3.27 \pm 0.03	0.0121	8.34

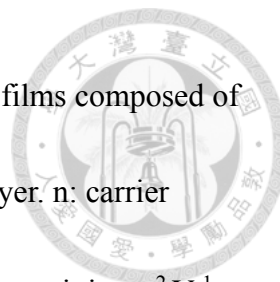


Table 3.7: The thermoelectric characteristic of undoped ZnO and the films composed of 1 period of mix 24:1 HZO and varied cycles of conventional HfO₂ layer. n: carrier concentration and the unit is $\times 10^{19} \text{ cm}^{-3}$; μ : electrical mobility and the unit is $\text{cm}^2 \text{ V}^{-1} \text{ s}^{-1}$; σ : electrical conductivity, S cm^{-1} ; κ : thermal conductivity, $\text{W m}^{-1} \text{ K}^{-1}$; the unit of Seebeck coefficient is $\mu\text{V K}^{-1}$; PF is the power factor and the unit is $\times 10^{-4} \text{ W m}^{-1} \text{ K}^{-2}$.

	n	μ	σ	Seebeck	PF	κ	ZT (300k)	Normalized ZT
ZnO	4.78	18.36	140.6	-107.49 \pm 1.29	1.62	33.5 \pm 0.41	0.0015	1.00
Con 49:1	9.42	17.90	270.2	-74.25 \pm 0.89	1.49	6.20 \pm 0.01	0.0072	4.95
Mix 24:1	16.72	17.30	463.5	-64.03 \pm 0.52	1.90	10.5 \pm 0.01	0.0054	3.73
Mix 24 / 1H	16.62	16.42	439.9	-63.46 \pm 0.87	1.77	5.77 \pm 0.03	0.0092	6.33
Mix 24 / 3H	12.68	14.95	303.8	-64.83 \pm 0.68	1.28	3.12 \pm 0.01	0.0123	8.44
Mix 24 / 5H	11.81	14.28	270.1	-63.78 \pm 0.81	1.10	2.44 \pm 0.03	0.0135	9.29
Mix 24 / 7H	10.29	14.06	237.6	-74.17 \pm 1.08	1.31	2.11 \pm 0.06	0.0186	12.77
Mix 24 / 9H	9.88	13.93	220.2	-68.35 \pm 0.96	1.03	1.95 \pm 0.02	0.0158	10.88

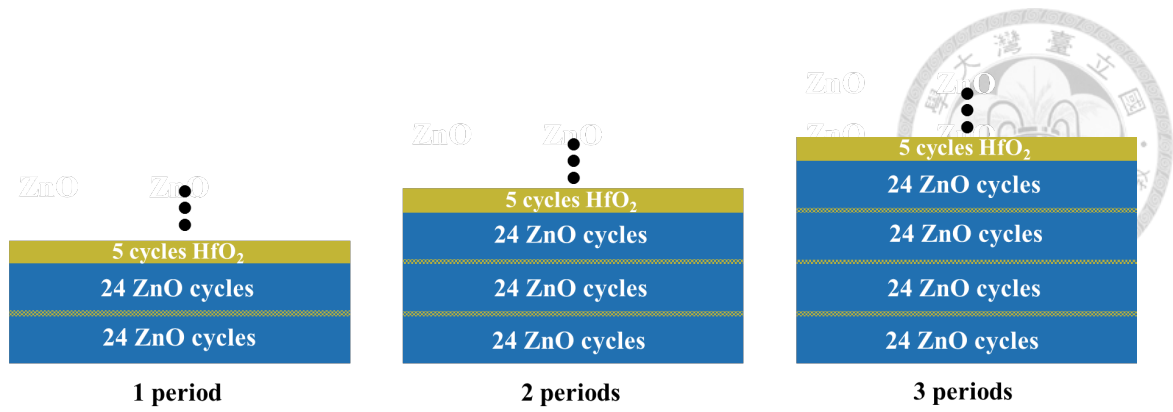


Figure 3.4: The ZnO films doped with a combination of conventional and mixed HfO₂ dopant layers.

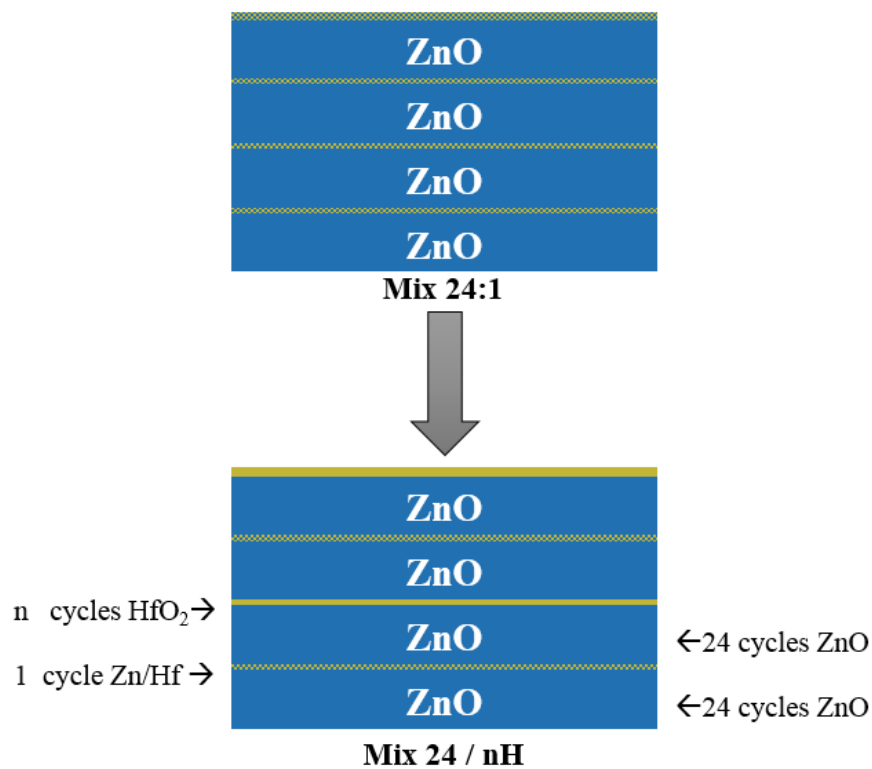


Figure 3.5: The illustration and the nomenclature of structures with 1 period of mix 24:1 HZO and varied cycles of conventional HfO₂ layer.

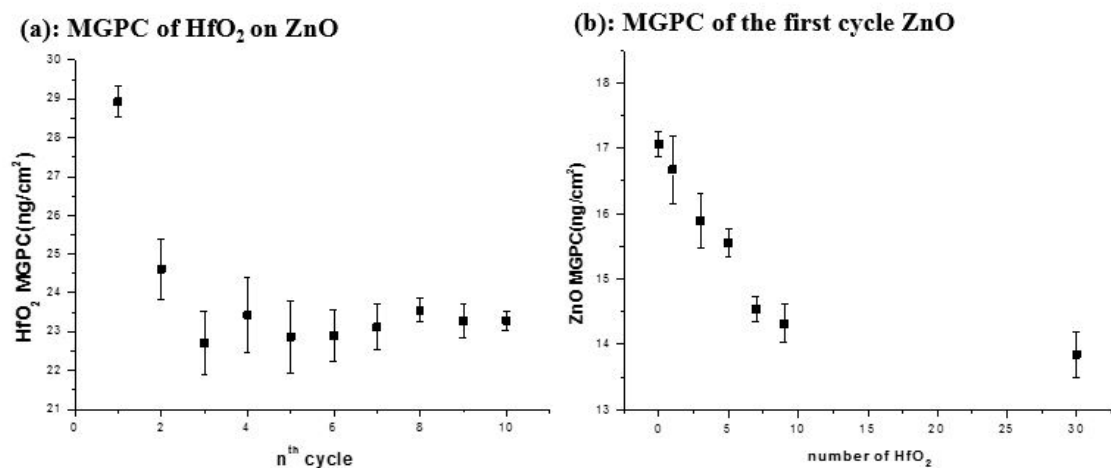


Figure 3.6: MGPC of (a) HfO₂ on the surface of 24 cycles ZnO and (b) the first cycle ZnO on the various cycles of HfO₂ acquired from in-QCM analysis.

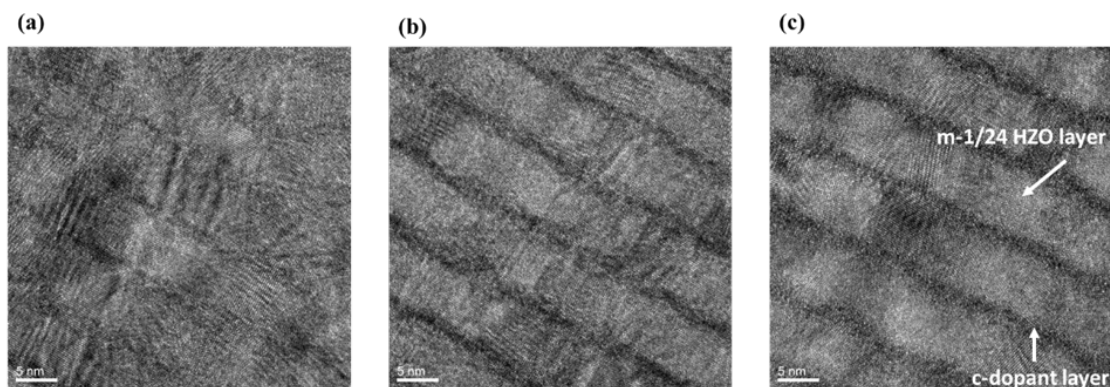


Figure 3.7: Cross-sectional TEM images of the mix 24:1 HZO films inserted with (a) 3, (b) 5, (c) 7 cycles of the conventional dopant layer at each 1 period length (24 ZnO cycles/1 m-dopant cycle/24 ZnO cycles).

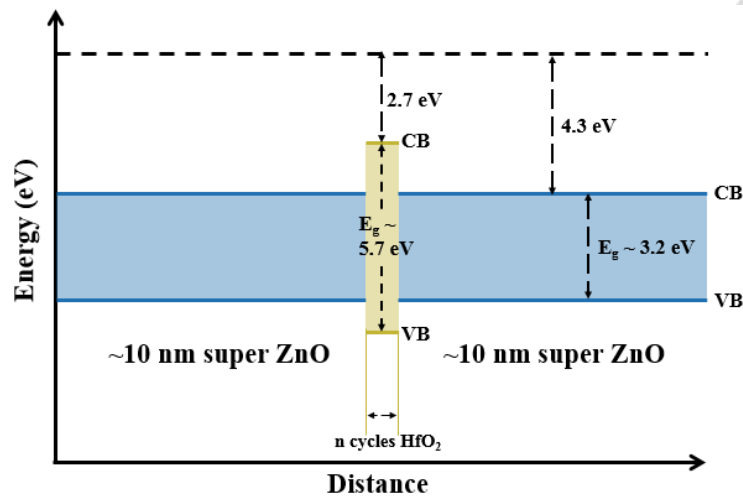


Figure 3.8: The energy band alignment of ZnO and HfO₂.

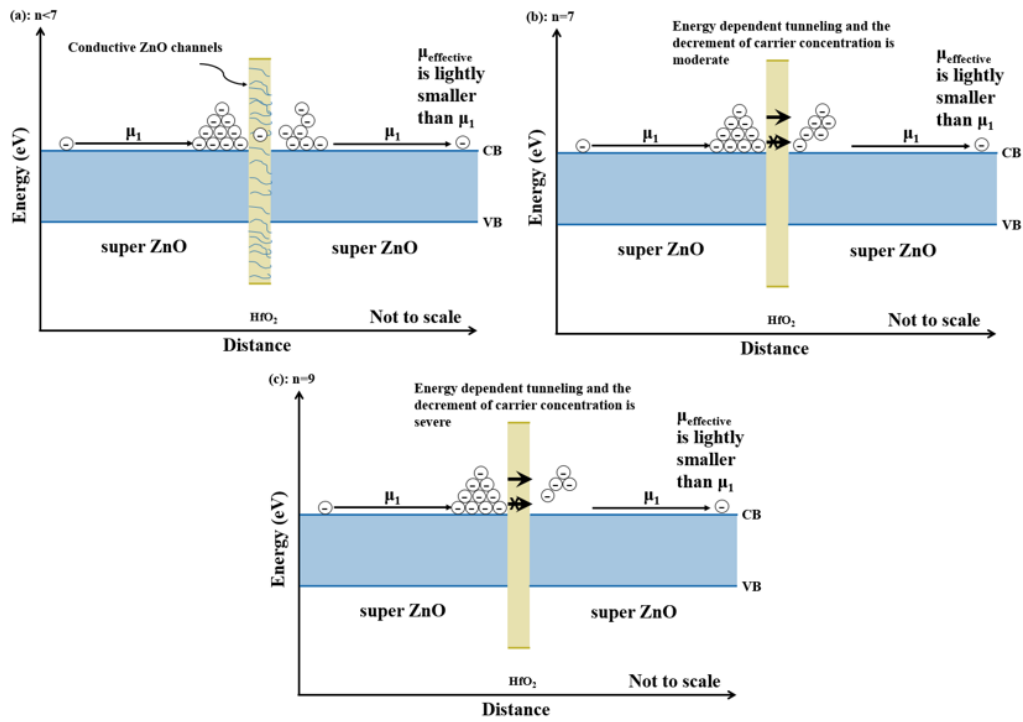


Figure 3.9: The transportation of carriers in mix 24 / nH (a) $n < 7$; (b) $n = 7$; (c) $n > 7$.

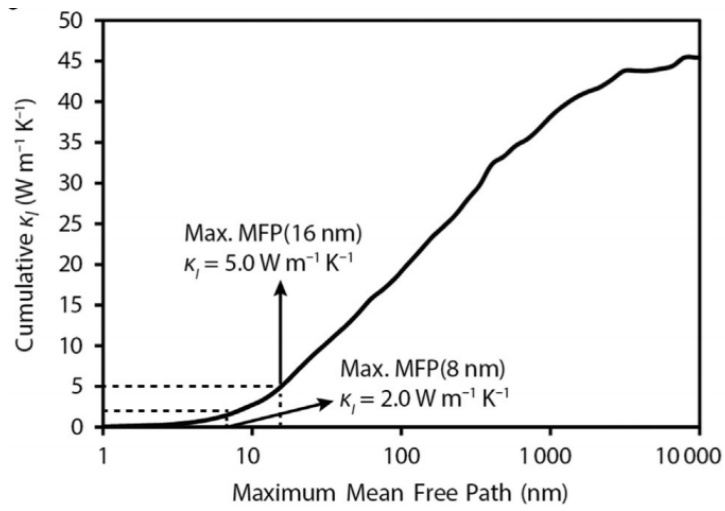


Figure 3.10: Cumulative lattice thermal conductivity of bulk ZnO at 300 K simulated by

Karttunen et al.¹⁰⁰.



3.3 Isotope superlattice

3.3.1 Modification of deposition parameters

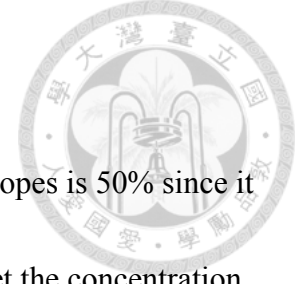
In order to verify the reactivity and the robustness of process via using H_2^{18}O as the source oxygen in depositing isotope superlattice, we deposited the mix 24 / 7H using H_2^{18}O as the oxygen source solely. For convenience, this type of doped ZnO was called as mix 24 / 7H- ^{18}O and the one using normal water as the oxygen source only was named as mix 24 / 7H- ^{16}O . It could be discovered that mix 24 / 7H- ^{18}O showed a decayed characteristic compared to that of mix 24 / 7H- ^{16}O , such as electrical conductivity and refractive index. Since the condensability of H_2^{18}O was lightly higher than that of H_2^{16}O due to the higher molecular weight^{101,102}. Thus, this result could be attributed to multilayer condensation of H_2^{18}O while using the same deposition parameter as mix 24 / 7H- ^{16}O , which might cause a non-ALD growth and then deposit a slightly looser film. For this reason, the thickness increased and the refractive index decreased. Referring to electrical conductivity, non-prefect growth lowered the electrical mobility; besides, the formed defects might serve as the carrier traps, which cut down the carrier concentration. To address the issue of redundant physisorbed H_2^{18}O , we prolonged the purge time of H_2^{18}O from 5s to 8s arbitrarily. It turned out that modified mix 24 / 7H- ^{18}O showed the same electrical characteristic as mix 24 / 7H- ^{16}O . Therefore, our hypothesis held that the electrical properties of ALD deposited ZnO were

maintained even oxygen isotope was incorporated intentionally, since ^{16}O and ^{18}O show almost the same electrical properties. The electrical characteristic, thickness and the refractive index of mix 24 / $7\text{H-}^{16}\text{O}$, mix 24 / $7\text{H-}^{18}\text{O}$ and modified mix 24 / $7\text{H-}^{18}\text{O}$ are listed in Table 3.8.

Table 3.8: The electrical characteristic, thickness and the refractive index of mix 24 / $7\text{H-}^{16}\text{O}$, mix 24 / $7\text{H-}^{18}\text{O}$ and modified mix 24 / $7\text{H-}^{18}\text{O}$. n: carrier concentration and the unit is $\times 10^{19} \text{ cm}^{-3}$; μ : electrical mobility and the unit is $\text{cm}^2 \text{ V}^{-1} \text{ s}^{-1}$; σ : electrical conductivity, S cm^{-1} . The unit of thickness is nm.

	n	μ	σ	Thickness	Refractive index
Mix 24 / $7\text{H-}^{16}\text{O}$	10.55	14.06	237.6	89.46	2.01
Mix 24 / $7\text{H-}^{18}\text{O}$	8.53	12.33	168.5	90.83	1.99
Modified mix 24 / $7\text{H-}^{18}\text{O}$ /H_2^{18}O purge 8s	10.04	14.28	229.4	89.21	2.01

3.3.2 Influence on thermoelectric properties



According to reported works, the optimal concentration of isotopes is 50% since it ensures the highest dissimilarity in mass difference. Thus, we also set the concentration of ^{18}O in our research at 50% and then varied the periodicity to make sure the influence of isotope superlattice on thermoelectric properties. Figure 3.11 shows the nomenclature of structure discussed in this section, and the measured characteristics are listed in Table 3.9. It is noteworthy that the purge time of H_2^{18}O in the research was set at 8s based on our previous result.


Starting with electrical characteristic, all the ^{18}O incorporated films showed the almost unperturbed electrical performance regardless of periodicity of superlattice which were consistent with our assumption. Hence, the power factors of them were retained at $\sim 1.30 \times 10^{-4} \text{ W m}^{-1} \text{ K}^{-2}$. On the other hand, the thermal conductivity was affected by the period length of superlattice; especially, it decreased considerably at the moderate period length, i.e. 2~4 nm, but otherwise changed slightly. In order to elucidate this phenomenon, the detailed phonon transportation parameters had to be taken into consideration, such as wavelength of phonons, mean free path of phonons and DOS of phonons.

Figure 3.12 is the contribution ratio of each phonon mode in ZnO, which was simulated by Wu et al.¹⁰³, it clearly revealed that the modes below band gap almost

dominated the thermal conductivity completely at 300K. By consulting Figure 3.13, which is the phonon group velocity as a function of frequency for ZnO simulated by Wu et al.¹⁰³ also, the wavelengths of these phonons are estimated to be around 0.5~7 nm.

Hence, the mass difference interfaces resulted by 7H 7:7 isotope superlattice were invisible to most of phonons since the distance between interfaces was only~1.2nm.

Based on this contention, 7H 7:7 structure just affected the effective mass of phonons instead of introducing additional scattering centers; therefore, the reduction of thermal conductivity was slight. As the distance of mass difference interface (or the period length of superlattice) increased, more phonons were scattered since interfaces became visible; thus, the reduction of thermal conductivity became considerable. However, the effect on reducing thermal conductivity dropped obviously as the distance of mass difference interface became quite long, e.g. ~9 nm in 7H 56:56. This result could be attributed to no mass difference interface inside super ZnO, so the distribution of phonon mean free path in ZnO was unperturbed, which was almost as the same as that in mix 24 / 7H structure; therefore, the only difference was that the effective mass was increased. Besides, the density of thick HfO₂ layers was also increased, which enhanced the scattering effect, so the thermal conductivity of 7H 56:56 was lower than the linear combination of mix 24 / 7H and mix 24 / 7H-¹⁸O, i.e. 2.05 W m⁻¹ K⁻¹ and 2.09 W m⁻¹ K⁻¹, respectively.



Referring to the degree of reduction on thermal conductivity, our result was about 18%, which was far lower than the best result (~50%) in $^{12}\text{C}/^{13}\text{C}$ graphene system demonstrated by Chen et al.⁸⁹. By the simulation done by Wang et al.¹⁰⁴ which can be seen in Figure 3.14, it clearly revealed that the DOS of the modes below the band gap (which dominate the thermal conductivity in room temperature) were mainly contributed from the vibration of zinc atoms since they are much heavier than oxygen atoms. Therefore, the low degree of reduction on thermal conductivity owing to the ^{18}O incorporation was reasonable.

To sum up, we demonstrated the isotope incorporated superlattice by the usage of H_2^{18}O as the source of oxygen in depositing HZO. Thanks to the same electrical properties between ^{16}O and ^{18}O , the power factor of deposited structure was unperturbed regardless of periodicity of superlattice. Nonetheless, the mass difference interfaces impeded the transportation of phonons effectively at certain distance, so the degree of reduction on thermal conductivity was up to ~20%. With these two effects, the ZT value could be further enhanced by the factor of ~20% while remaining the optimal structure developed in section 3.2.2.

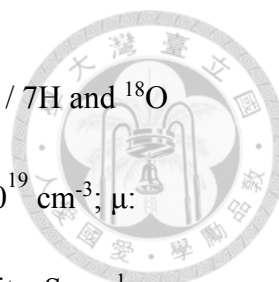


Table 3.9: The thermoelectric characteristic of undoped ZnO, mix 24 / 7H and ¹⁸O

incorporated superlattice. n: carrier concentration and the unit is $\times 10^{19} \text{ cm}^{-3}$; μ :

electrical mobility and the unit is $\text{cm}^2 \text{ V}^{-1} \text{ s}^{-1}$; σ : electrical conductivity, S cm^{-1} ; κ :

thermal conductivity, $\text{W m}^{-1} \text{ K}^{-1}$; the unit of Seebeck coefficient is $\mu\text{V K}^{-1}$; PF is the

power factor and the unit is $\times 10^{-4} \text{ W m}^{-1} \text{ K}^{-2}$.

	n	μ	σ	Seebeck	PF	κ	ZT (300k)	Normalized ZT
ZnO	4.78	18.36	140.6	-107.49 \pm 1.29	1.62	33.5 \pm 0.41	0.0015	1.00
Mix 24 / 7H- ¹⁶ O	10.29	14.06	237.6	-74.17 \pm 1.08	1.31	2.11 \pm 0.06	0.0186	12.77
Mix 24 / 7H- ¹⁸ O	9.97	14.88	237.4	-73.79 \pm 0.74	1.29	2.07 \pm 0.03	0.0187	12.88
7H 7:7	10.36	14.23	236.1	-74.07 \pm 0.41	1.30	2.05 \pm 0.02	0.0190	13.03
7H 14:14	10.27	13.98	229.7	-74.52 \pm 0.27	1.28	1.91 \pm 0.05	0.0200	13.77
7H 28:28	10.46	14.16	236.9	-73.88 \pm 0.36	1.29	1.76 \pm 0.04	0.0220	15.15
7H 56:56	10.36	14.35	237.8	-74.43 \pm 0.46	1.32	2.05 \pm 0.03	0.0194	13.32

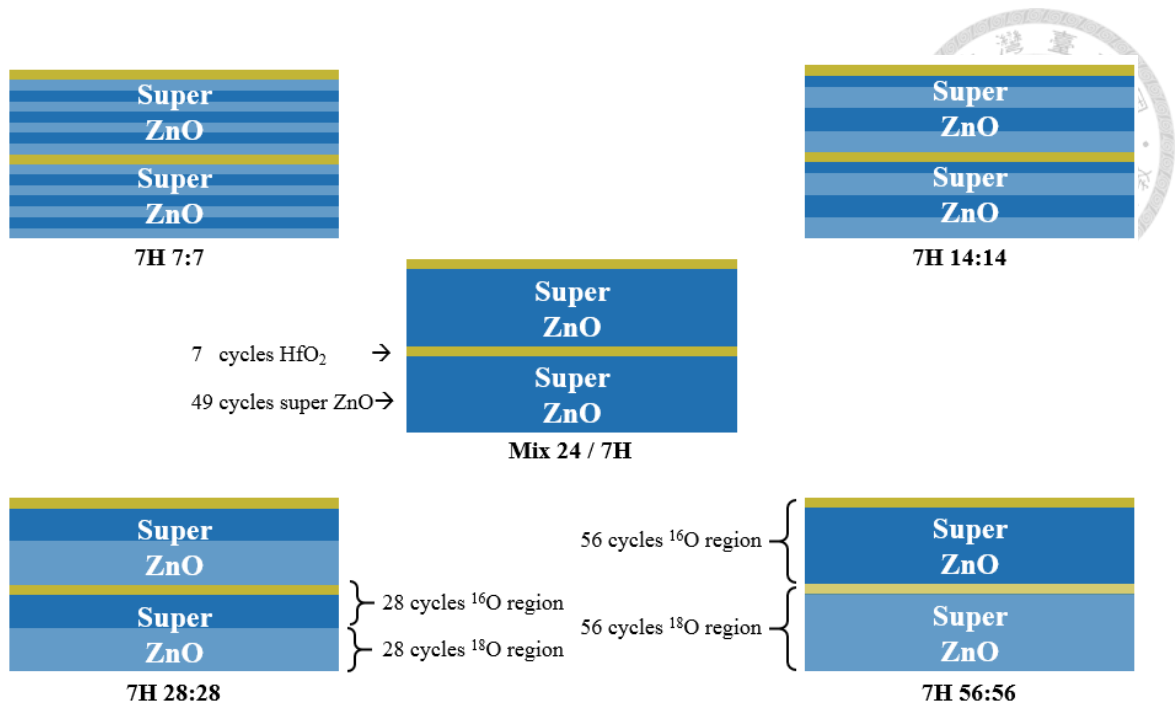


Figure 3.11: The nomenclature of structures which are isotope incorporated.

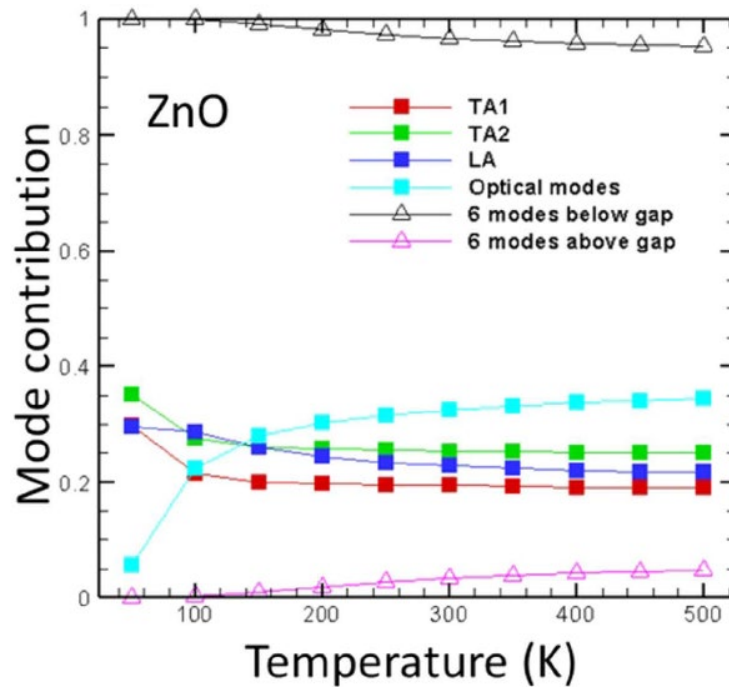


Figure 3.12: The contribution ratio of each phonon modes in ZnO which is simulated by

Wu et al.¹⁰³.

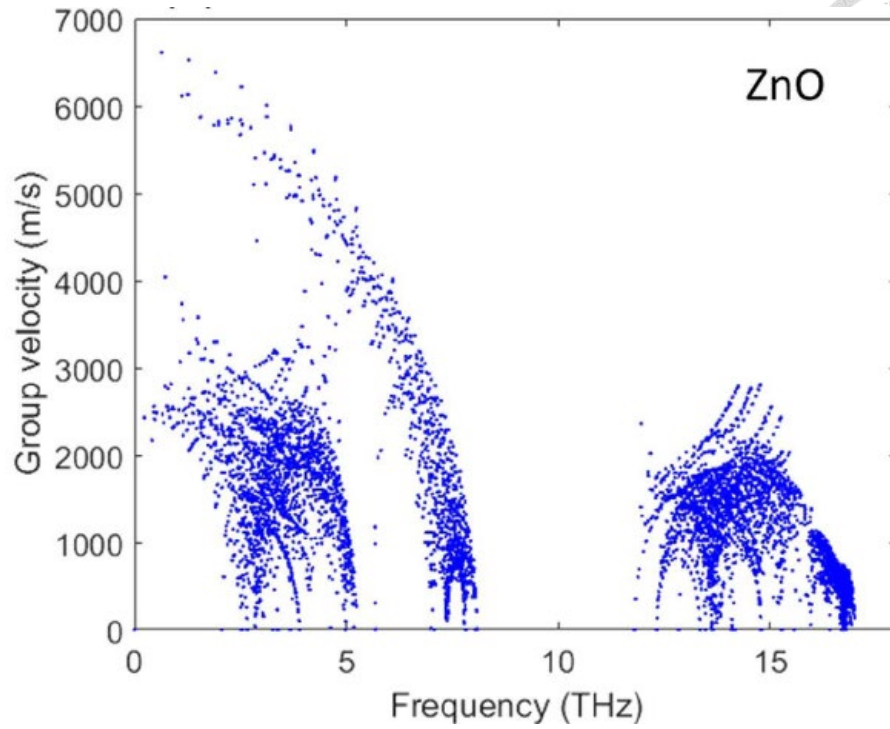


Figure 3.13: The phonon group velocity as a function of frequency for ZnO simulated by Wu et al.¹⁰³.

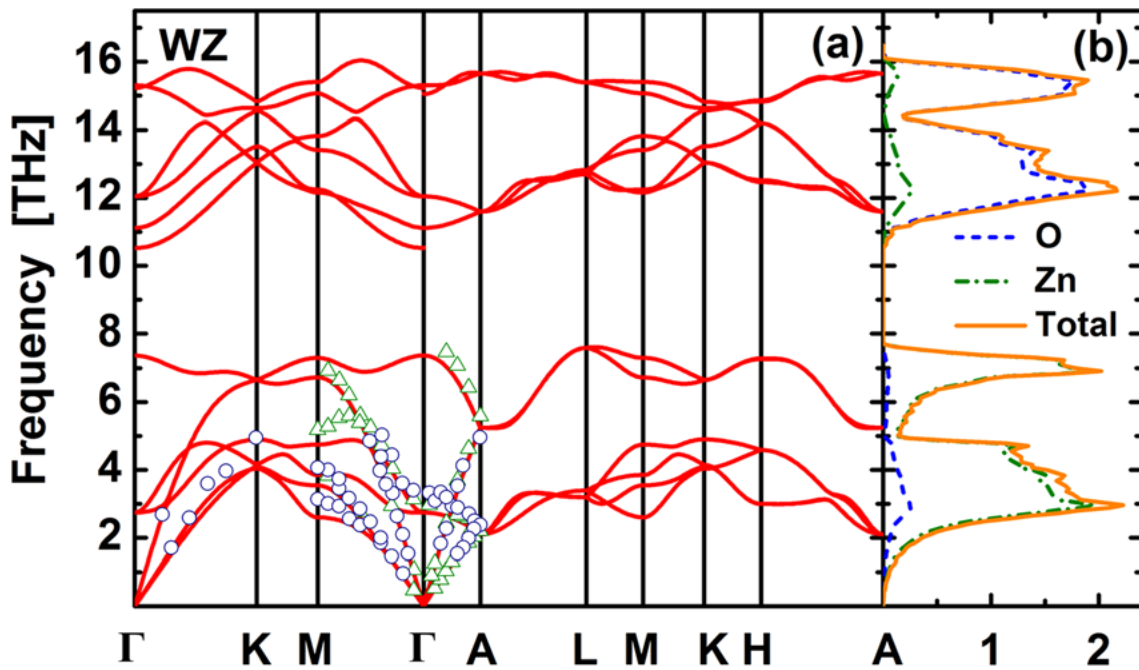


Figure 3.14: The simulation done by Wang et al.¹⁰⁴ (a) phonon dispersion curves of wurtzite ZnO; (b) vibrational density of states of wurtzite ZnO.

3.4 Summary



In this chapter, the study started with the selection of dopants. In order to clarify the influence of properties of dopants on thermoelectric characteristic, we chose three tetravalent metal ions in the same group(IVB group) as dopants, i.e. Ti^{4+} , Zr^{4+} and Hf^{4+} ; moreover, we also used the precursors with the same functional ligand to control the reactivity. After systematical investigation, we concluded that Hf^{4+} showed the greatest benefit on enhancing thermoelectric performance of ZnO (6 times improvement), since the incorporation of Hf didn't decrease the electrical mobility severely. This advantage ensured the enhancement of the electrical conductivity without increasing carrier concentration greatly. Thus, the high absolute value of Seebeck coefficient was maintained. Besides, the great mass difference between Hf and Zn suppressed the thermal conductivity effectively.

However, the electrical conductivity was only enhanced by the factor of 2.5 due to the low doping efficiency of conventional ALD doping process. Thus, we proposed a new doping technique, i.e. mixed ALD doping process, to further increase the electrical conductivity. At the optimal doping concentration, the highest conductivity was almost 5-fold more compared with undoped ZnO. Unfortunately, an abundance of free carriers lowered the absolute value of Seebeck coefficient and the loosely distributed dopants no longer impeded the transportation of phonons effectively. For this reason, the degree of

enhancement on ZT value, which was only about 4.5 times, was unsatisfactory.

Afterward, we combined the advantages of conventional process and mixed ALD doping process to deposit HZO superlattices, i.e. heat blocking for conventional process and excellent electrical performance for mixed ALD doping process. After striking a balance between all effects, we conclude that 7-cycle HfO_2 was the optimal heat and electrical barrier to incorporate with super ZnO, because it could increase the absolute value of Seebeck coefficient by energy filtering effects and impeded heat transport by forming distinct HfO_2/ZnO interface. Hence, the overall enhancement on ZT value was over an order of magnitude (~ 13 times).

Finally, we investigated the effect of isotope incorporation on thermoelectricity in compound materials for the first time. After modifying the deposition parameters, the electrical performance of ^{18}O -containing films was about the same with the normal films (^{18}O -excluding). After that, we controlled the period length of superlattice to probe the interface-distance dependent thermal conductivity in our systems. It turned out that the optimal periodicity was determined to be 4.5/4.5 nm, which best matches the majority phonon wavelengths of ZnO. Therefore, regarding the enhancement on ZT, the further 20% increment was achieved and the ZT value of optimal ZnO was about 0.023 at 300K, which was about 16 times higher than that of undoped ZnO.

Chapter 4

Metal oxide/polymer superlattice



As we stated in section 1.8.3, the deposition of conducting polymers by MLD technique was developed to prepare the insertion material in metal oxide/polymer superlattice. In the research, three common conducting polymers were tested, i.e. polythiophene, polyaniline and PEDOT. Among the deposition processes, PEDOT-process possessed the following merits: reproducibility, robustness and the high electrical conductivity of the deposited films. Although the research started with the deposition of polythiophene and polyaniline, the focus of this chapter was on the characteristic and the deposition process of PEDOT and its metal oxide/polymer superlattice. As for the deposition of polythiophene and polyaniline, they are stated in the latter part of this section.

4.1 Poly(3,4-ethylenedioxythiophene) (PEDOT)

4.1.1 The deposition of PEDOT


In the development of depositing polyaniline by MLD technique, we noticed that the vapor pressure of oxidant, i.e. SbCl_5 , decayed with time if the temperature was elevated. It might be due to the high oxidizing power nature which made itself unstable. For addressing the stability issue, prolonging the pulse time was utilized to increase the

amount of vapor phase SbCl_5 molecules instead of elevating the temperature of SbCl_5 .

Thus, we set the temperature of SbCl_5 at 75°C , at which the degradation was less obvious. For the detailed experimental settings, they can be found in Table 2.6. The characteristics of deposited PEDOT films are summarized in Table 4.1.

First, the blue appearance of deposited films shown in Figure 4.1 and the characteristic absorption peaks in FTIR spectrum (Figure 4.2) confirmed the formation of PEDOT by MLD process. In FTIR spectrum, 10 typical absorption bands of PEDOT are listed as follow: 1519, 1312, 1206, 1133, 1079, 1032, 969, 912, 829, and 690 cm^{-1} . The bands at 1519 and 1312 cm^{-1} are originated from the stretching mode of $\text{C}=\text{C}$ and $\text{C}-\text{C}$ in thiophene ring. The bands around 1206, 1133, 1079, and 1032 cm^{-1} are attributed to the bending mode of $\text{C}-\text{O}-\text{C}$ in ethylenedioxy groups; the bands at 969, 912, 829, and 690 cm^{-1} are identified as the stretching mode of the $\text{C}-\text{S}-\text{C}$ bond in thiophene ring. All bands mentioned above and the absence of the peak at 754 cm^{-1} which is attributed to $\text{C}-\text{H}$ of the aromatic structure confirmed the successful formation of the PEDOT in MLD process.

As for thermoelectric properties, MLD-deposited PEDOT showed a high electrical conductivity without post-treatments, which were common ways to promote the electrical conductivity of PEDOT; however, it showed a poor absolute value of Seebeck coefficient. This characteristic was attributed to high doping level of deposited



PEDOT. In Figure 4.3, which is the UV-Vis spectrum of our PEDOT, there are two characteristic peaks at about 400-700 nm and 1000-1060 nm with a free tail extending into the near-infrared region. These two peaks are ascribed to the π - π^* transitions of thiophene ring and polaron and/or bipolaron bands for oxidized PEDOT with long conjugation length, respectively. A high absorbance in near-infrared region relative to visible light region indicated the high doping level of PEDOT deposited by MLD process; hence, a high carrier concentration in PEDOT was expectable, which yielded a high electrical conductivity but low absolute value of Seebeck coefficient, thus a low power factor. Regarding thermal conductivity, our PEDOT showed a typical behavior of polymers that is almost thermally insulated and the thermal conductivity is lower than unity. Considering all effects, the ZT value of our PEDOT was only 0.051 at 300 K, which made it improper to serve as a particle thermoelectric material by itself.

Compared to the MLD polyaniline process we developed, there were two merits in PEDOT deposition process. First, it is obvious that the deposited films were highly conductive unlike MLD deposited polyaniline and performed a typical p-type conducting. Without post-treatment which was commonly conducted to promote electrical conductivity, such as acid rinse, the conductivity of our PEDOT films were over 400 S cm^{-1} that could compete with those synthesized by traditional solution process. Second, it is noteworthy that the growth rate of PEDOT was almost ten times

higher than that of polyaniline we deposited, i.e. 0.3~0.4 nm/cycle and 0.03 nm/cycle, respectively; hence, high growth rate ensured the practicability of MLD deposited PEDOT in various applications. Thanks to these advantages, MLD deposited PEDOT was promising and then chosen as the insertion material in developing metal oxide/polymer superlattice thermoelectric materials.

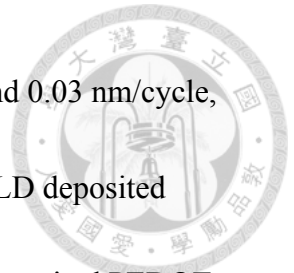


Table 4.1: The characteristic of deposited PEDOT films.

Thickness (nm)	Growth rate (nm/cycle)	σ (S cm ⁻¹)	Seebeck (μ V K ⁻¹)	PF (10 ⁻⁴ W m ⁻¹ K ⁻²)	κ (W m ⁻¹ K ⁻¹)	ZT (300k)
60.6	0.303	456.6	8.39	0.032	0.19	0.0051

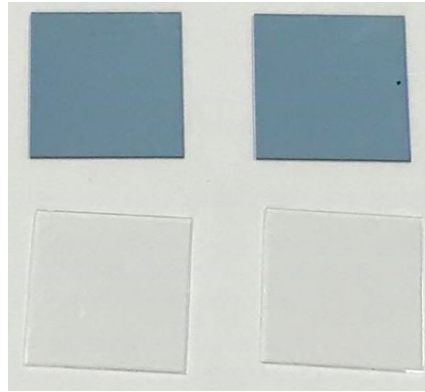


Figure 4.1: The photographs of deposited PEDOT films and blank glass substrates.

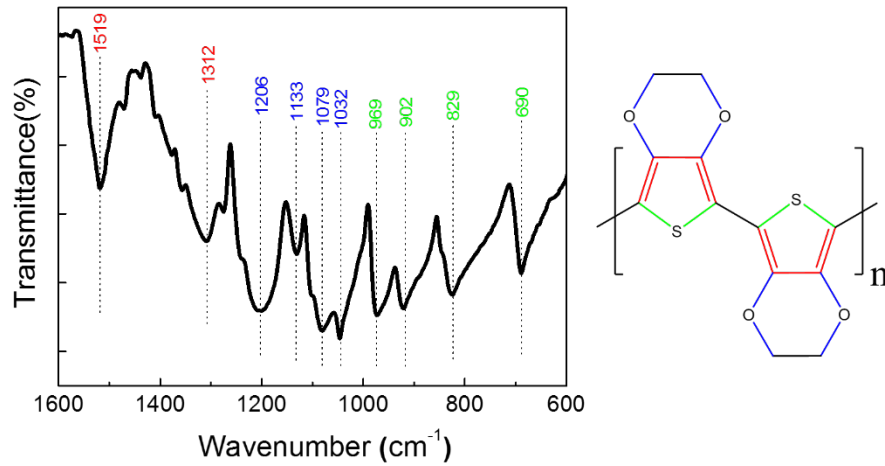


Figure 4.2: The FTIR spectrum of deposited PEDOT films.

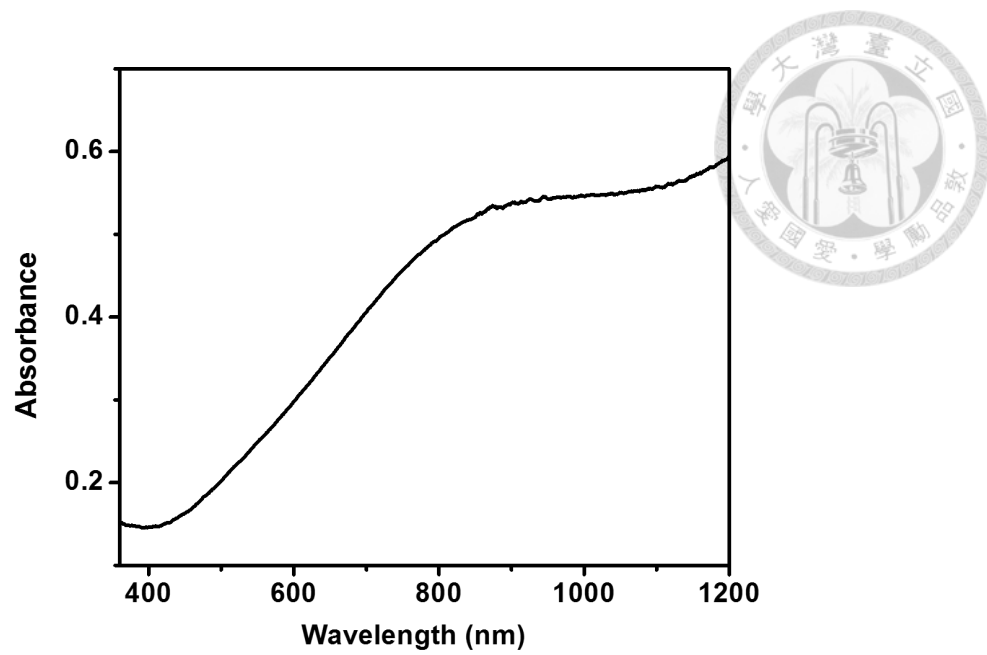


Figure 4.3: The UV-Vis spectrum of deposited PEDOT films.

4.1.2 Interface-engineering of metal oxide/PEDOT superlattice

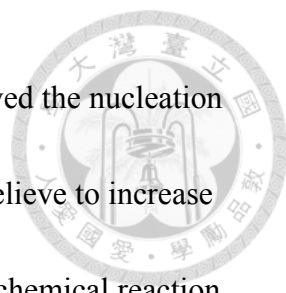


As we stated in previous section, PEDOT was selected as an insertion material and utilized to develop conducting polymer incorporated HZO superlattice thermoelectric materials due to its high growth rate and conductivity. However, the integration of two processes pressed for an investigation before depositing HZO/PEDOT superlattices, since PEDOT and HZO didn't offer proper reaction sites for each other to nucleate during switching.

To address this issue, we first monitored the growth of PEDOT on the surface of ZnO using the pristine deposition settings (same as those in previous section) by QCM. In Figure 4.4, it shows the mass gain of the one-cycle PEDOT on the surface of ZnO using different pulse sequence of precursors. It can be seen clearly that mass gain of EDOT dose approached to zero in the pristine pulse sequence (EDOT first) even incoming SbCl_5 indeed chemisorbed onto the surface. This phenomena revealed two facts: EDOT monomers couldn't adsorb onto the surface on ZnO; SbCl_5 molecules could react with surface functional groups of ZnO. These two facts concluded that no PEDOT formed after one cycle of PEDOT-deposition. However, as we changed the pulse sequence (SbCl_5 first), there were positive mass gains after the pulse of both precursors, which meant PEDOT indeed formed by this pulse sequence. Besides QCM analysis, the growth mechanism could be also discerned by cross sectional TEM images

presented in Figure 4.5: the inserted PEDOT layers can be seen in Figure 4.5 (b), but no layered structures in Figure 4.5 (a). Hence, the modified pulse sequence, i.e. SbCl_5 was introduced first, was utilized to deposit inserted PEDOT layers in superlattice; moreover, the multiple pulse process of EDOT, i.e. $\text{SbCl}_5 \rightarrow \text{EDOT} \rightarrow \text{EDOT} \rightarrow \text{EDOT}$, was also utilized to ensure the growth of PEDOT under few cycles of deposition.

After dealing with the modification of PEDOT deposition process, we further investigated the growth of incoming ZnO on the surface of inserted PEDOT layers to optimize the deposition process of HZO. In Figure 4.6, it shows the MGPC of ZnO at the steady-growth region and the mass gain of the first cycle using the normal depositing parameters (i.e. without exposure) of ZnO on surface of inserted PEDOT with various modifications. The low mass gain of ZnO depositing without any modification interpreted the poor nucleation and growth of ZnO on the surface of inserted PEDOT as we expected. However, after conducting each modification, the mass gain truly increased which validates the profit of interface-engineering. In type A, the exposure of SbCl_5 during depositing PEDOT was abrogated to eliminate redundant physisorbed molecules since unreacted SbCl_5 molecules were nearly inert to the incoming H_2O which was analyzed by QCM shown in Figure 4.7, and thus hinder the nucleation of ZnO; in type B, long exposure time (25 seconds) of each precursor was utilized to increase the physisorbed precursors and/or reaction probability (by increasing



collision between gas-phase molecules and surface), and then improved the nucleation of ZnO on the surface of PEDOT; in type C, the dose of H₂O₂ was believed to increase the density of hydroxyl groups on the organic surface which offered chemical reaction sites for incoming precursors of ZnO, and thus improved nucleation and growth of ZnO. For achieving best improvement in the mass gain of ZnO, three types of modifications were applied simultaneously to enhance the growth of incoming ZnO synergistically, and the result was outstanding since the mass gain was almost 2.5 times to the one without any modification. Moreover, the electrical conductivity of PEDOT/HZO superlattice with various modifications was measured to evaluate efficacy of modifications, the measured electrical conductivities are summarized in Table 4.2. The result tallied with the observation by QCM analyses in previous discussions. It could be seen that electrical mobility was enhanced significantly indicating the reformed quality of HZO and interface between each layers that were originated from the improvement of the nucleation and growth of ZnO of the surface of PEDOT.

In summary, the interface-engineering was explored to integrate ALD-HZO and MLD-PEDOT processes to deposit HZO/PEDOT superlattice. The interface-engineering included the modification of PEDOT process to ensure the growth of PEDOT under few cycles of deposition and the modification of PEDOT/ZnO interfaces to improve the quality of ZnO (HZO). The modifications of PEDOT process included

switching pulse sequence (SbCl_5 first), abrogating the exposure time of SbCl_5 and utilizing multiple pulse of EDOT monomers. Besides, two modifications were applied before the deposition of ZnO using normal parameters: the dose of H_2O_2 to increase the density of surface hydroxyl groups and 5-cycle nucleation process of ZnO that substituted 5 cycles with normal parameters to promote nucleation.

Table 4.2: The electrical conductivity of PEDOT/HZO superlattice with various modifications in the structure of 6×(4 periods mix 19:1 HZO + 1-cycle PEDOT)

	n ($\times 10^{19} \text{ cm}^{-3}$)	μ ($\text{cm}^2 \text{ V}^{-1} \text{ s}^{-1}$)	σ (S cm^{-1})
Without	9.86	2.51	39.4
Type A	12.65	3.10	62.9
Type A+B	11.12	7.87	140.2
Type A+B+C	12.72	13.75	280.2

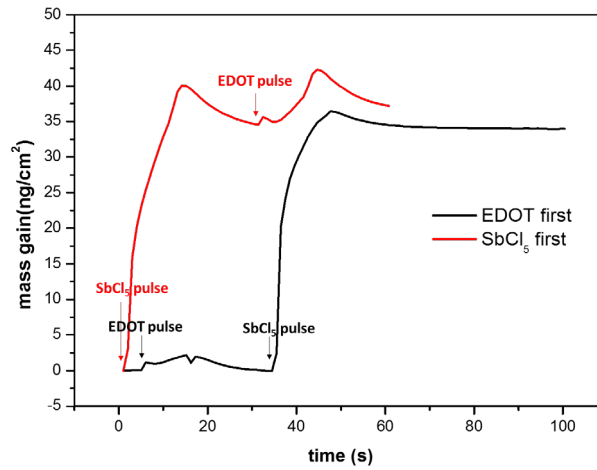


Figure 4.4: The in-situ QCM results of the deposition of PEDOT on the surface of ZnO using two kinds of pulse sequences.

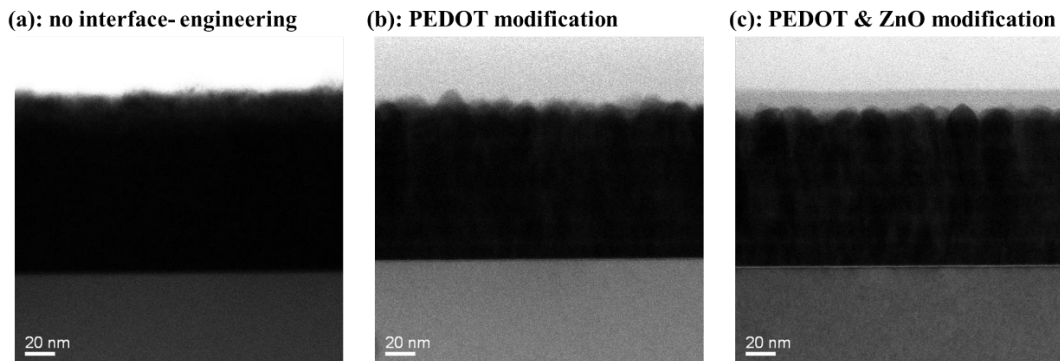


Figure 4.5: The cross sectional TEM images of deposited films in the structure of 6×(80-cycle ZnO/ 1-cycle PEDOT).

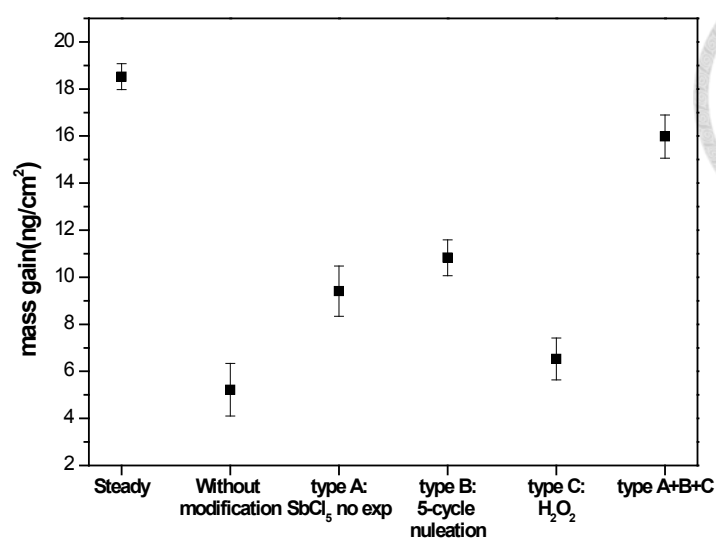


Figure 4.6: The mass gain of ZnO in steady-growth region and that on the surface of inserted PEDOT with various modifications.

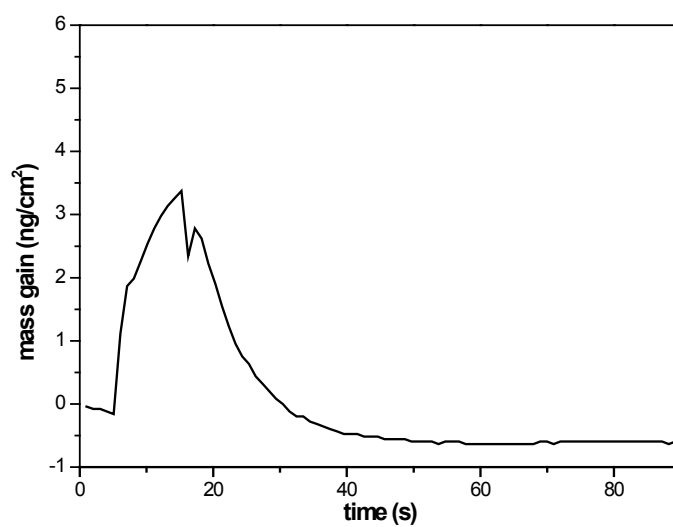
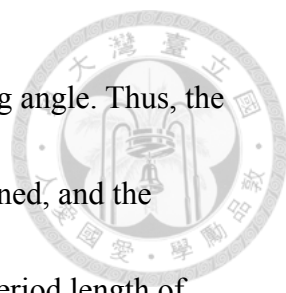


Figure 4.7: The mass gain of H₂O on surface covered by redundant SbCl₅.

4.1.3 Superlattice deposition and thermoelectric performance




After finishing the study of interface-engineering for the deposition of HZO/PEODT superlattice, there was still one remaining issue to address, the determination of “super ZnO”, which possessed the best electrical performance as stated before, to integrate with inserted PEDOT. Because of the slight variation in deposition condition between our ALD and MLD systems, e.g. working pressure and flow field of precursors, the “super ZnO” had to be determined once again. Therefore, we followed the approaches stated in section 3.2.1, tuning the insertion periodicity of mixed doping layers to acquire the best electrical performance, and then concluded that mix 19:1 HZO was the “super ZnO” in MLD system based on the highest power factor listed in Table 4.3. Thus, mix 19:1 HZO was a host material in the section to study the effects of composition and structure on the thermoelectric performance of HZO/PEDOT superlattice. However, it is noteworthy that the electrical mobility of HZO deposited by MLD system was higher than that deposited by ALD system with the same insertion periodicity of mixed doping layers. This property was attributed to the higher preferential-growth in (002) direction as XRD patterns revealed in Figure 4.8. The high preferential-growth in a conductive film yielded fast transportation paths for electrical carriers, and thus the electrical mobility of the film could be much higher than that with lower preferential-growth.



nm, β is the FWHM (Full width at half maximum), and θ is the Bragg angle. Thus, the transportation of electrical carriers and phonons were almost maintained, and the thermoelectric performance was unaffected. On the other hand, the period length of inserted PEDOT layers in the superlattice composed of 2 periods of mix 19:1 and 1-cycle PEDOT was much shorter than the distance between scattering centers of mix 19:1, and thus the inserted PEDOT layers became the major scattering centers for both carriers (heat and electric). Besides, short distance between two adjacent PEDOT layers confined the growth of ZnO crystals; therefore, the transportation of electrical carriers and phonons were retarded extremely even the nucleation and growth of ZnO on PEDOT were improved through interface-engineering. Luckily, the concurrent suppression of electrical mobility and thermal conductivity could be decoupled at medium insertion periodicity of PEDOT layers, i.e. 4 periods in our results. Since the distance between adjacent PEDOT layers in this structure was around 16 nm, which was slightly smaller than the grain size of mix 19:1 HZO, and therefore the suppression of grain growth was retarded. Furthermore, the conductive nature of PEDOT offers conducting paths for electrical carriers; thus, the electrical mobility could be maintained partially. As for thermal conductivity, the inserted PEDOT layers that were the main scattering centers for phonons in this structure could reduce the thermal conductivity obviously due to the extremely heterogeneous interface between ZnO and PEDOT.

Overall, the thermoelectric performance of superlattice composed of alternating 4-period mix 19:1 HZO host and 1-cycle PEDOT had a potential to be further improved through thickening the inserted PEDOT even though the ZT of this superlattice was not the highest one among four superlattices on this front.

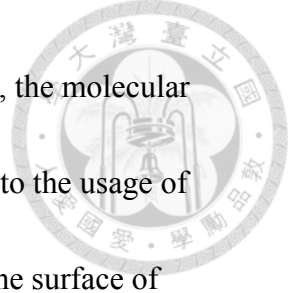
Further, the inserted PEDOT was thickened gradually and type-C modification, i.e. the dose of H_2O_2 before 5-cycle ZnO nucleation layers, was applied to optimize the performance of superlattices. The thermoelectric properties of deposited superlattices are listed in Table 4.5. The enhancement of electrical mobility (conductivity also) through the usage of type-c modification, which improved the growth and/or nucleation of ZnO, was stated in section 4.2.1. Besides, the slight increment of thermal conductivity was also attributed to modified interfaces between ZnO and PEDOT, by which the scattering of phonons was reduced. Regarding the dependence of ZT enhancement on the thickness of inserted PEDOT, we started from the reduced thermal conductivity. It could be seen that the thermal conductivity decreased with the cycle (thickness) of inserted PEDOT. This result was originated from the formation of complete and clear interfaces between ZnO and PEDOT gradually as the cycle of inserted PEDOT increased, hence the interface-scattering of phonons was enhanced due to the significant discrepancy in the type of bonds and the microstructure between ZnO and PEDOT, i.e. covalent bonds and disordered amorphousness of PEDOT versus ionic



bonds and ordered crystallinity of ZnO. The gradually-formed interfaces could be observed and confirmed by the comparison of cross-sectional TEM images presented in Figure 4.10. Moreover, the inserted PEDOT layers also offered a considerable serial thermal resistance due to its ultra-low thermal conductivity, $0.19 \text{ W m}^{-1} \text{ K}^{-1}$. Thus, the reduced thermal conductivity was obtained. However, the decrement of thermal conductivity was unsatisfactory. Based on the simple series-resistance model, which is illustrated in Figure 4.11, the theoretical thermal conductivity could be expressed as below. It is noteworthy that there were assumptions we made to simplify the calculation: (1) Cross-sectional area was unity; (2) Thermal conductance G at interfaces were the same. ($G_{\text{HZO} \rightarrow \text{PEDOT}} = G_{\text{PEDOT} \rightarrow \text{HZO}} = G = 0.2 \text{ GW m}^{-2} \text{ K}^{-1}$, which is based on the result of Mark D. Losego et al.¹⁰⁶); (3) The transportation of phonons inside HZO was unchanged even with the insertion of PEDOT.

$$R_{total} = \frac{d_{film}}{\kappa_{film}} = 5 \times \left(\frac{d_{HZO}}{\kappa_{HZO}} + \frac{d_{PEDOT}}{\kappa_{PEDOT}} + \frac{2}{G} \right) + \frac{d_{HZO}}{\kappa_{PEDOT}}$$

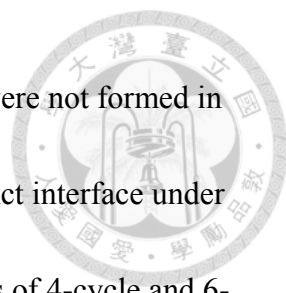
Therefore, the estimated thermal conductivity of each superlattice should be 1.49, 1.31, 1.15 and 0.95 for 1-cycle, 2-cycle, 4-cycle and 6-cycle, respectively. The estimated thermal conductivity was much lower than the measured value in all superlattices. This result indicated the lack of distinct interface and the existence of fast-transportation route for phonons in the inserted PEDOT layers. In fact, it indeed took time (or cycles) for PEDOT to form a complete layer, hence the interface



(HZO→PEDOT) might not form under low-cycle condition. Besides, the molecular scale ZnO may indeed exist inside the inserted PEDOT layers due to the usage of nucleation process, which could improve the nucleation on ZnO on the surface of PEDOT. In nucleation process, the sample was soaked in the vapor of each precursor, hence precursors had enough time to infiltrate into the superficial PEDOT, which was fluffy in structure, and then physisorbed onto it. Therefore, the molecular scale ZnO could be formed inside PEDOT during nucleation process and then diminished another distinct interfaces (PEDOT→HZO) even the deposition-cycle of inserted PEDOT increased. To evaluate the effect of inserted PEDOT on the suppression of thermal conductivity exactly, the intrinsic thermal conductance of PEDOT and the conductance of each interface were lumped as a single conductance G' , thus the equation was modified as:

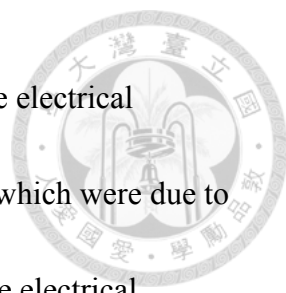
$$R_{total} = \frac{d_{film}}{\kappa_{film}} = 5 \times \left(\frac{d_{HZO}}{\kappa_{HZO}} + \frac{d_{PEDOT}}{\kappa_{PEDOT}} + \frac{2}{G} \right) + \frac{d_{HZO}}{\kappa_{PEDOT}} = 5 \times \left(\frac{d_{HZO}}{\kappa_{HZO}} + \frac{1}{G'} \right) + \frac{d_{HZO}}{\kappa_{PEDOT}}$$

The estimated G' of each superlattice was 0.51, 0.37, 0.21 and 0.14 GW m⁻² K⁻¹ for 1-cycle, 2-cycle, 4-cycle and 6-cycle PEDOT, respectively. Interestingly, our results of 1-cycle and 2-cycle PEDOT were in line with the results of Ashutosh Giri et al.¹⁰⁷, and the estimated the interface thermal conductance in ZnO/hydroquinone/ZnO structure is shown in Figure 4.12. In their result, they stated that the hydroquinone molecules were most probably attached to every other surface Zn site (50% surface

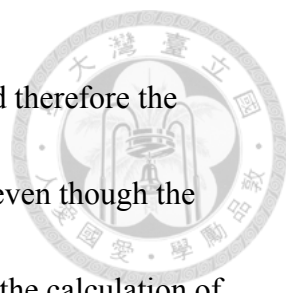


coverage) through first principles study, thus the distinct interfaces were not formed in their case. This might also interpreted the lack of complete and distinct interface under low-cycle condition as we supposed. On the other hand, in the results of 4-cycle and 6-cycle PEDOT, the estimated interface thermal conductance was lower than results of Ashutosh Giri et al. It suggested the evolution of forming distinct interfaces since our results were still higher than the half of $0.2 \text{ GW m}^{-2} \text{ K}^{-1}$ (i.e. $0.1 \text{ GW m}^{-2} \text{ K}^{-1}$ due to two interfaces in perfect layer structure). Nonetheless, the exact interface thermal conductance, G , and the thickness of pure PEDOT layers (or effective thickness) still couldn't be determined on this front; hence, more detailed analyses and structures had to be tested to clarify the effect and mechanism of inserted PEDOT on suppressing the thermal conductivity of superlattices.

As for electrical properties, the carrier concentration slightly increased in the beginning but decreased as the cycle/thickness of PEDOT increases. This may resulted from the existence of Cl^- , which can serve as an n-type dopant for ZnO as F^- did in F-doped ZnO, inside PEDOT. However, as the cycle/thickness of PEDOT increased, the degree of carrier compensation, which occurred at the interfaces due to the p-type conducting nature of PEDOT and n-type of ZnO (or HZO), became non-negligible. Thus, the carrier concentration of superlattice decreased with the thickness of inserted PEDOT layers but still remained n-type owing to great thickness (or volume) difference

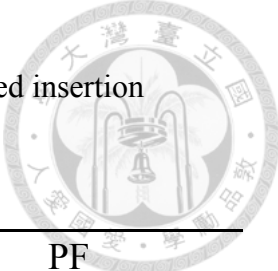


between HZO host layers and PEDOT insertion layers. Regarding the electrical mobility, the electrical barrier and the depletion region at interfaces, which were due to carrier compensation, blocked the transportation of carriers, hence the electrical mobility decreased monotonically with the cycle/thickness of PEDOT. Overall, thickening the inserted PEDOT deteriorated electrical conductivity of the superlattice. Referring to the absolute value of Seebeck coefficient, it decreased initially but increased as the cycle/thickness of inserted PEDOT increased. The decrement of the absolute value of Seebeck coefficient might be originated from the serial/parallel contribution provided by PEDOT, whose Seebeck coefficient was positive, therefore it compensated the negative Seebeck coefficient of HZO. As the cycle/thickness of inserted PEDOT increased, the electrical barriers became more established, such as the energy band of PEDOT and depletion regions, thus the inserted PEDOT could enhance the Seebeck coefficient through energy filtering effect. As the energy band alignment of PEDOT and ZnO presented in Figure 4.13, the conduction band edge of PEDOT was about 1 eV higher than that of ZnO and therefore energy filtering effect easily took place at the artificial interfaces in our superlattices. Besides, the carrier compensation also provided another route to enhance the absolute value of Seebeck coefficient since it distorted the energy band and resulted in energy barriers and depletion regions at the interfaces. Nonetheless, the improvement in the absolute value of Seebeck coefficient



still couldn't overcome the suppression of electrical conductivity, and therefore the power factor decreased with the cycle/thickness of inserted PEDOT even though the power of Seebeck coefficient was higher than that of conductivity in the calculation of the power factor. Hence, although the thermal conductivity could be further decreased through increasing the cycle/thickness of inserted PEDOT, the deteriorated power factor might compensate the merit. Overall, the ZT of superlattice could be enhanced by a factor of 7 through the insertion of 6-cycle PEDOT into mix 19:1 HZO host-layer compared with undoped ZnO deposited by MLD system.

Table 4.3: The electrical properties of ZnO and mixed HZO with varied insertion periodicity of mixed doping layers.



	n ($\times 10^{19} \text{ cm}^{-3}$)	μ ($\text{cm}^2 \text{ V}^{-1} \text{ s}^{-1}$)	σ (S cm^{-1})	Seebeck ($\mu\text{V K}^{-1}$)	PF ($10^{-4} \text{ W m}^{-1} \text{ K}^{-2}$)
ZnO	3.28	30.58	160.7	-99.01 ± 0.36	1.57
Mix 24:1	10.20	23.72	387.1	-65.29 ± 0.27	1.65
Mix 19:1	12.85	21.65	443.3	-63.01 ± 0.27	1.76
Mix 14:1	14.78	19.61	463.7	-60.79 ± 0.51	1.71
Mix 9:1	21.06	16.14	541.6	-55.37 ± 0.39	1.66
Mix 4:1	28.96	12.84	592.2	-50.83 ± 0.44	1.53

Table 4.4: The thermoelectric characteristic of the HZO/PEDOT superlattice films with varied periodicities of mix 19:1 HZO host layers.

	n (10^{19} cm^{-3})	μ ($\text{cm}^2 \text{ V}^{-1} \text{ s}^{-1}$)	σ (S cm^{-1})	Seebeck ($\mu\text{V K}^{-1}$)	PF ($10^{-4} \text{ W m}^{-1} \text{ K}^{-2}$)	κ ($\text{W m}^{-1} \text{ K}^{-1}$)	ZT (300K)
Mix 19:1	12.88	21.57	445.2	-63.01 ± 0.27	1.76	12.8 ± 0.18	0.0041
2 periods	10.63	2.14	36.4	-63.49 ± 0.98	0.15	3.30 ± 0.15	0.0013
4 periods	11.12	7.87	140.2	-55.55 ± 0.69	0.43	5.35 ± 0.10	0.0024
6 periods	11.48	17.81	327.6	-60.86 ± 0.75	1.21	11.53 ± 0.22	0.0032
8 periods	13.02	21.28	443.9	-62.59 ± 0.80	1.74	11.81 ± 0.07	0.0044

Table 4.5: The thermoelectric characteristic of the HZO/PEDOT superlattice films

composed of alternating 4 periods of mix 19:1 HZO and varied cycles of PEDOT.

	n (10^{19} cm^{-3})	μ ($\text{cm}^2 \text{ V}^{-1} \text{ s}^{-1}$)	σ (S cm^{-1})	Seebeck ($\mu\text{V K}^{-1}$)	PF ($10^{-4} \text{ W m}^{-1} \text{ K}^{-2}$)	κ ($\text{W m}^{-1} \text{ K}^{-1}$)	ZT (300K)
ZnO	3.28	30.58	160.7	-99.01 ± 0.36	1.57	33.2 ± 0.32	0.0014
Mix 19:1	12.88	21.57	445.2	-63.01 ± 0.27	1.76	12.8 ± 0.18	0.0041
1-cycle w/o H_2O_2	11.12	7.87	140.2	-55.55 ± 0.69	0.43	5.35 ± 0.10	0.0024
1-cycle	12.72	13.75	280.2	-58.96 ± 0.85	0.97	5.63 ± 0.17	0.0052
2-cycle	13.21	11.91	252.1	-59.14 ± 0.75	0.88	4.65 ± 0.13	0.0057
4-cycle	10.16	9.86	160.5	-67.83 ± 0.62	0.74	3.25 ± 0.08	0.0068
6-cycle	9.82	8.81	138.9	-72.17 ± 0.91	0.72	2.36 ± 0.11	0.0092

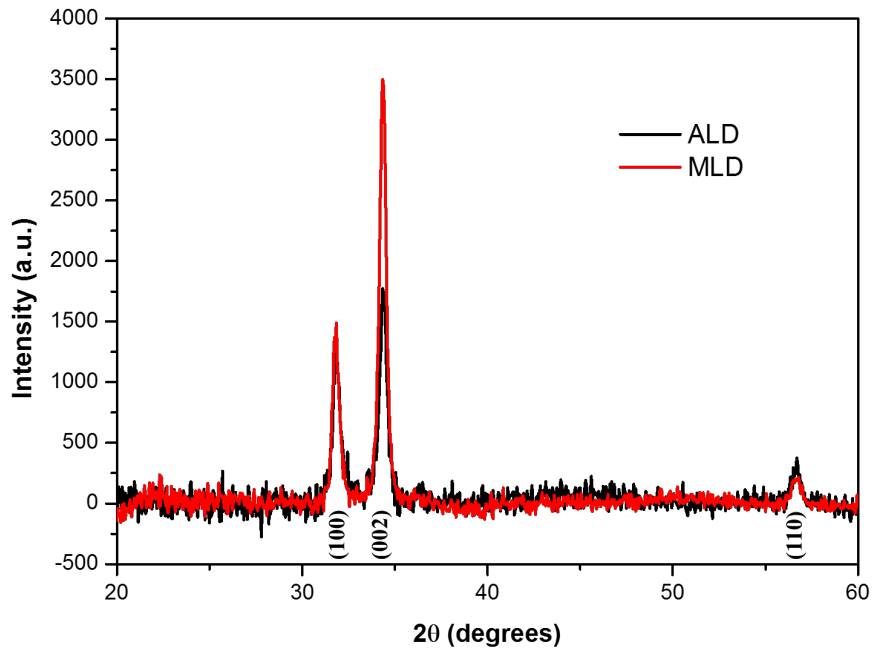


Figure 4.8: The XRD patterns of ZnO deposited by ALD and MLD systems.

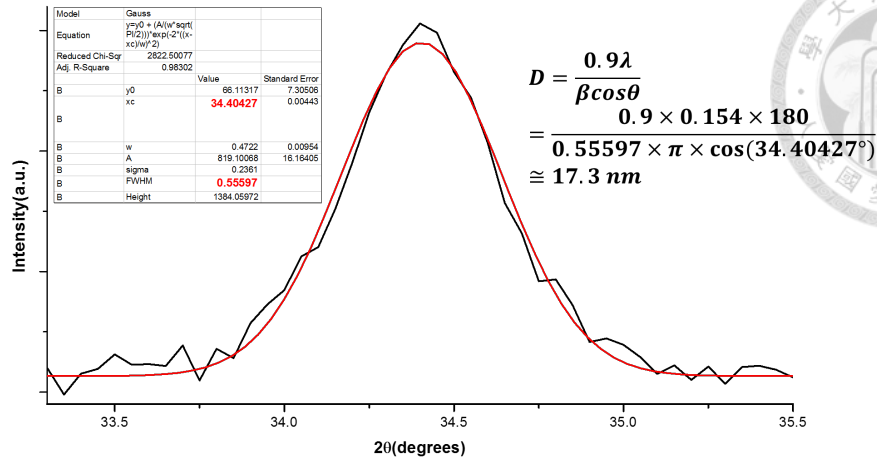


Figure 4.9: The mean grain size calculation of mix 19:1 HZO by Scherrer equation.

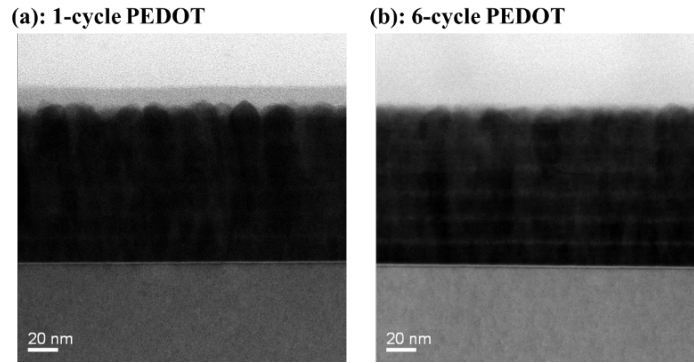


Figure 4.10: The cross-sectional TEM images of HZO/PEDOT superlattices with (a) 1-cycle; (b) 6-cycle inserted PEDOT.

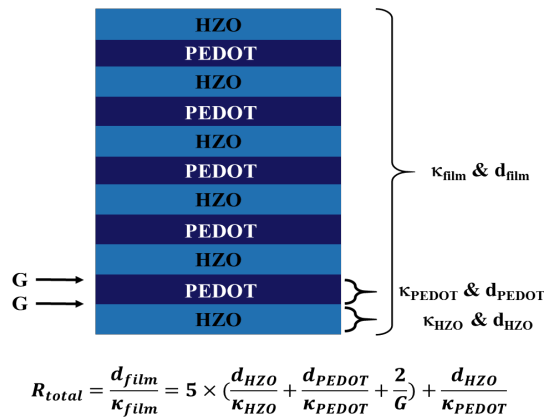


Figure 4.11: The schematic illustration of superlattice-structure and series-resistance model in our calculation.

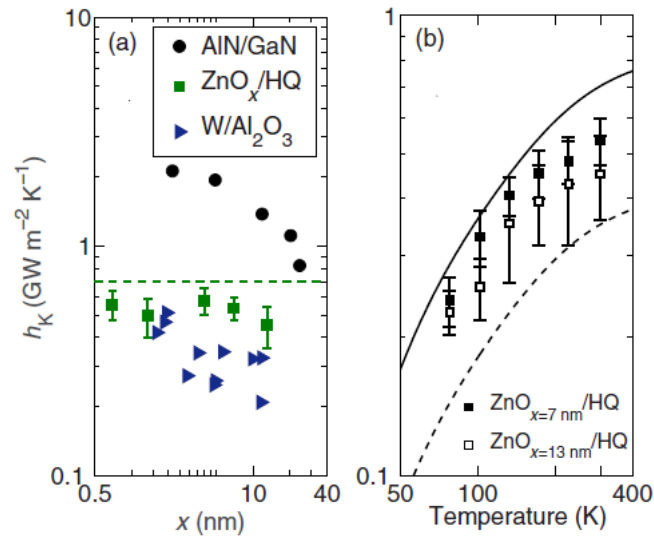


Figure 4.12: The estimated interface thermal conductance in ZnO/hydroquinone/ZnO superlattice done by Ashutosh Giri et al.

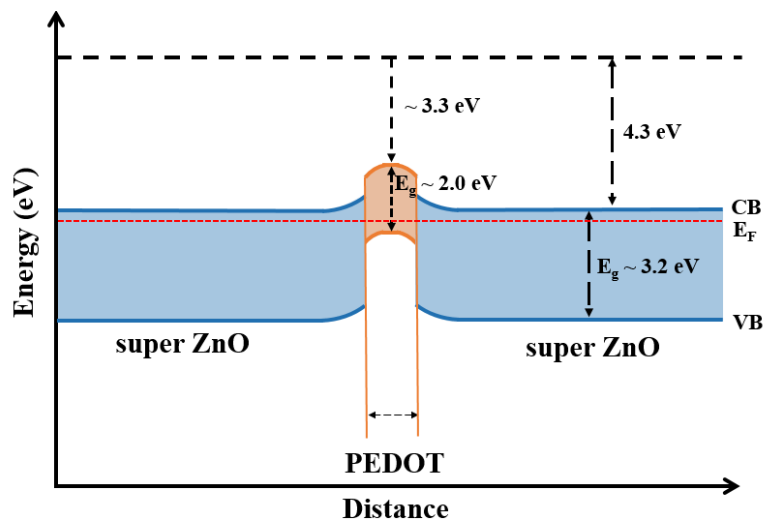


Figure 4.13: The schematic illustration of energy band alignment of PEDOT and ZnO.




4.2 Polyaniline

In the development of depositing polyaniline thin films, two oxidants had been utilized to deposit polyaniline, one was VOCl_3 and the other was SbCl_5 . In both cases, polyaniline thin films had been successfully deposited on silicon wafers and glass substrates at 150°C .

Referring to VOCl_3 system, aniline was heated to 55°C to obtain sufficient concentration of molecules initially. However, the deposited films were only near 12 nm which were hard to conduct analyses. For address this issue, we elevated the temperature of aniline to 65°C for acquiring more vapor phase molecules; besides, the exposure time of each precursor was prolonged from 3s to 5s for increasing reaction probability. Although the growth rate indeed rose from 0.012 nm/cycle to 0.016 nm/cycle, the deposited films were still too thin to analyze and use practically. We attributed the low growth rate to the low concentration of physisorbed and/or chemisorbed VOCl_3 on the surface of substrate at 150°C owing to the highly volatile characteristic of VOCl_3 . Thus, it reduced the frequency of effective collision between VOCl_3 and aniline

Considering increasing the physisorbed and/or chemisorbed oxidants, we selected a new oxidant, SbCl_5 , whose condensability was higher than that of VOCl_3 , i.e. boiling points are 175°C and 126°C for SbCl_5 and VOCl_3 , respectively, to deposit polyaniline



films. In this experiment, we set the temperature of SbCl_5 at 75°C , 85°C and 95°C to obtain three different amounts of vapor phase oxidant molecules. It turned out that the growth rate rose as the temperature of SbCl_5 increased, and the growth rate of each is listed in Table 4.6. For further analyze deposited polyaniline thin films, we decided to set the temperature of SbCl_5 at 95°C , at which the growth rate was the highest, to deposit films with adequate thickness on silicon wafers and glass substrates. The photograph of ~ 15 and $\sim 30\text{nm}$ polyaniline thin films on glass substrates is shown in Figure 4.14. As for Figure 4.15, it is the FTIR spectrum of $\sim 30\text{nm}$ polyaniline on silicon wafer. Although, some peaks in FTIR couldn't be identified, the FTIR spectrum confirmed the formation of polyaniline, and especially the quinoid and benzenoid peaks in FTIR revealed the formation of conjugated chain which are at 1577 and 1490 cm^{-1} , respectively.

To sum up, we successfully demonstrated the deposition of polyaniline via MLD technique, the growth rate was quite low which reduced the practicability; moreover, the deposited films were insulated, which might be originated by the unfavorable oxidant/monomer ratio. Therefore, polyaniline deposited by MLD technique couldn't be used in developing metal oxide/polymer superlattice thermoelectric materials.

Table 4.6: The relevance of polyaniline growth rate on the temperature of SbCl₅.

SbCl ₅ temperature(°C)	Thickness (nm)	Growth rate (nm / cycle)
75	12.9	0.013
85	24.6	0.025
95	28.8	0.029

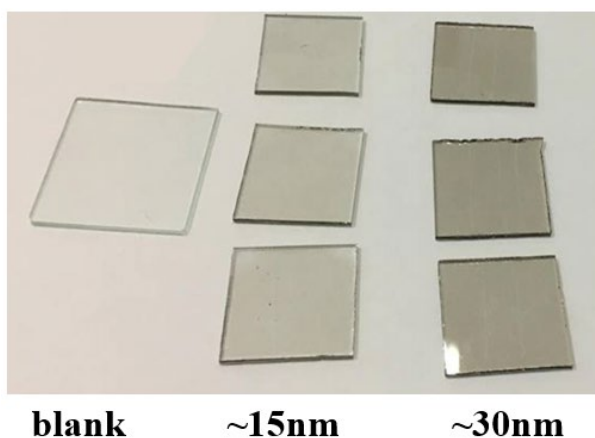


Figure 4.14: The photograph of 15 and 30nm polyaniline thin films on glass substrates.

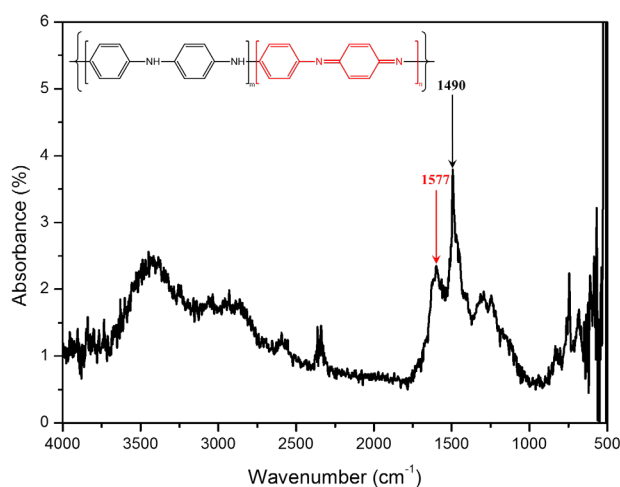


Figure 4.15: The FTIR spectrum of ~30nm polyaniline.

4.3 Polythiophene



In the beginning, we set the deposition temperature at 150°C to match up the ALD ZnO/doped ZnO deposition process, but nothing formed even the deposition cycles

were increased to 1000 cycles. Since Lau et al. stated that 5°C is the optimized deposition temperature in their oCVD system with the same precursors as ours, and an increase in substrate temperature by 2°C significantly reduces the deposition rate⁹⁴.

Based on this contention, we lowered the deposition temperature to increase the growth rate and the temperature was set at 60°C, which is the lower limit temperature for our system, to prevent contamination. Nonetheless, we still failed to deposit polythiophene films. For clarifying the origin of failure, in-situ QCM was utilized to monitor the growth of polythiophene. In this experiment, we dosed thiophene twice in one cycle to increase the reaction probability, i.e. $\text{VOCl}_3 \rightarrow \text{thiophene} \rightarrow \text{thiophene}$, and then repeated this sequence. Figure 4.16:6(a) shows that VOCl_3 molecules were able to physisorb onto the surface of QCM, but the number of physisorbed molecules decreased over time since the N_2 flow purged the surface of QCM. On the other hand, the downward peaks appeared as thiophene was introduced into reaction chamber and then returned to the desorption patterns of VOCl_3 , which can be seen in Figure 4.16:6(b). We assumed that the results might refer to the evidence of no chemisorption even physisorption of thiophene molecules onto the surface of VOCl_3 , and the downward peaks came from the

response of QCM to the pressure and/or temperature fluctuation while dosing thiophene molecule. To verify this supposition, we increased the flow rate of N₂ transiently to mimic the pulse of thiophene. Figure 4.16:6(c) reveals the downward peaks indeed represented the pressure and/or temperature fluctuation during process. In conclusion, we thought that the extremely volatile characteristic of thiophene, i.e. vapor pressure is ~150 mmHg at room temperature, was unfavorable to deposit polythiophene in our system.

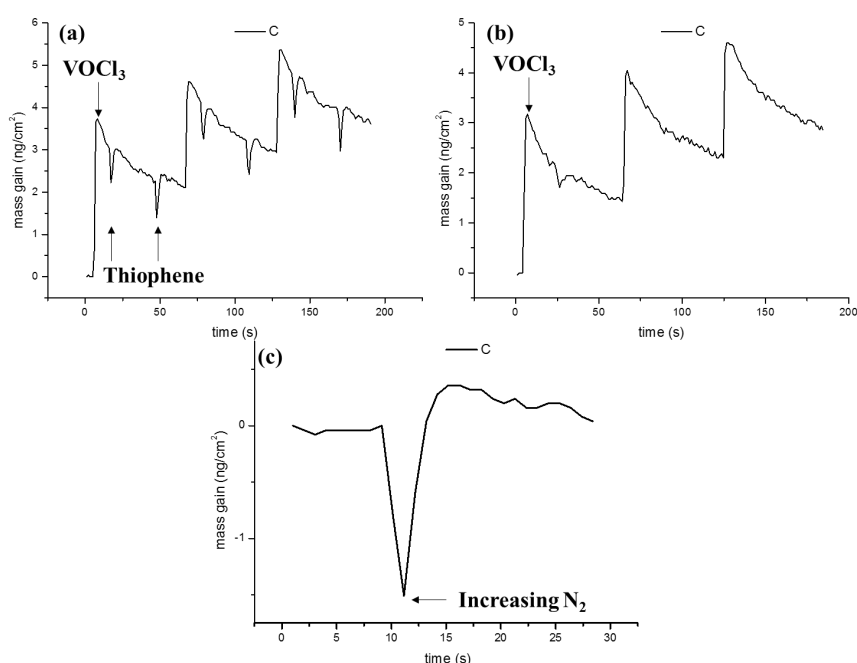



Figure 4.16: The in-situ QCM results (a) deposition of polythiophene while pulsing thiophene twice; (b) pulse VOCl₃ alone; (c) increasing N₂ flow rate transiently.

4.4 Summary



In this chapter, we investigated the deposition of conducting polymers through MLD technique, in which two conducting polymers, i.e. polyaniline and PEDOT, were successfully deposited. Especially, PEDOT showed a relatively high deposition rate (growth rate), 0.3 nm/cycle. It ensured the practicability of this MLD process to deposit PEDOT films in any thickness. Furthermore, the electrical conductivity of our PEDOT films were over 400 S cm^{-1} , which can compete with those synthesized by traditional solution process. These two merits ensured the practicability of MLD-deposited PEDOT in a variety of applications and researches. Moreover, the thermal conductivity of PEDOT was extremely low, only $0.19 \text{ W m}^{-1} \text{ K}^{-1}$, so it was able to provide a considerable thermal resistance in the following research, the thermoelectric performance of metal oxide (HZO) / polymer (PEDOT) superlattices.

Next, the interface-engineering was explored to integrate ALD-HZO and MLD-PEDOT processes to deposit HZO/PEDOT superlattice. In this part, the growth mechanism of PEDOT on the surface of ZnO was studied to ensure the growth of PEDOT under few cycles of deposition. Besides, the modification of PEDOT/ZnO interfaces was implemented to improve the growth of incoming ZnO (HZO). Overall, after conducting interface-engineering, the mass gain of the first-cycle ZnO on the surface of PEDOT was enhanced by a factor of 4 and the electrical conductivity of

deposited superlattice was increased from 39.4 S cm^{-1} to 280.2 S cm^{-1} .

Lastly, the thermoelectric properties of HZO/PEDOT superlattices were studied.

Regarding thermal conductivity, although the complete organic/inorganic interface might not form in any of the tested structures based on our modeling, the thermal conductivity was reduced intensely due to the considerable interface thermal resistances (two interfaces and intrinsic thermal resistance) provided by the inserted PEDOT layers. Besides, the insertion of PEDOT could increase the absolute value of Seebeck coefficient due to energy filtering effect. The increased absolute value of Seebeck coefficient was able to compensate the loss in the electrical conductivity. After testing various periodicities and thicknesses of inserted PEDOT, the optimal structure of superlattice was determined to be alternating 4 periods of mix 19:1 HZO and 6 cycles of PEDOT, and the maximum improvement in ZT was about $\sim 700\%$ over that of the undoped ZnO.

Chapter 5


Long-term stable gas barrier



As described in section 1.8.4, the superlattice-based gas barriers developed by our group before suffered from a poor long-term stability due to the hydrolytic reaction of PA32 in the superlattice. Hence, the depositions of several anti-hydrolysis polymers were developed to act as the substituents in the superlattice-based gas barriers. In our research, the depositions of two polyamides were demonstrated successfully, and thus the discussion on the depositions of polyamides and gas barrier performance of HfO₂/polyamide superlattice were stated first. After that, the discussion of the deposition of polyester, which we also attempt to develop, were stated.

5.1 The deposition of polyamide

Three sets of precursors, MC with piperazine, MC with 1,8-diaminooctane and terephthaloyl chloride with ED, were examined for depositing polyamide films. The structure of precursors, polymers and deposition temperatures are summarized in Table 5.1. As for the temperature precursors and deposition parameters, they are listed in section 2.1.5.



First, the QCM results by the usage of MC and piperazine are shown in Figure 5.1. At 100°C. The mass gain was unstable and small, which can be observed in Figure 5.1 (a). Enlightening from the deposition of polyesters, we suspected that the mass gain might result from the self-condensation of MC monomers only. Thus, the deposition temperature was elevated to 120°C to promote the reactivity between precursors. It is worthy of note that the exposure of MC and piperazine were introduced and set at 10 seconds; besides, to remove redundant precursors and byproducts, the purge times of MC and piperazine were prolonged to 40 and 150 seconds, respectively,. However, the mass gain reduced obviously, which can be seen in Figure 5.1 (b). The results indicate that the mass gain at 100°C was attributed to physisorption of piperazine and self-condensation of MC. On the other hand, the mass gain at 120°C was due to self-condensation of MC mostly since the physisorption was suppressed at elevated temperature even with the exposure of piperazine monomers. Therefore, we failed to deposit polyamide films by the usage of MC and piperazine.

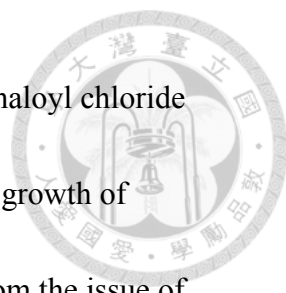
Next, the result of the combination of MC with 1,8-diaminooctane is discussed. It is noteworthy that the extremely long purge times utilized in this process did not dedicate to remove redundant precursors and byproducts as usual; instead, long purge times were considered as the waiting time for acquiring sufficient vapor-phase 1,8-diaminooctane molecules due to its low evaporation rate. As shown in Figure 5.2 (a),

which is the QCM result at 120°C deposition temperature, the mass gain also decreased with deposition cycles, hence the termination reaction still existed in this process.

However, the value of mass gain was quite larger than that in previous works, i.e.

polyester and polyamide by MC and piperazine, which suggested the growth of polyamide by the usage of MC and 1,8-diaminooctane. To avoid the occurrence of termination, we lowered the deposition temperature to 100°C to suppress the mobility and flexibility of 1,8-diaminooctane molecules and further prevent the double reaction. As a consequence, the QCM results in Figure 5.2 (b) and Figure 5.3 show that the mass gain was raised and much steadier even the deposition-cycle was over 100. In fact, the polyamide films, which were about 20 nm in thickness, were obtained after 100-cycle deposition; namely, the growth rate of this process was around 0.2 nm/cycle at 100°C. Besides, the FTIR spectrum of the deposited film, which is shown in Figure 5.4, confirmed the formation of polyamide in this MLD process.

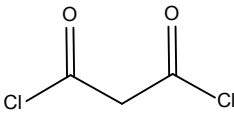
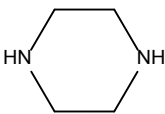
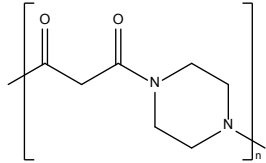
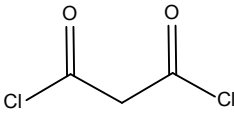

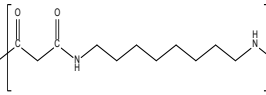
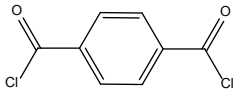
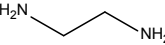
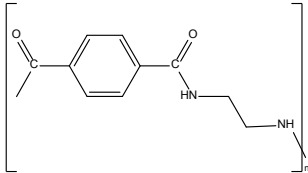
Last, the result of the third set of precursors, terephthaloyl chloride with ED, is stated below. In the QCM result, which is presented in Figure 5.5, it could be observed that the mass gain decreased with the deposition cycle but it was still considerable. To rule out the self-condensation of each precursor, the multiple pulse of single precursor, i.e. pulse terephthaloyl chloride or ED on the surface of each other repeatedly, was carried out. In Figure 5.6, two facts are concluded, one is that self-condensation of ED



molecules is absent; the other is that the self-condensation of terephthaloyl chloride exists but not obvious. With the above results, we concluded that the growth of polyamide by the usage of terephthaloyl chloride and ED suffered from the issue of termination. Thus, the re-nucleation layers, i.e. 2-cycle Al_2O_3 , were inserted for every 10-cycle polyamide to provide new reaction sites for precursors. The QCM result of polyamide with re-nucleation layers is presented in Figure 5.7, in which the mass gain was consistent without any decay; in fact, the thickness of polyamide film after 100-cycle deposition was about 19 nm and the refractive index of obtained film was ~ 1.57 . As previous work, the FTIR spectrum shown in Figure 5.8 was utilized to confirm the growth of polyamide films.

To sum up, in this section, we state the development of anti-hydrolysis polymers, in which two types of polyamide were successfully deposited by MLD technique. For convenience, the polyamide deposited by the usage of MC and 1,8-diaminooctane was named as PA38 (Poly(imino-(1,3-dioxotrimethylene)-iminooctamethylene)), and the other polyamide, whose precursors were terephthaloyl chloride and ED, was called as PAb2 (Poly(imino-carbonyl-1,4-phenylene-carbonyl-iminoethylene)) in the rest dissertation.

Table 5.1: The structure of precursors, polymers and deposition temperatures in the deposition of polyamides.

	Deposition temperature	Precursor (dichloride)	Precursor (diamine)	Polymer
Type 1	100/120 °C			
Type 2	100/120 °C			
Type 3	120 °C			

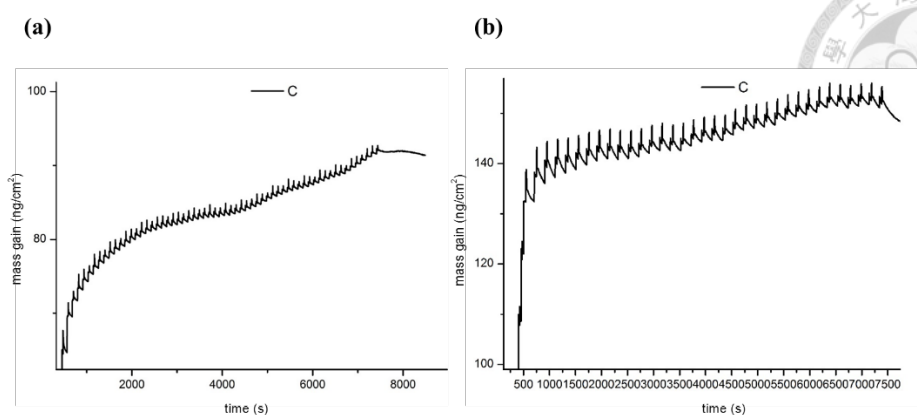


Figure 5.1: The QCM results by the usage of MC and piperazine in deposition of polyamide at varied deposition temperature (a) 100°C; (b) 120°C.

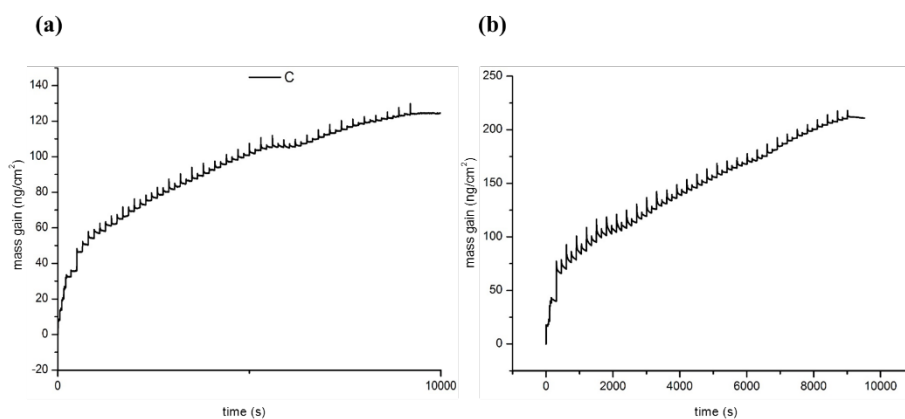


Figure 5.2: The QCM results by the usage of MC and 1,8-diaminooctane in deposition of polyamide at varied deposition temperature (a) 120°C; (b) 100°C.

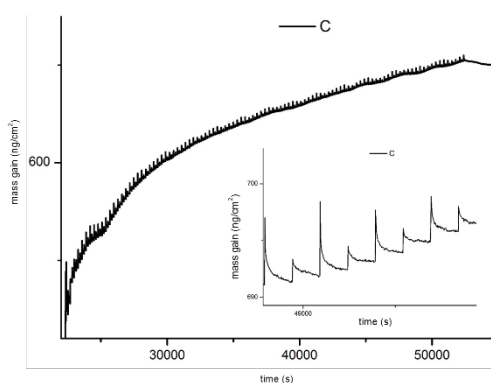


Figure 5.3: The QCM results of 100-cycle polyamide deposited by the usage of MC and 1,8-diaminooctane at 100°C. The inset is the zoom-in of the mass gain at latter cycles.

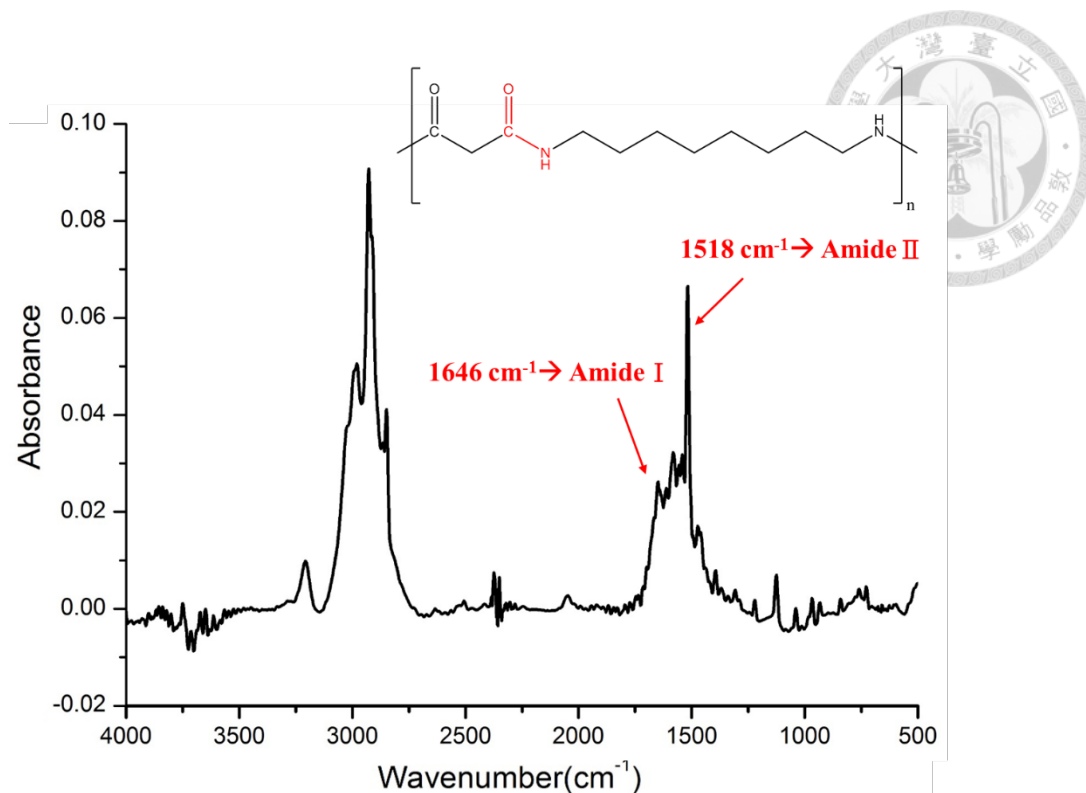


Figure 5.4: The FTIR spectrum of polyamide deposited by the usage of MC and 1,8-diaminooctane.

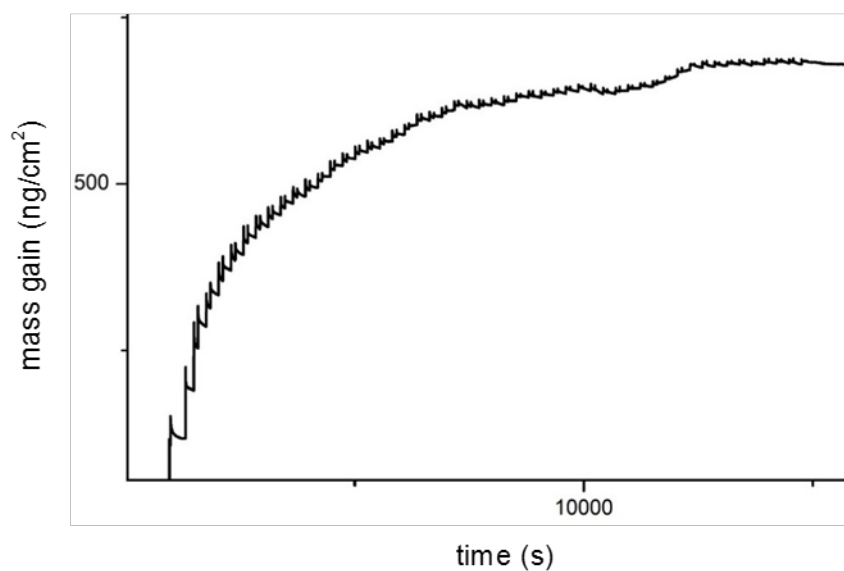


Figure 5.5: The QCM result by the usage of terephthaloyl chloride and ED in deposition of polyamide at 120°C.

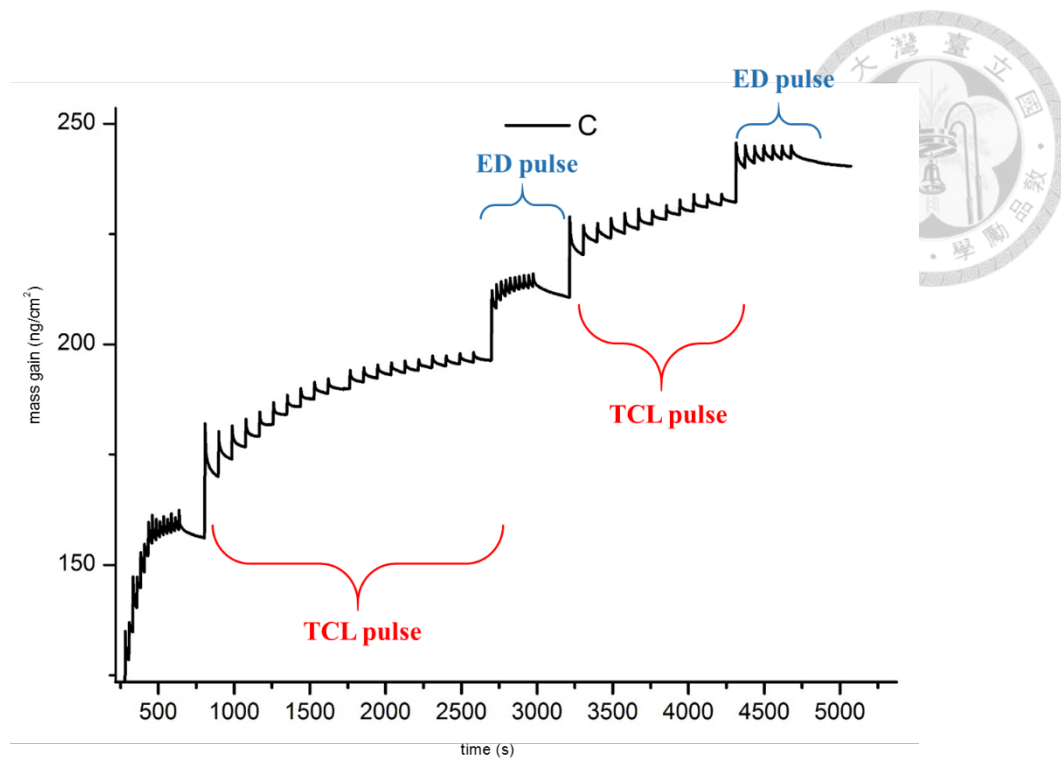


Figure 5.6: The QCM result of the multiple pulse of single precursor.

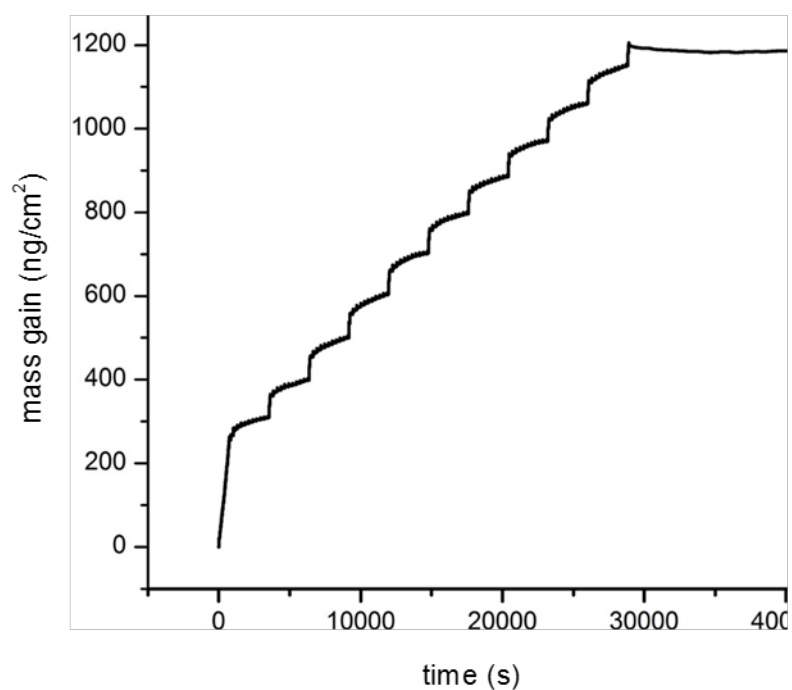


Figure 5.7: The QCM result of polyamide by the usage of terephthaloyl chloride and ED with re-nucleation layers.

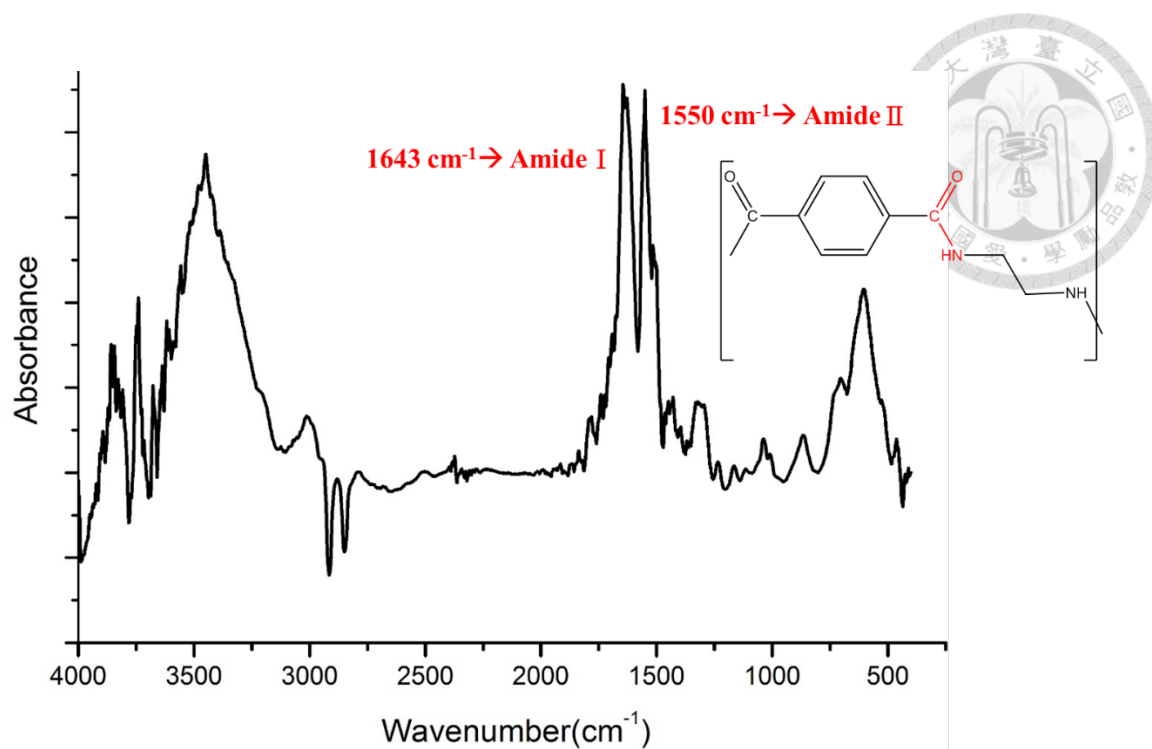


Figure 5.8: The FTIR spectrum of polyamide deposited by the usage of terephthaloyl chloride and ED.


5.2 The gas barrier performance of polyamide and HfO₂/polyamide superlattice



In this section, the performance of gas barrier composed of alternating HfO₂ and anti-hydrolysis polymer is demonstrated. Although two types of polyamides were successfully deposited, i.e. PA38 and PAb2, only PAb2 was selected in the demonstration since the extremely long process time limited the practicality of PA38 in the deposition of superlattice-based gas barrier.

First, the anti-hydrolysis performance of PAb2 was examined. In this experiment, 10 nm of PAb2 and PA32, which was also developed by our group and deposited by the usage of MC and ED as precursors, were deposited on the PI substrates to conduct the damp-test (85°C, 85%RH, 36 hours), and the HeTR of samples (PAb2, PA32 and PI substrate) before and after damp-test are summarized in Table 5.2. In the results, the increasing HeTR of deposited polymer films was mainly attributed to the hydrolysis and/or swelling of our MLD-deposited polymer films since the HeTR of the blank PI substrate was almost unchanged. In the comparison between PAb2 and PA32, the increment of PAb2 was less than that of PA32, which confirmed the improved stability of PAb2 under damp condition.

As for the performance of superlattice-based gas barrier, the structure was designed as alternating 20 cycles of HfO₂ with 20 cycles of polymer and repeating 9 times, in



which the thickness of each layers was based on the optimal structure developed by our previous work done by Ming-Hung Tseng, Ph.D.; however, repeating-time was set arbitrarily on this front. It is noteworthy that the deposition settings of PAb2 were modified to achieve high uniformity, i.e. multiple pulse (2 times) of terephthaloyl chloride and 25 s exposure of each step, the results are also listed Table 5.2. After modification, the variation in the measured HeTR of deposited gas barriers in the same batch was substantially reduced.

Regarding the WVTR, the lower WVTR of HfO₂/PAb2 superlattice-based gas barrier compared with HfO₂/PA32 indicated that the usage of PAb2 prevented the hydrolysis/swelling of polymers and then slowed down the collapse of the superlattice due to the anti-hydrolysis property even the WVTR test was implemented under 100% RH condition. Thus, the gas barrier performance was maintained. Based on this result, it verified our concept that the superlattice-based gas barrier, which contained anti-hydrolysis polymer, exhibited an enhanced long-term stability. Hence, the structure of superlattice, including the thickness of each layer and repeating times, could be further optimized to reduce the WVTR to realize the goal of long-term stable gas barrier for versatile electronics.

Table 5.2: HeTR of varied samples before/after damp-test (85°C, 85%RH, 36 hours)

and WVTR of superlattice-based gas barrier. The unit of HeTR and WVTR is cc day^{-1}

m^{-2} and $\text{g day}^{-1} \text{m}^{-2}$, respectively.

	Before	After	WVTR
PI substrate	2000	2000	22.1
PA32	98	320	N/A
PAb2	103	227	N/A
HfO ₂ /PAb2	2.56~19.82	N/A	N/A
without modification			
HfO ₂ /PAb2	2.26	N/A	5.8
with modification			
HfO ₂ /PA32	2.09	N/A	12.7

5.3 The deposition of polyester



To monitor the growth of polyester with the usage of MC and EG as precursors, QCM analyses were utilized in the development of depositing polyester films. First, we set the temperature of reaction chamber at 150°C arbitrarily. The QCM results of varied pulse time of EG are presented in Figure 5.9, in which it could be discovered that the growth of polyester slowed down rapidly after the initial cycles regardless of the pulse time of EG. To clarify the growth mechanism, we elevated the temperature of chamber from 150°C to 180°C to exclude the probability of lack of reactivity between MC and EG. The QCM result is shown in Figure 5.10. Unfortunately, the growth still terminated rapidly. Therefore, the result might indicate the termination of MLD-deposited polyester since the flexible backbones of MC and EG molecules enabled the occurrence of double reaction, whose schematic illustration is presented in Figure 5.11¹⁰⁸; thus, subsequent monomers had fewer reaction sites with which they can react gradually. As for the minute quantity of mass gain at latter cycles, it might result from the renucleation process due to the physisorbed precursors and/or the self-condensation of MC monomers. The reaction mechanism of the self-condensation of MC monomers is shown in Figure 5.12.¹⁰⁹ In conclusion, we thought the growth of polyester with MC and EG as precursors was hard to fulfill by MLD technique.

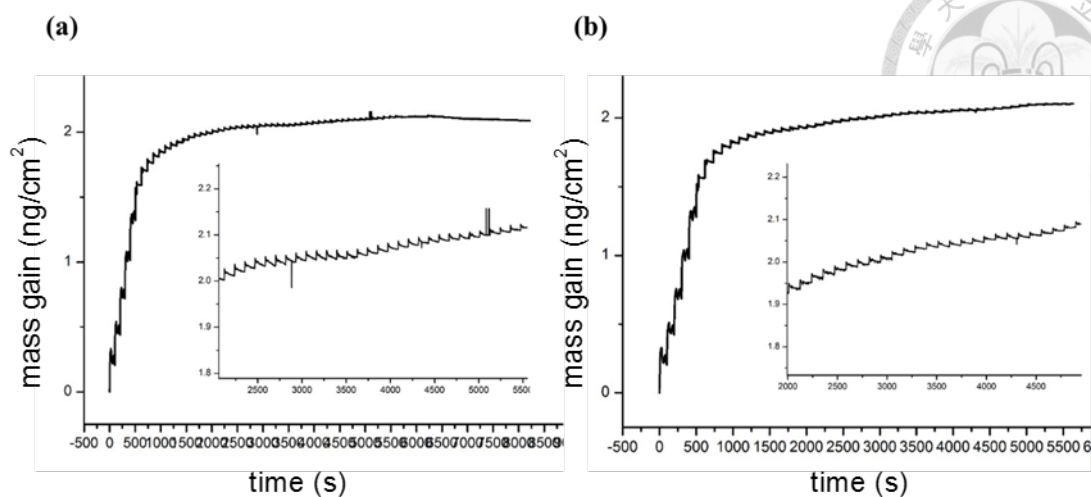


Figure 5.9: The QCM results of varied pulse time of EG (a) 0.02 s; (b) 0.10 s. The insets are the mass gain at latter cycles.

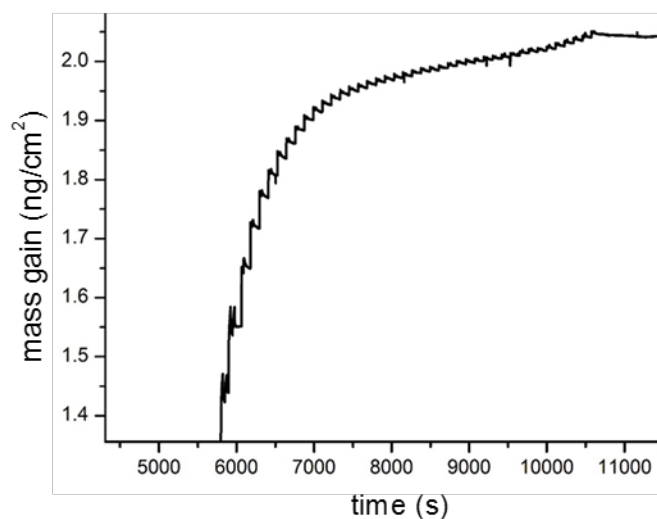


Figure 5.10: The QCM result of polyester at 180°C with 0.02 s pulse of EG.

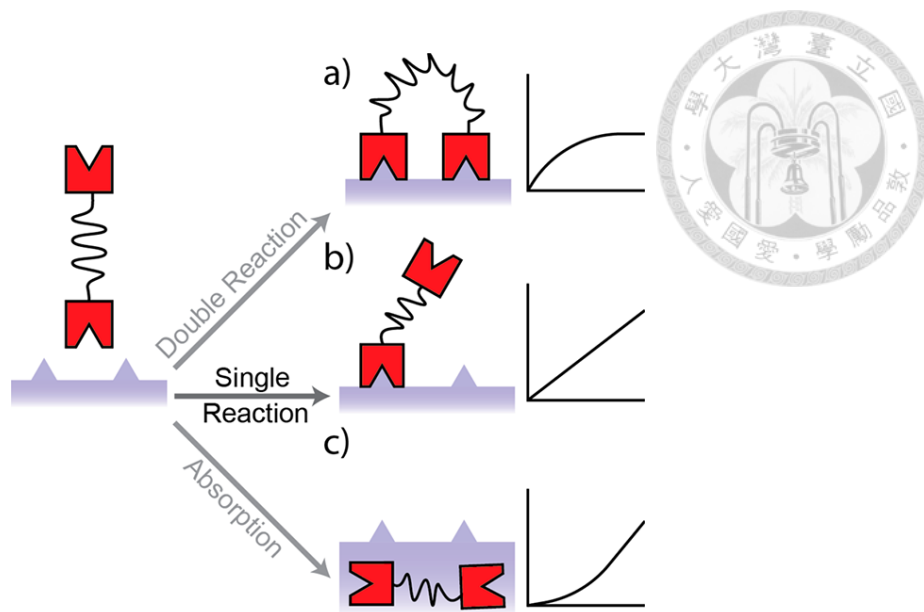


Figure 5.11: The schematic illustration of single and double reaction in MLD.

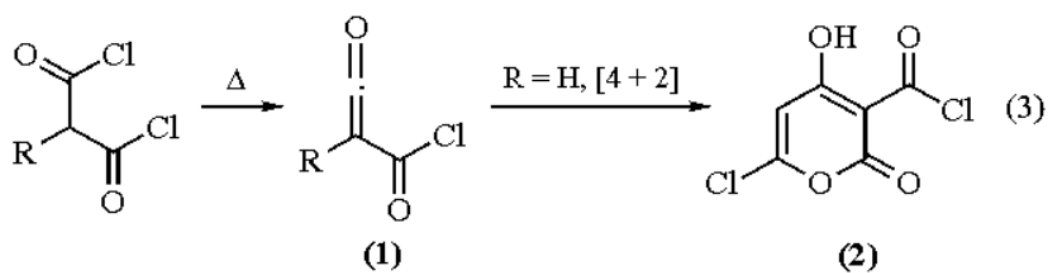



Figure 5.12: The reaction mechanism of the self-condensation of MC monomers.

5.4 Summary



In this chapter, we aimed to develop a long-term stable gas barrier by depositing the superlattice composed of HfO_2 and anti-hydrolysis polymer. Thus, the study started with the development of anti-hydrolysis polymers deposition by MLD technique, in which one polyester and three types of polyamides were tested. Luckily, the depositions of two polyamides by MLD were successfully demonstrated, i.e. PA38 and PAb2. Between these two polyamides, only PAb2 was selected as the basis material in the deposition of superlattice-based gas barrier with HfO_2 due to its shorter process time. As a result, both the pure PAb2 films and the HfO_2 /PAb2 superlattice showed an enhanced long-term stability under humid condition in comparison with the property of PA32 and HfO_2 /PA32 superlattice. Therefore, the concept of promoting the long-term stability of superlattice-based gas barrier by the usage of anti-hydrolysis polymer as basis material was verified.

Chapter 6



Conclusions

In this dissertation, the development of superlattice-based thin films deposited by ALD was studied. In the first part, we focused on the enhancing ZT of the inorganic superlattice thermoelectric material. We have explored the roles of dopants as both carrier-inducing and phonon-scattering components in metal oxide superlattice. We determined that the heavier elements with similar ionic radii to the cation in the host metal were the better doping ions. Because they produced the great mass difference to impede the transportation of phonons while preserving the crystallinity to maintain high electrical mobility. Besides, optimization of the thermoelectric performance by using a combination of the conventional and mixed ALD doping processes had the benefits of the heat blocking from the conventional process and the excellent electrical properties from the mixed process. After systematic investigation, we concluded that the superlattice, which was composed of two periods of mix 24:1 and 7-cycle conventional HfO_2 , possessed the optimal performance, i.e. about 13-fold enhancement on ZT compared to undoped ZnO .

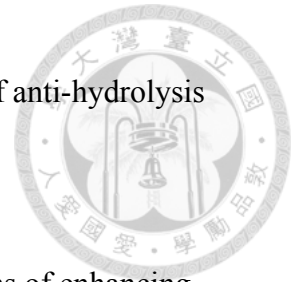
We also investigated the effects of introducing the ^{18}O isotope into the Hf-doped

ZnO (HZO) on its thermoelectric performance experimentally for the first time. We determined that the optimal pattern of ^{18}O distribution was alternating 4.5 nm of ^{18}O -containing HZO layer with 4.5 nm of ^{16}O -containing one, resulting in a 20% further increase in ZT.

In the second part, we started with the exploration of the deposition of conducting polymers via MLD technique, in which the depositions of polyaniline and PEDOT were successfully demonstrated. After that, PEDOT was selected as basis material in the deposition of novel ALD metal oxide/polymer superlattice films. In this research, the unique inorganic/organic interfaces provided following merits to further increase the thermoelectric performance of superlattice-based materials, such as increasing interfacial scattering of phonons, improving the electrical carrier filtering and offset electrical DOS symmetry via band distortion. After testing various periodicities and thicknesses of inserted PEDOT, the optimal structure of superlattice was determined as alternating 4 periods of mix 19:1 HZO and 6 cycles of PEDOT, and the maximum improvement in ZT was about ~700% over that of the undoped ZnO.

In the last part, another application of superlattice-based material deposited by ALD was verified. In the research of long-term stable gas barrier, the anti-hydrolysis polymers were deposited. As a result, both the pure PAb2 films and the $\text{HfO}_2/\text{PAb2}$ superlattice showed an enhanced long-term stability under humid condition. Therefore,

the concept of the promoting gas barrier performance by the usage of anti-hydrolysis polymer as basis material was confirmed by this research.




Through this dissertation, we aim to investigate the mechanisms of enhancing thermoelectric performance of superlattice-based materials, which are also applicable to the development of other types of ALD TE films. Furthermore, we also intend to explore and verify the variety of application of ALD-deposited superlattice materials.

Reference



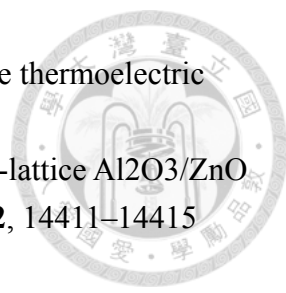
1. Chapter 6 — Innovating Clean Energy Technologies in Advanced Manufacturing | Department of Energy. <https://energy.gov/under-secretary-science-and-energy/downloads/chapter-6-innovating-clean-energy-technologies-advanced>.
2. Sootsman, J. R., Chung, D. Y. & Kanatzidis, M. G. New and Old Concepts in Thermoelectric Materials. *Angewandte Chemie International Edition* **48**, 8616–8639 (2009).
3. Seebeck, T. J. Ueber die magnetische Polarisation der Metalle und Erze durch Temperaturdifferenz. *Annalen der Physik* **82**, 253–286 (1826).
4. Cutler, M. & Mott, N. F. Observation of Anderson Localization in an Electron Gas. *Phys. Rev.* **181**, 1336–1340 (1969).
5. Snyder, G. J. & Toberer, E. S. Complex thermoelectric materials. *Nat Mater* **7**, 105–114 (2008).
6. Kanatzidis, M. G. Nanostructured Thermoelectrics: The New Paradigm?†. *Chem. Mater.* **22**, 648–659 (2010).
7. Zhang, Y. *et al.* Hot Carrier Filtering in Solution Processed Heterostructures: A Paradigm for Improving Thermoelectric Efficiency. *Adv. Mater.* **26**, 2755–2761 (2014).
8. Li, J.-F., Liu, W.-S., Zhao, L.-D. & Zhou, M. High-performance nanostructured thermoelectric materials. *NPG Asia Mater* **2**, 152–158 (2010).
9. Zhao, L.-D. *et al.* Thermoelectrics with Earth Abundant Elements: High Performance p-type PbS Nanostructured with SrS and CaS. *J. Am. Chem. Soc.* **134**, 7902–7912 (2012).
10. Johnsen, S. *et al.* Nanostructures Boost the Thermoelectric Performance of PbS. *J. Am. Chem. Soc.* **133**, 3460–3470 (2011).
11. Zhang, K. *et al.* Thermoelectric performance of p-type nanohybrids filled polymer composites. *Nano Energy* **13**, 327–335 (2015).
12. Zhang, S., Li, A. & Sun, K. Thermoelectric properties of Graphene/Mn_{0.7}Zn_{0.3}Fe₂O₄ composites. *Ceramics International* **43**, 8643–8647 (2017).
13. Lee, H. *et al.* Effects of nanoscale porosity on thermoelectric properties of SiGe. *Journal of Applied Physics* **107**, 094308 (2010).
14. Goldsmid, H. J. Porous Thermoelectric Materials. *Materials (Basel)* **2**, 903–910 (2009).
15. Bulat, L. P., Pshenay-Severin, D. A. & Osvenskii, V. B. Effect of porosity on the

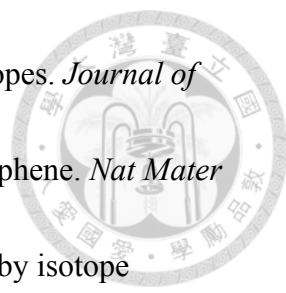
- 
- thermoelectric efficiency of PbTe. *Phys. Solid State* **58**, 1532–1538 (2016).
16. Gu, Y. *et al.* Porosity induced thermoelectric performance optimization for antimony telluride. *Ceramics International* **44**, 21421–21427 (2018).
 17. Chowdhury, I. *et al.* On-chip cooling by superlattice-based thin-film thermoelectrics. *Nat. Nanotechnol.* **4**, 235–238 (2009).
 18. Wan, C. *et al.* Flexible n-type thermoelectric materials by organic intercalation of layered transition metal dichalcogenide TiS₂. *Nature Materials* **14**, 622 (2015).
 19. Martin-Gonzalez, M., Caballero-Calero, O. & Diaz-Chao, P. Nanoengineering thermoelectrics for 21st century: Energy harvesting and other trends in the field. *Renew. Sust. Energ. Rev.* **24**, 288–305 (2013).
 20. Bulman, G. *et al.* Superlattice-based thin-film thermoelectric modules with high cooling fluxes. *Nature Communications* **7**, 10302 (2016).
 21. Harman, T. C., Taylor, P. J., Walsh, M. P. & LaForge, B. E. Quantum Dot Superlattice Thermoelectric Materials and Devices. *Science* **297**, 2229–2232 (2002).
 22. Venkatasubramanian, R. Lattice thermal conductivity reduction and phonon localizationlike behavior in superlattice structures. *Phys. Rev. B* **61**, 3091–3097 (2000).
 23. Nishio, Y. & Hirano, T. Improvement of the Efficiency of Thermoelectric Energy Conversion by Utilizing Potential Barriers. *Jpn. J. Appl. Phys.* **36**, 170 (1997).
 24. Bahk, J.-H., Bian, Z. & Shakouri, A. Electron energy filtering by a nonplanar potential to enhance the thermoelectric power factor in bulk materials. *Phys. Rev. B* **87**, 075204 (2013).
 25. Ko, D.-K., Kang, Y. & Murray, C. B. Enhanced Thermopower via Carrier Energy Filtering in Solution-Processable Pt–Sb₂Te₃ Nanocomposites. *Nano Lett.* **11**, 2841–2844 (2011).
 26. Soni, A. *et al.* Interface Driven Energy Filtering of Thermoelectric Power in Spark Plasma Sintered Bi₂Te_{2.7}Se_{0.3} Nanoplatelet Composites. *Nano Lett.* **12**, 4305–4310 (2012).
 27. Martin, J., Wang, L., Chen, L. & Nolas, G. S. Enhanced Seebeck coefficient through energy-barrier scattering in PbTe nanocomposites. *Phys. Rev. B* **79**, 115311 (2009).
 28. Chen, Z.-G., Shi, X., Zhao, L.-D. & Zou, J. High-performance SnSe thermoelectric materials: Progress and future challenge. *Prog. Mater. Sci.* **97**, 283–346 (2018).
 29. Yang, L., Chen, Z.-G., Dargusch, M. S. & Zou, J. High Performance Thermoelectric Materials: Progress and Their Applications. *Adv. Energy Mater.* **8**, 1701797 (2018).
 30. Bahk, J.-H., Fang, H., Yazawa, K. & Shakouri, A. Flexible thermoelectric materials and device optimization for wearable energy harvesting. *J. Mater. Chem. C* **3**, 10362–10374 (2015).
 31. Zheng, X. F., Liu, C. X., Yan, Y. Y. & Wang, Q. A review of thermoelectrics

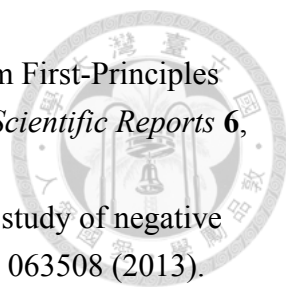
- research - Recent developments and potentials for sustainable and renewable energy applications. *Renew. Sust. Energ. Rev.* **32**, 486–503 (2014).
32. Hochbaum, A. I. *et al.* Enhanced thermoelectric performance of rough silicon nanowires. *Nature* **451**, 163–167 (2008).
 33. Zhang, G. *et al.* Rational Synthesis of Ultrathin n-Type Bi₂Te₃ Nanowires with Enhanced Thermoelectric Properties. *Nano Lett.* **12**, 56–60 (2012).
 34. Liang, L., Chen, G. & Guo, C.-Y. Enhanced thermoelectric performance by self-assembled layered morphology of polypyrrole nanowire/single-walled carbon nanotube composites. *Compos. Sci. Technol.* **129**, 130–136 (2016).
 35. Choi, J., Lee, J. Y., Lee, S.-S., Park, C. R. & Kim, H. High-Performance Thermoelectric Paper Based on Double Carrier-Filtering Processes at Nanowire Heterojunctions. *Adv. Energy Mater.* **6**, 1502181 (2016).
 36. Sothmann, B., Sanchez, R. & Jordan, A. N. Thermoelectric energy harvesting with quantum dots. *Nanotechnology* **26**, 032001 (2015).
 37. Harman, T. C., Taylor, P. J., Spears, D. L. & Walsh, M. P. Thermoelectric quantum-dot superlattices with high ZT. *J. Electron. Mater.* **29**, L1–L4 (2000).
 38. Wang, R. Y. *et al.* Enhanced thermopower in PbSe nanocrystal quantum dot superlattices. *Nano Lett.* **8**, 2283–2288 (2008).
 39. Esposito, M., Lindenberg, K. & Van den Broeck, C. Thermoelectric efficiency at maximum power in a quantum dot. *EPL* **85**, 60010 (2009).
 40. Park, J.-S., Chae, H., Chung, H. K. & Lee, S. I. Thin film encapsulation for flexible AM-OLED: a review. *Semicond. Sci. Technol.* **26**, 034001 (2011).
 41. Hausmann, D. M., Kim, E., Becker, J. & Gordon, R. G. Atomic Layer Deposition of Hafnium and Zirconium Oxides Using Metal Amide Precursors. *Chemistry of Materials* **14**, 4350–4358 (2002).
 42. Wang, X., Tabakman, S. M. & Dai, H. Atomic Layer Deposition of Metal Oxides on Pristine and Functionalized Graphene. *J. Am. Chem. Soc.* **130**, 8152–8153 (2008).
 43. Ritala, M. *et al.* Atomic Layer Deposition of Oxide Thin Films with Metal Alkoxides as Oxygen Sources. *Science* **288**, 319–321 (2000).
 44. Juppo, M., Ritala, M. & Leskelä, M. Use of 1,1-Dimethylhydrazine in the Atomic Layer Deposition of Transition Metal Nitride Thin Films. *J. Electrochem. Soc.* **147**, 3377–3381 (2000).
 45. Becker, J. S. & Gordon, R. G. Diffusion barrier properties of tungsten nitride films grown by atomic layer deposition from bis(tert-butylimido)bis(dimethylamido)tungsten and ammonia. *Appl. Phys. Lett.* **82**, 2239–2241 (2003).
 46. Kim, H. Atomic layer deposition of metal and nitride thin films: Current research efforts and applications for semiconductor device processing. *Journal of Vacuum*

- Science & Technology B: Microelectronics and Nanometer Structures Processing, Measurement, and Phenomena* **21**, 2231–2261 (2003).
47. Dasgupta, N. P., Meng, X., Elam, J. W. & Martinson, A. B. F. Atomic Layer Deposition of Metal Sulfide Materials. *Acc. Chem. Res.* (2015) doi:10.1021/ar500360d.
 48. Dasgupta, N. P. *et al.* Atomic Layer Deposition of Lead Sulfide Quantum Dots on Nanowire Surfaces. *Nano Lett.* **11**, 934–940 (2011).
 49. Lim, B. S., Rahtu, A. & Gordon, R. G. Atomic layer deposition of transition metals. *Nature Materials* **2**, 749–754 (2003).
 50. Adamczyk, N. M., Dameron, A. A. & George, S. M. Molecular Layer Deposition of Poly(p-phenylene terephthalamide) Films Using Terephthaloyl Chloride and p-Phenylenediamine. *Langmuir* **24**, 2081–2089 (2008).
 51. Du, Y. & George, S. M. Molecular Layer Deposition of Nylon 66 Films Examined Using in Situ FTIR Spectroscopy. *J. Phys. Chem. C* **111**, 8509–8517 (2007).
 52. Ivanova, T. V., Maydannik, P. S. & Cameron, D. C. Molecular layer deposition of polyethylene terephthalate thin films. *Journal of Vacuum Science & Technology A* **30**, 01A121 (2012).
 53. Fug, F. *et al.* Molecular layer deposition of polyurethane—Polymerisation at the very contact to native aluminium and copper. *Applied Surface Science* **426**, 133–147 (2017).
 54. Lee, Y., Yoon, B., Cavanagh, A. S. & George, S. M. Molecular Layer Deposition of Aluminum Alkoxide Polymer Films Using Trimethylaluminum and Glycidol. *Langmuir* **27**, 15155–15164 (2011).
 55. Dameron, A. A. *et al.* Molecular Layer Deposition of Alucone Polymer Films Using Trimethylaluminum and Ethylene Glycol. *Chem. Mater.* **20**, 3315–3326 (2008).
 56. Kerckhove, K. V. de *et al.* Molecular layer deposition of “titanicone”, a titanium-based hybrid material, as an electrode for lithium-ion batteries. *Dalton Trans.* **45**, 1176–1184 (2016).
 57. Yoon, B., Lee, B. H. & George, S. M. Highly Conductive and Transparent Hybrid Organic–Inorganic Zincone Thin Films Using Atomic and Molecular Layer Deposition. *J. Phys. Chem. C* **116**, 24784–24791 (2012).
 58. Xiao, W. *et al.* A flexible transparent gas barrier film employing the method of mixing ALD/MLD-grown Al₂O₃ and alucone layers. *Nanoscale Res Lett* **10**, 1–7 (2015).
 59. Lee, B. H., Yoon, B., Anderson, V. R. & George, S. M. Alucone Alloys with Tunable Properties Using Alucone Molecular Layer Deposition and Al₂O₃ Atomic Layer Deposition. *J. Phys. Chem. C* **116**, 3250–3257 (2012).
 60. Liang, X. & Weimer, A. W. An overview of highly porous oxide films with tunable

- thickness prepared by molecular layer deposition. *Current Opinion in Solid State and Materials Science* doi:10.1016/j.cossms.2014.08.002.
61. Liu, J. *et al.* Ultralow Thermal Conductivity of Atomic/Molecular Layer-Deposited Hybrid Organic–Inorganic Zincone Thin Films. *Nano Lett.* **13**, 5594–5599 (2013).
 62. Nminibapiel, D. *et al.* Growth of Nanolaminates of Thermoelectric Bi₂Te₃/Sb₂Te₃ by Atomic Layer Deposition. *ECS J. Solid State Sci. Technol.* **3**, P95–P100 (2014).
 63. Zhang, K. *et al.* Atomic Layer Deposition of Nanolaminate Structures of Alternating PbTe and PbSe Thermoelectric Films. *ECS J. Solid State Sci. Technol.* **3**, P207–P212 (2014).
 64. Sarnet, T. *et al.* Atomic Layer Deposition and Characterization of Bi₂Te₃ Thin Films. *J. Phys. Chem. A* (2014) doi:10.1021/jp5063429.
 65. Mahuli, N., Saha, D. & Sarkar, S. K. Atomic Layer Deposition of p-Type Bi₂S₃. *J. Phys. Chem. C* **121**, 8136–8144 (2017).
 66. Lin, Y.-Y., Hsu, C.-C., Tseng, M.-H., Shyue, J.-J. & Tsai, F.-Y. Stable and High-Performance Flexible ZnO Thin-Film Transistors by Atomic Layer Deposition. *ACS Applied Materials & Interfaces* **7**, 22610–22617 (2015).
 67. Lim, S. J. *et al.* Atomic Layer Deposition ZnO:N Thin Film Transistor: The Effects of N Concentration on the Device Properties. *J. Electrochem. Soc.* **157**, H214–H218 (2010).
 68. Chou, C.-T. *et al.* Transparent Conductive Gas-Permeation Barriers on Plastics by Atomic Layer Deposition. *Adv. Mater.* **25**, 1750–1754 (2013).
 69. Macco, B. *et al.* Atomic layer deposition of high-mobility hydrogen-doped zinc oxide. *Solar Energy Materials and Solar Cells* **173**, 111–119 (2017).
 70. Boyadjiev, S. I., Georgieva, V., Yordanov, R., Raicheva, Z. & Szilágyi, I. M. Preparation and characterization of ALD deposited ZnO thin films studied for gas sensors. *Applied Surface Science* **387**, 1230–1235 (2016).
 71. Lin, P., Chen, X., Zhang, K. & Baumgart, H. Improved Gas Sensing Performance of ALD AZO 3-D Coated ZnO Nanorods. *ECS J. Solid State Sci. Technol.* **7**, Q246–Q252 (2018).
 72. Tseng, Z.-L., Chiang, C.-H. & Wu, C.-G. Surface Engineering of ZnO Thin Film for High Efficiency Planar Perovskite Solar Cells. *Scientific Reports* **5**, 13211 (2015).
 73. Hultqvist, A. *et al.* Atomic Layer Deposition of Electron Selective SnO_x and ZnO Films on Mixed Halide Perovskite: Compatibility and Performance. *ACS Appl. Mater. Interfaces* **9**, 29707–29716 (2017).
 74. Lee, S.-H., Lee, J.-H., Choi, S.-J. & Park, J.-S. Studies of thermoelectric transport properties of atomic layer deposited gallium-doped ZnO. *Ceramics International* **43**, 7784–7788 (2017).
 75. Park, N.-W. *et al.* Control of phonon transport by the formation of the Al₂O₃

- 
- interlayer in Al₂O₃–ZnO superlattice thin films and their in-plane thermoelectric energy generator performance. *Nanoscale* **9**, 7027–7036 (2017).
76. Lee, J.-H. *et al.* Enhancing the thermoelectric properties of super-lattice Al₂O₃/ZnO atomic film via interface confinement. *Ceramics International* **42**, 14411–14415 (2016).
 77. Tynell, T., Yamauchi, H. & Karppinen, M. Hybrid inorganic–organic superlattice structures with atomic layer deposition/molecular layer deposition. *Journal of Vacuum Science & Technology A* **32**, 01A105 (2014).
 78. Tynell, T., Terasaki, I., Yamauchi, H. & Karppinen, M. Thermoelectric characteristics of (Zn,Al)O/hydroquinone superlattices. *J. Mater. Chem. A* **1**, 13619–13624 (2013).
 79. Abdulagatov, A. I. *et al.* Pyrolysis of Titanicene Molecular Layer Deposition Films as Precursors for Conducting TiO₂/Carbon Composite Films. *J. Phys. Chem. C* **117**, 17442–17450 (2013).
 80. Niemelä, J.-P. & Karppinen, M. Tunable optical properties of hybrid inorganic–organic [(TiO₂)_m(Ti–O–C₆H₄–O–)_k]_n superlattice thin films. *Dalton Trans.* **44**, 591–597 (2014).
 81. Lee, B. H., Anderson, V. R. & George, S. M. Growth and Properties of Hafniconene and HfO₂/Hafniconene Nanolaminate and Alloy Films Using Molecular Layer Deposition Techniques. *ACS Appl. Mater. Interfaces* (2014) doi:10.1021/am504341r.
 82. Vasudevan, S. A. *et al.* Controlled release from protein particles encapsulated by molecular layer deposition. *Chem. Commun.* **51**, 12540–12543 (2015).
 83. Nisula, M. & Karppinen, M. Atomic/Molecular Layer Deposition of Lithium Terephthalate Thin Films as High Rate Capability Li-Ion Battery Anodes. *Nano Lett.* **16**, 1276–1281 (2016).
 84. Bergsman, D. S. *et al.* Structurally Stable Manganese Alkoxide Films Grown by Hybrid Molecular Layer Deposition for Electrochemical Applications. *Advanced Functional Materials* **29**, 1904129 (2019).
 85. Wu, S., Wang, Z., Xiong, S. & Wang, Y. Tailoring TiO₂ membranes for nanofiltration and tight ultrafiltration by leveraging molecular layer deposition and crystallization. *Journal of Membrane Science* **578**, 149–155 (2019).
 86. Liang, X., Yu, M., Li, J., Jiang, Y.-B. & Weimer, A. W. Ultra-thin microporous–mesoporous metal oxide films prepared by molecular layer deposition (MLD). *Chem. Commun.* 7140–7142 (2009) doi:10.1039/B911888H.
 87. Liang, X. *et al.* Ultrathin highly porous alumina films prepared by alucone ABC molecular layer deposition (MLD). *Microporous and Mesoporous Materials* **168**, 178–182 (2013).

- 
88. Surla, V. *et al.* Seebeck coefficient measurements of lithium isotopes. *Journal of Nuclear Materials* **415**, 18–22 (2011).
 89. Chen, S. *et al.* Thermal conductivity of isotopically modified graphene. *Nat Mater* **11**, 203–207 (2012).
 90. Royo, M. & Rurali, R. Tuning thermal transport in Si nanowires by isotope engineering. *Phys. Chem. Chem. Phys.* **18**, 26262–26267 (2016).
 91. Mukherjee, S. *et al.* Reduction of Thermal Conductivity in Nanowires by Combined Engineering of Crystal Phase and Isotope Disorder. *Nano Lett.* **18**, 3066–3075 (2018).
 92. Bhattacharyya, D., Howden, R. M., Borrelli, D. C. & Gleason, K. K. Vapor phase oxidative synthesis of conjugated polymers and applications. *J. Polym. Sci. B Polym. Phys.* **50**, 1329–1351 (2012).
 93. Im, S. G. & Gleason, K. K. Systematic Control of the Electrical Conductivity of Poly(3,4-ethylenedioxythiophene) via Oxidative Chemical Vapor Deposition. *Macromolecules* **40**, 6552–6556 (2007).
 94. Nejati, S. & Lau, K. K. S. Chemical Vapor Deposition Synthesis of Tunable Unsubstituted Polythiophene. *Langmuir* **27**, 15223–15229 (2011).
 95. Atanasov, S. E. *et al.* Highly Conductive and Conformal Poly(3,4-ethylenedioxythiophene) (PEDOT) Thin Films via Oxidative Molecular Layer Deposition. *Chem. Mater.* **26**, 3471–3478 (2014).
 96. Cahill, D. G. Analysis of heat flow in layered structures for time-domain thermoreflectance. *Review of Scientific Instruments* **75**, 5119–5122 (2004).
 97. Yuan, H. *et al.* Atomic layer deposition of Al-doped ZnO films using ozone as the oxygen source: A comparison of two methods to deliver aluminum. *Journal of Vacuum Science & Technology A* **30**, 01A138 (2011).
 98. Lee, D.-J. *et al.* Structural and Electrical Properties of Atomic Layer Deposited Al-Doped ZnO Films. *Advanced Functional Materials* **21**, 448–455 (2011).
 99. Jin, C., Liu, B., Lei, Z. & Sun, J. Structure and photoluminescence of the TiO₂ films grown by atomic layer deposition using tetrakis-dimethylamino titanium and ozone. *Nanoscale Res Lett* **10**, (2015).
 100. Karttunen, A. J., Tynell, T. & Karppinen, M. Layer-by-layer design of nanostructured thermoelectrics: First-principles study of ZnO:organic superlattices fabricated by ALD/MLD. *Nano Energy* **22**, 338–348 (2016).
 101. Van Hook, W. A. Vapor pressures of the isotopic waters and ices. *The Journal of Physical Chemistry* **72**, 1234–1244 (1968).
 102. Apelblat, A. Vapour pressures of H₂¹⁶O and H₂¹⁸O, and saturated aqueous solutions of KCl from T=298K to T=318K by the isoteniscopic method. *The Journal of Chemical Thermodynamics* **30**, 1191–1198 (1998).

- 
103. Wu, X. *et al.* Thermal Conductivity of Wurtzite Zinc-Oxide from First-Principles Lattice Dynamics – a Comparative Study with Gallium Nitride. *Scientific Reports* **6**, 22504 (2016).
104. Wang, Z., Wang, F., Wang, L., Jia, Y. & Sun, Q. First-principles study of negative thermal expansion in zinc oxide. *Journal of Applied Physics* **114**, 063508 (2013).
105. Nie, T., Zhang, K., Xu, J., Lu, L. & Bai, L. A facile one-pot strategy for the electrochemical synthesis of poly(3,4-ethylenedioxythiophene)/Zirconia nanocomposite as an effective sensing platform for vitamins B2, B6 and C. *Journal of Electroanalytical Chemistry* **717–718**, 1–9 (2014).
106. Losego, M. D., Blitz, I. P., Vaia, R. A., Cahill, D. G. & Braun, P. V. Ultralow Thermal Conductivity in Organoclay Nanolaminates Synthesized via Simple Self-Assembly. *Nano Lett.* **13**, 2215–2219 (2013).
107. Giri, A. *et al.* Heat-transport mechanisms in molecular building blocks of inorganic/organic hybrid superlattices. *Phys. Rev. B* **93**, 115310 (2016).
108. Bergsman, D. S., Closser, R. G. & Bent, S. F. Mechanistic Studies of Chain Termination and Monomer Absorption in Molecular Layer Deposition. *Chem. Mater.* **30**, 5087–5097 (2018).
109. Davis, S. J. & Elvidge, J. A. 789. Heterocyclic syntheses with malonyl chloride. Part I. Pyrano-1 : 3-dioxins from ketones. *J. Chem. Soc.* 4109–4114 (1952) doi:10.1039/JR9520004109.

Appendix



Nanoporous materials

To set up the deposition process of alucone, the QCM analysis was utilized to monitor the growth of alucone as demonstrated previously. Figure A.1 presents the QCM result of alucone with varied exposure time of EG. First, the positive and consistent MGPC indicated the formation of alucone under set condition and linear growth, i.e. without termination, in this process. As for the discrepancy between the MGPC with varied exposure time of EG, it suggested that the low reactivity between the methyl groups, which were exposed at the surface after the pulse of TMA, and hydroxyl groups on the EG molecules. Hence, the exposure of EG was utilized to prolong the reaction time and increase collisions between EG molecules and surface reactive species.

However, the extremely long exposure time, i.e. 15 s in our result, was unfavorable to deposit pure alucone since the hydrogen bonds between EG molecules made it hard to eliminate redundant EG from the surface. Thus, the moderate exposure time, i.e. 5 s, was considered as a proper setting. In fact, the deposition temperature was also elevated from 105 °C to 135 °C, the MGPC with 15 s exposure time of EG decreased from 114.5 ng cm⁻² to 103.9 ng cm⁻². This result confirmed that the increment

of MGPC was partially attributed to physisorbed EG molecules, which were able to be removed at elevated temperature easily. Nonetheless, although the pure alucone could be obtained at elevated deposition temperature, the deposition temperature was still set at 105 °C to cater for most of plastic substrates.

After verifying the growth of alucone by QCM analysis, 300 cycles of alucone thin films without/with 5 s exposure of EG and were deposited on Si-wafer to further confirm the growth of alucone by ellipsometry and scanning electron microscope. As observed by QCM analyses, the growth of alucone without the exposure of EG was much slower than that with 5 s exposure of EG, so the thickness of deposited films were about 33 nm and 60 nm, respectively; namely, the growth rate per cycle could be increased from 0.11 nm/cycle to 0.2 nm/cycle by prolonging the exposure time of EG. The cross-sectional SEM images of alucone film with the exposure of EG are presented in Figure A.2.


Compared with reported values, the reported growth rates are 0.22~0.26 nm/cycle and 0.17~0.19 nm/cycle at 100 °C and 130 °C, respectively; therefore, the growth rate in our result was reasonable, i.e. ~0.2 nm/cycle at 105°C. Besides the growth rate, the refractive index of our alucone films, 1.45~1.51, also tallied with reported value, about 1.5. With these verification, we concluded that the deposition of alucone was established successfully in our MLD system.

For verifying the effect of low-temperature pyrolysis process we developed, TGA analysis was implemented to estimate carbon-residue in alucone films after annealing.

Figure A.3 is the TGA result of the core-material, SiO₂ nanoparticles. It interpreted that there was no obvious mass-change of SiO₂ nanoparticles in the test window, i.e. 0~400 °C, hence the mass-change of SiO₂/alucone core-shell particles could be only attributed to the deposited shell-material, alucone.

First, the TGA results of the SiO₂/alucone core-shell particles with the 100 sccm O₂ flow are presented in Figure A.4. In Figure A.4 (a), it revealed that the carbon-segments in alucone films could be removed completely at 450 °C within an hour. However, when the holding temperature decreased to 250 °C, the carbon-segments were not able to be eliminated entirely with the same annealing time, which can be observed in Figure A.4 (b). In Figure A.4 (c) and (d), as the holding temperature lowered to 120 °C, at which most of plastic substrates are stable, the carbon-residue inside the alucone after annealing was estimated 70~75% even the annealing time was prolonged to 2 hours. Comprehensively, the results established that the pyrolysis of carbon-segments in alucone was hard to implement at low annealing temperature under oxygen-contained atmosphere.

To address this issue, we developed the low-temperature pyrolysis process, in which the SiO₂/alucone core-shell particles were exposed to water vapor at varied



temperature but the same absolute humidity, i.e. 60°C, 99% RH and 90°C, 30% RH; besides, the SiO₂/alucone core-shell particles were also soaked into water at room temperature directly to clarify the hydrolysis of alucone. After holding in water vapor/water, the TGA analysis was also applied to the core-shell particles to evaluate the effect of carbon-elimination of our low-temperature pyrolysis process, and the results are shown in Figure A.5. The results indicated that the carbon-segments could be eliminated with the assistance of water vapor/water on a certain level, which was estimated as 70% and 60% for water vapor and water, respectively. Nonetheless, it is noteworthy that the holding times in water vapor and water were 1 day and 5 days, respectively; hence, the effect of water vapor was superior to that of water. As for the influence of temperature, we concluded that it was much effective to remove carbon-segments in alucone at elevated temperature with the same absolute humidity.

Although the carbon-segments couldn't be eliminated completely, it is still noticeable that the process temperature was only 90°C, which is tolerable to the common plastic substrates. However, based on our results, we deemed that the effect of low-temperature pyrolysis process could be further enhanced, i.e. reducing carbon-residue and holding time, by increasing the process temperature slightly and tuning the absolute humidity of circumstance.



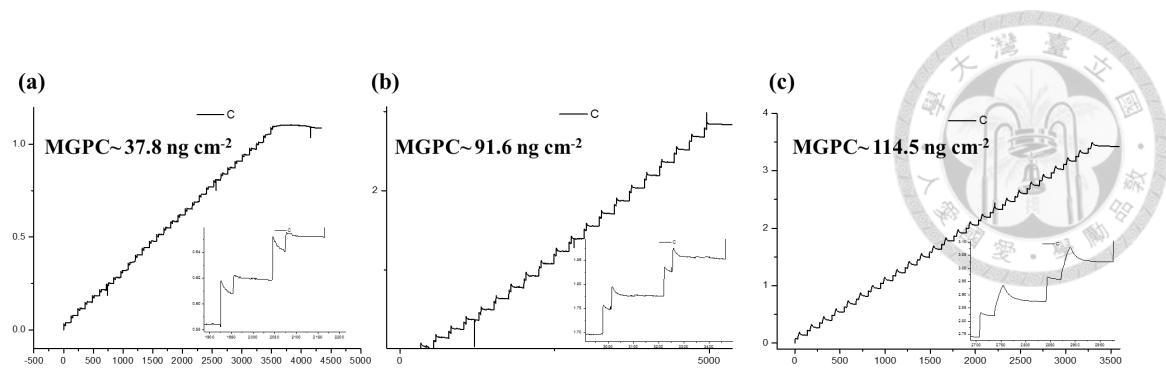


Figure A.1: The QCM result of alucone with varied exposure time (a) without; (b) 5 s; (c) 15 s of EG deposited at 105 °C. In the figure, the y-axis represents the mass gain, and the unit is ng/cm²; the x-axis is the time whose unit is second.

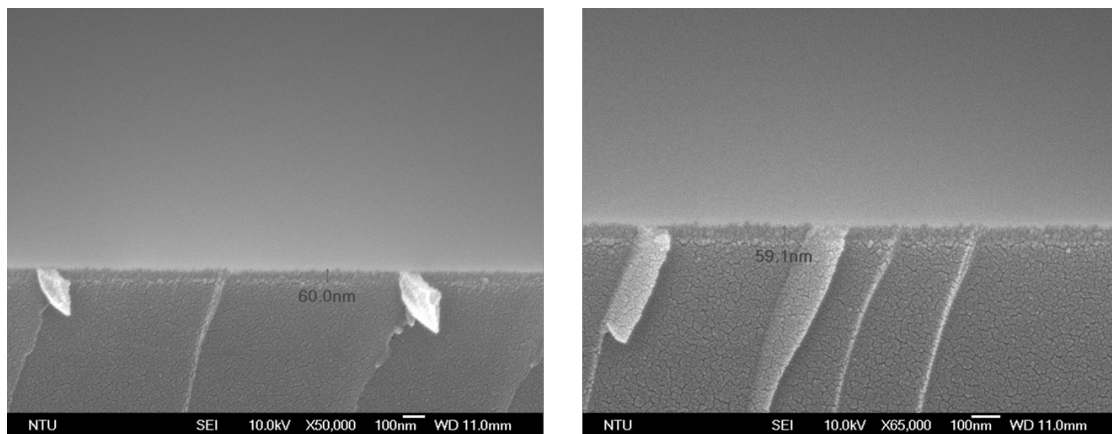


Figure A.2: The cross-sectional SEM images of alucone film with the exposure of EG.

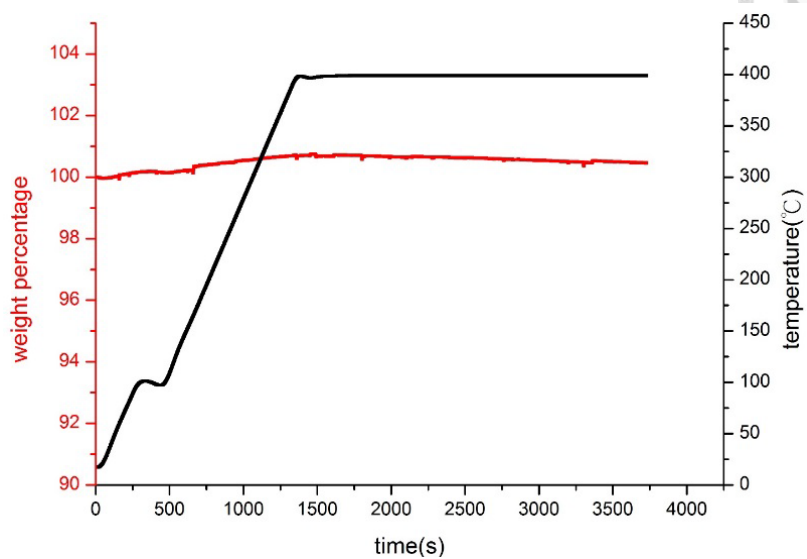


Figure A.3: The TGA result of the SiO₂ nanoparticles.

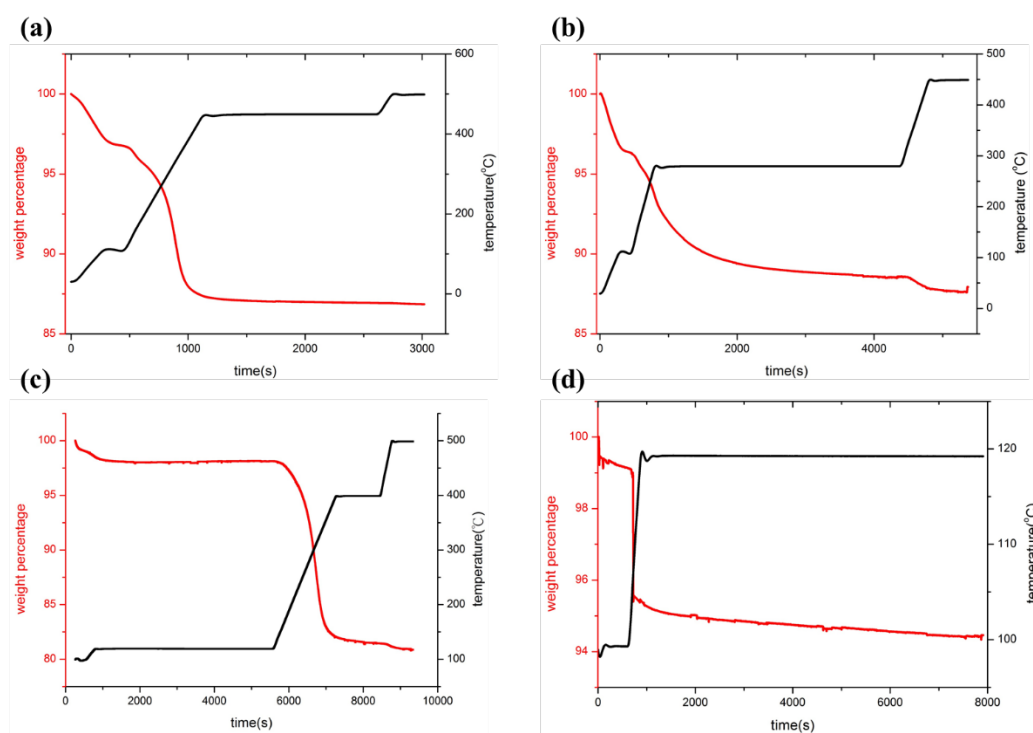


Figure A.4: The TGA results of the SiO₂/alucone core-shell particles.

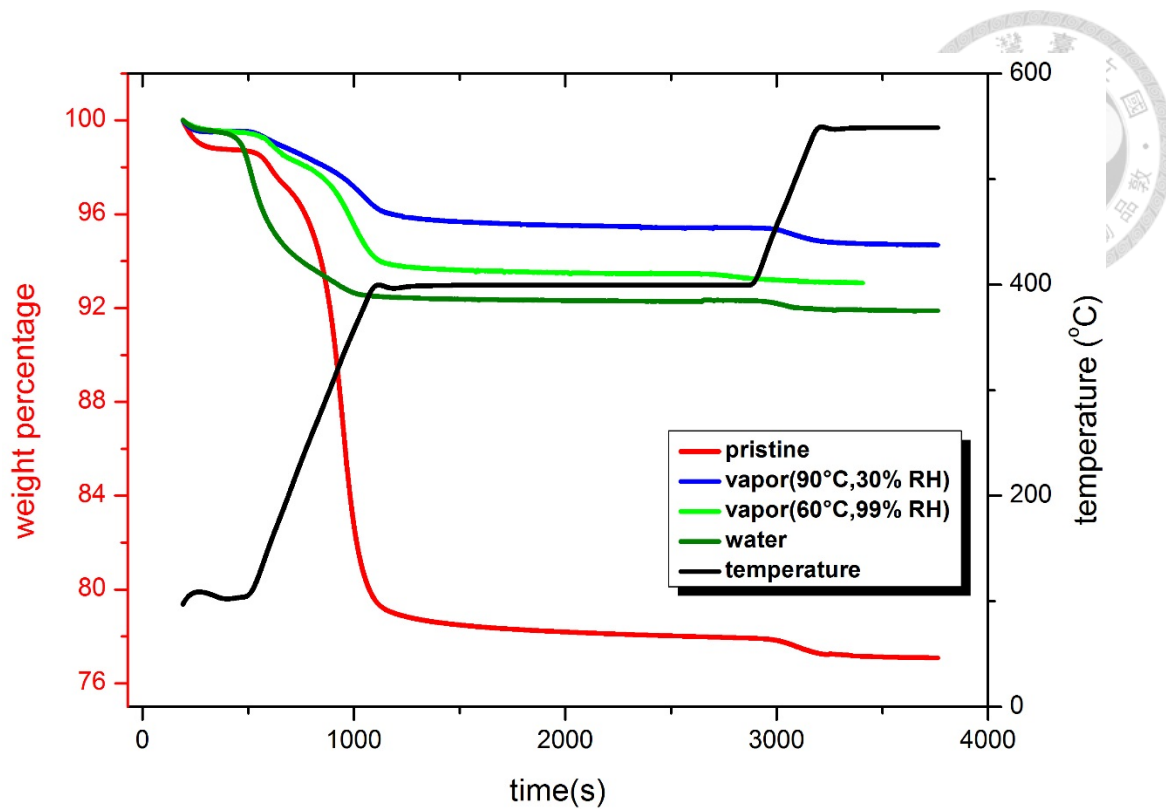


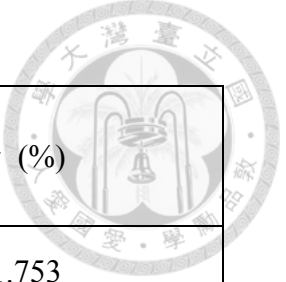
Figure A.5: The TGA results of the SiO₂/alucone core-shell particles after varied low-temperature pyrolysis process.

Other data

Table A.1: The electrical properties of HZO after annealing in H₂/N₂.

	Δn (%)	$\Delta \mu$ (%)	$\Delta \sigma$ (%)
200°C 15m	-0.6	-3.8	-4.5
300°C 5m	-2.9	0.3	-2.6
350°C 1m	-24.0	-4.8	-27.6
350°C 3m	-17.6	-13.6	-28.9
350°C 5m	-31.6	-33.0	-54.1
450°C 1m	-38.4	-71.1	-82.2
450°C 3m	-64.7	-53.2	-83.5

Table A.2: The electrical properties of HZO after annealing in N₂.



	Δn (%)	$\Delta \mu$ (%)	$\Delta \sigma$ (%)
350°C 5m	-17.181	-17.642	-31.753
350°C 3m	-0.382	-4.129	-4.646
300°C 10m	27.202	-31.868	-13.333
300°C 5m	3.742	-4.259	-0.572
300°C 3m	-0.249	0.964	0.634
300°C 1m	1.480	-3.315	-3.373
250°C 10m	0.797	-20.529	-7.702
200°C 10m	-7.735	-0.598	-8.180

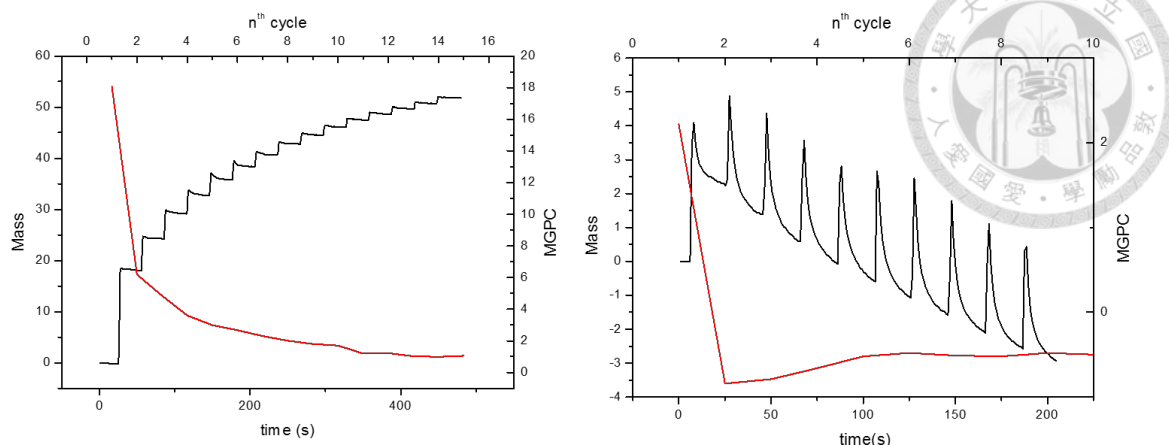


Figure A.6: (a) The multiple pulse of SbCl₅ on the DEZn surface; (b) The multiple pulse of DEZn on the SbCl₅ surface. The deposition settings: SbCl₅: 0.1/0/30; DEZn: 0.05/0/20. In Figure A.6 (a), it shows that SbCl₅ was able to adsorb on the DEZn surface and react with the surface reactive species. As for the decreasing MGPC, it may interpret that the decreasing reaction sites for SbCl₅ and/or the self-condensation of SbCl₅ at the latter cycles. In Figure A.6 (b), it reveals that only the first pulse of DEZn possessed a positive mass gain on the surface of SbCl₅. Comprehensively, it seems that there is not a self-limited mechanism in the reaction between SbCl₅ and DEZn.

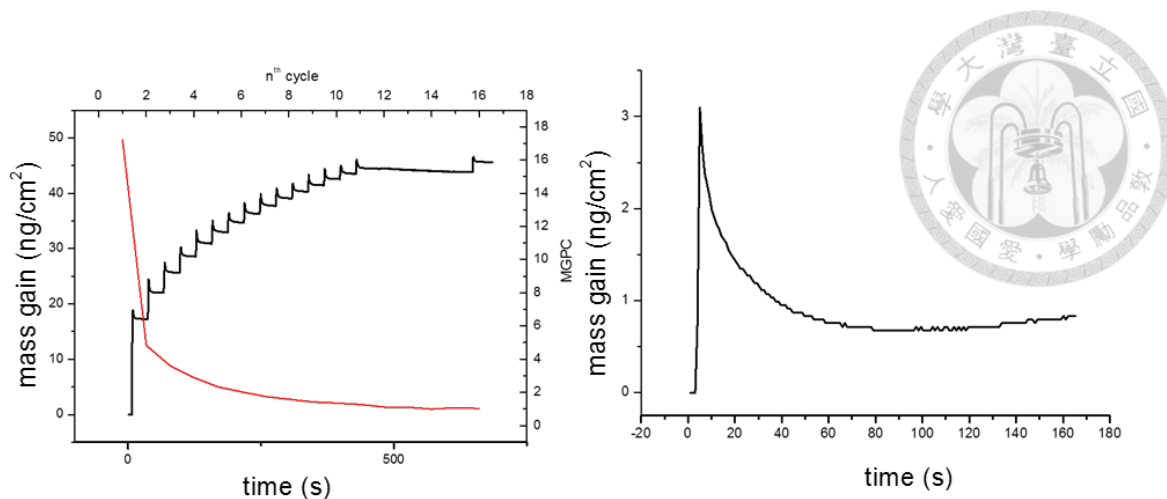


Figure A.7: The second run of the QCM result. (a) The multiple pulse of SbCl₅ on the DEZn surface; (b) The single pulse of DEZn on the SbCl₅ surface. The deposition settings: SbCl₅: 0.1/0/30; DEZn: 0.05/0/20. By comparing Figure A.6 (b) with Figure A.7 (b), it reveals that the multiple pulse of DEZn indeed eliminated substances from the surface of QCM crystal.

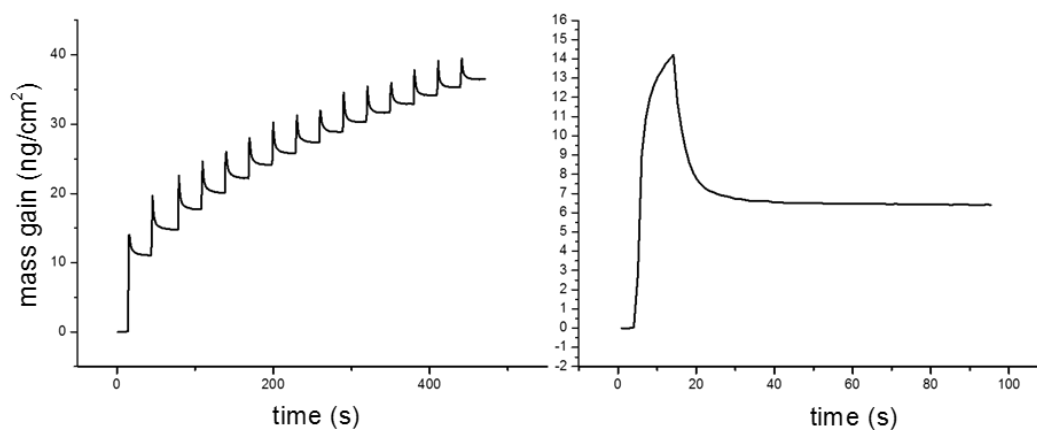


Figure A.8: The third run of the QCM result. (a) The multiple pulse of SbCl₅ on the DEZn surface; (b) The single pulse of DEZn on the SbCl₅ surface. The deposition settings: SbCl₅: 0.1/0/30; DEZn: 0.05/10/30. The exposure of DEZn cannot remove substances as the multiple pulse of DEZn did in previous run (shown in Figure A.7 (b)).

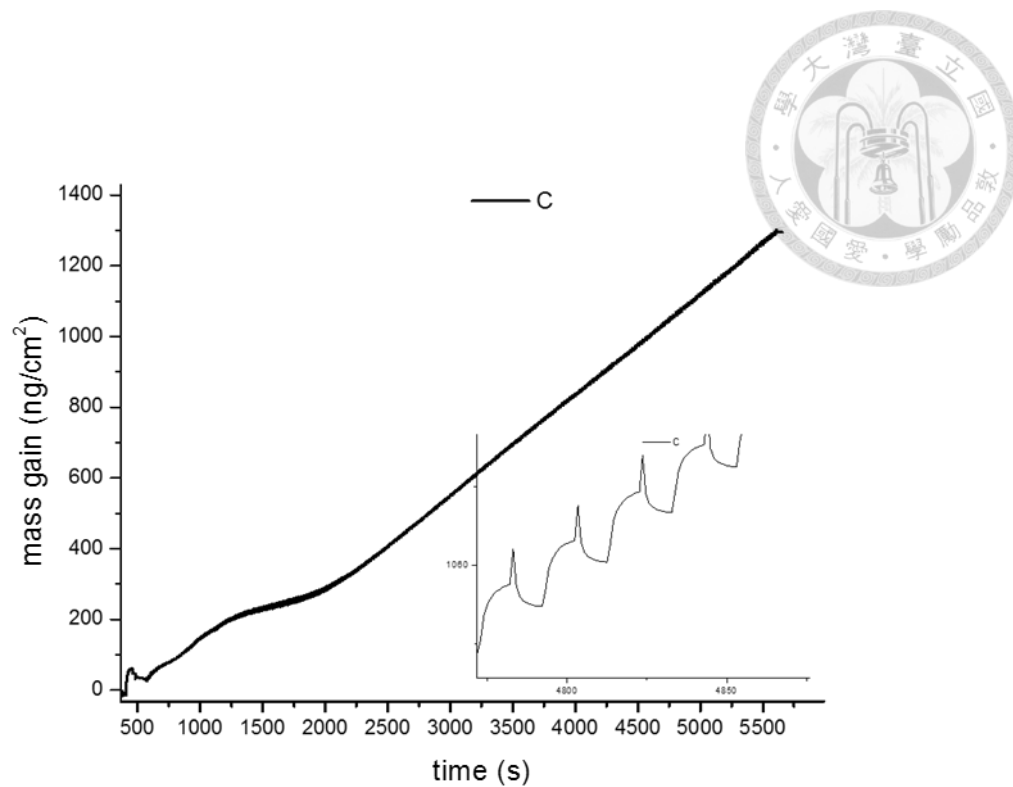


Figure A.9: The QCM result of the reaction by the usage of DEZn and SbCl_5 . The deposition settings: SbCl_5 : 0.1/0/30; DEZn: 0.05/0/20. In this figure, it shows that reaction could be continued all the time. However, the MGPC and the QCM pattern might change as the deposition cycles increased.